Neutrino induced charm production in the CHORUS calorimeter

Kees van der Poel

Neutrino induced charm production in the CHORUS calorimeter

Een wetenschappelijke proeve op het gebied
van de Natuurwetenschappen, Wiskunde en Informatica.

Proefschrift

ter verkrijging van de graad van doctor
aan de Katholieke Universiteit Nijmegen,
volgens besluit van het College van Decanen
in het openbaar te verdedigen
op woensdag 15 september 1999,
des namiddags om 3.30 uur precies,

door

Cornelis Andreas Franciscus Johannes van der Poel

geboren op 9 oktober 1968 te Maastricht.

Promotor: **Prof. Dr. P. Duinker**
Co-promotor: **Dr. R. van Dantzig (NIKHEF)**

Manuscriptcommissie: **Prof. Dr. S.J. de Jong**
                                      Dr. M.A.J. Botje (NIKHEF)
                                      Dr. J.E.J. Oberski (NIKHEF)

To Marie-Louise

Contents

Contents

Introduction

The aim of our work is to use the CHORUS experiment [1] at CERN to measure the strangeness content of the nucleon via neutrino induced deep inelastic charm production. The strange quark distribution function has become in recent years an increasingly significant component of the nucleon internal structure.

Charm production is an important testing ground for perturbative QCD due to the large contribution from gluon-initiated diagrams. In addition, understanding the threshold behaviour associated with the heavy charm mass is critical to the extraction of the weak mixing angle, $\sin^2\theta_W$, from neutrino neutral-current and charged-current data.

CHORUS has been designed to measure $\nu_\mu \rightarrow \nu_\tau$ oscillations but over the years a considerable amount of additional data of neutrino induced deep-inelastic charged current events originating in the CHORUS calorimeter with two opposite charged muons and a hadronic shower in the final state have been accumulated. Such events are indicative for the production of charmed hadrons. They are mostly characterised by a high four-momentum transfer from the beam particle to the target nucleon.

Nucleons, protons and neutrons, are spin $\frac{1}{2}$ particles that form atomic nuclei. During the late sixties in deep-inelastic experiments [2] it was observed with a 20 GeV electron beam at the Stanford Linear Accelerator (SLAC) that the electrons scattered of pointlike objects, partons, within the nucleon. Early attempts to understand these effects identified these partons with the quarks, as proposed by Gell-Mann and Zweig [3–5] to explain the hadron spectrum. In the naive quark model a nucleon contains three spin $\frac{1}{2}$ valence quarks together determining its static properties like total electric charge and magnetic moment. In this model the proton is formed by two constituent u (up) quarks, with electric charge $+\frac{2}{3}$, and one d (down) quark with charge $-\frac{1}{3}$ (units of the elementary charge e). The neutron is an isospin mirror image of the proton: it has two d quarks and one u quark. In the Quark Parton Model (QPM) [6] the

Introduction

valence quarks are embedded in a sea of virtual quark-antiquark pairs.

Several experiments from the late sixties onward have provided the so called nucleon structure functions which contain information on the momentum and spin distribution of the partons. In the QPM scattering with an external probe takes place as if the partons inside the nucleon are free pointlike particles [7, 8], demonstrated by a phenomenon called scaling. The scaling properties of the partons can be explained by the concept of asymptotic freedom. Data taken in the seventies at Fermilab and CERN from neutrino, electron and muon induced interactions exhibit scaling violations indicating that interactions between quarks can only be ignored at very short distance, i.e. in the scaling limit. Moreover it was found that quarks only account for about 50% of the nucleon momentum. The other half thus must be carried by gluons, without electric charge, exchanged between the quarks and keeping them inside the nucleon. Besides the flavours u and d, the sea also contains s (strange) quarks with a charge $-\frac{1}{3}$.

Discoveries in the seventies in particular of the $J/\psi(1S)$ [9, 10], and the $\Upsilon(1S)$ meson [11, 12] on one hand, and the τ lepton [13], on the other hand together with the deep-inelastic scattering results, paved the way for the Standard Model (SM) of the electroweak [14–16] and strong interaction. Two types of particles appear in the SM, the elementary fermions of matter, particles with half-integral spin, and the mediators of the elementary forces, the intermediate vector bosons, particles with integral spin. The fermions are grouped in three families, of two quarks and two leptons each. These families are up and down (u, d), charm and strange (c, s) and top and bottom (t, b) for quarks and electron and electron neutrino (e, ν_e), muon and muon neutrino (μ, ν_μ) and tau and tau neutrino (τ, ν_τ) for leptons. The electromagnetic force is mediated by zero mass photons, the weak force by very massive intermediate vector bosons, and the strong force by eight zero mass gluons. The electromagnetic force couples to particles with electric charge, the weak force acts on all particles but is suppressed at low momentum transfer due to the large mass of the exchanged bosons. The strong force couples to particles with colour charge, quarks and gluons.

The part of the Standard Model which describes the dynamics of particles with colour is called Quantum Chromodynamics (QCD). The quarks exchange gluons, the gauge bosons of the strong force. Colours come in three varieties, red, blue, and green with their corresponding anti-partners. Quarks carry colour and gluons colour as well as anti-colour. Since gluons carry (anti-)colour themselves, they can interact with other gluons. The strong coupling strength

should be represented by a running coupling "constant" (α_s), the strong force growing as the interparticle distance increases. The scale for the strong coupling strength is given by Λ_{QCD} ($\sim$ 0.2 GeV). Quarks and gluons have not been observed at asymptotically large interparticle distances, which can be explained by another basic concept called colour confinement. Detectable particles are colour neutral (white). Knowledge of the quark distribution functions of the nucleon is needed in QCD to predict scattering processes on nucleons. These quark distributions are given as a function of two kinematical variables, Q^2 and x. In the kinematic region where perturbation theory can be used, QCD describes the evolution of these distributions in Q^2 according to the Dokshitzer Gribov-Lipatov Altarelli-Parisi (DGLAP) equations [17–21], provided that they are given as a function of the Bjorken scaling variable x [22].

Neutrinos only participate in weak interactions. These weak interactions are generated by the exchange of a charged vector boson $\mathrm{W}^\pm$, or a neutral vector boson Z^0, denoted as charged current (CC) and the neutral current (NC), respectively.

In the Standard Model with SU(2) × U(1) as the gauge group of electroweak interactions, both the quarks and the leptons are assigned to be left-handed doublets and right-handed singlets. The quark mass eigenstates are not the same as their weak eigenstates, and the matrix relating these bases is defined for three families and given an explicit parametrisation by Kobayashi and Maskawa [23]. It generalises the four quarks (two quark families) case, where the matrix is parametrised by a single angle, the Cabibbo angle [24] to the three families situation. The mixing is expressed in terms of a 3 × 3 unitary matrix V, called the Cabibbo-Kobayashi-Maskawa (CKM) matrix. For our work only two matrix elements are important, V_{cd} and V_{cs}. The first one describes the probability amplitude of the charged current quark flavour transition $d \leftrightarrow c$, the second one $s \leftrightarrow c$. Transitions between quark flavours of different families are an order of magnitude less probable than transitions within the same family. This phenomenon is called Cabibbo suppression. Muon-neutrino induced charm production on $d(\bar{d})$ quarks is Cabibbo suppressed. For ν_μ interactions about 50% of charm production takes place on strange sea quarks while for $\bar{\nu}_\mu$ interactions it rises to about 90%. These numbers can be understood if one considers that for charm production neutrinos scatter on d and s quarks, while anti-neutrinos on $\bar{d}$ and $\bar{s}$, and the nucleon content of s and $\bar{s}$ is the same, while the content of d is about a factor of nine larger than that of $\bar{d}$.

The remaining part of the thesis is structured as follows. After having sketched the basic theoretical context of our research in Chapter 1 an overview

Introduction

of the experimental setup is given in Chapter 2. In Chapter 3 the data selection and analysis method is described, and in Chapter 4 the results are given. We end with a summary and an outlook for future research.

Chapter 1

Charm production in neutrino charged current interactions

This chapter describes the theoretical framework of dimuon production induced by muon-neutrino deep-inelastic nucleon scattering. First we treat neutrino deep inelastic scattering in general. Then we turn to charm production, fragmentation of charm quarks and the subsequent muon decay of the produced charmed hadrons. Also non-charm "background" processes are briefly discussed. The current status of neutrino induced CC charm production is summarised. The physics Monte Carlo models used for our analysis are described in the last section. Throughout this chapter the natural system of units is used were $\hbar = c = 1$ with energy measured in units of GeV, momentum in GeV/c and mass in GeV/c^2.

1.1   Neutrino deep inelastic scattering

Kinematics
The Feynman diagram of inclusive deep inelastic charge current muon-neutrino–nucleon reaction

$$\nu_\mu + \mathrm{N} \rightarrow \mu^- + \mathrm{X}, \tag{1.1}$$

1. Charm production in neutrino charged current interactions
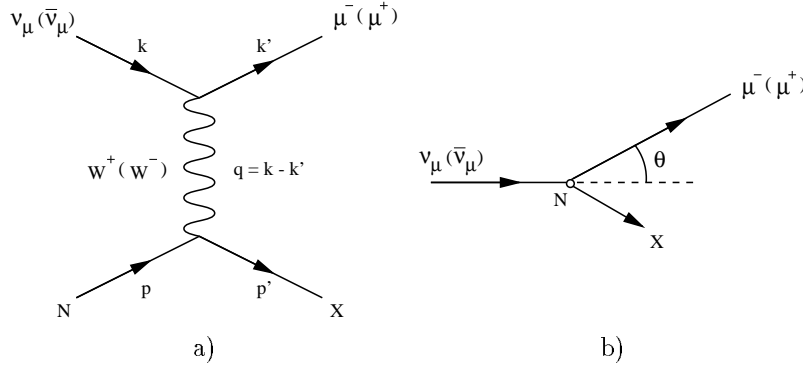
Figure 1.1: The inclusive deep inelastic CC muon-neutrino–nucleon interaction a) Feynman diagram, and b) the reaction in the laboratory frame.

is given in Figure 1.1a), where N is the nucleon and X represents any hadronic final state (hadronic fragments of nucleon break-up). The definitions used for the kinematical variables—see also Figure 1.1b)—are:

k, k'	four-momentum of neutrino and muon
p, p'	four-momentum of incoming nucleon and outgoing hadronic final state
$q = k - k'$	four-momentum transfer
M	rest mass of the nucleon
E_ν	neutrino energy in the laboratory frame
E_μ	muon energy in the laboratory frame
θ	angle between the muon and neutrino momentum vectors in the laboratory frame

   In the laboratory frame we consider, for simplicity, the nucleon to be at rest, Fermi motion related to nuclear binding energy is neglected. The Lorentz invariant kinematical variables: the square of the four-momentum transfer, $-Q^2$, the energy transfer in the laboratory frame, ν, the invariant mass squared of the hadronic final state, W^2, and the square of the centre-of-momentum

energy, s, are defined by

$$Q^2 = -q^2 = -(k - k')^2, \tag{1.2}$$

$$\nu = \frac{p \cdot q}{\sqrt{p \cdot p}}, \tag{1.3}$$

$$W^2 = p'^2 = M^2 + 2M\nu - Q^2, \tag{1.4}$$

$$s = (k + p)^2. \tag{1.5}$$

The deep inelastic case means that $Q^2 \gg M^2$. Two dimensionless Lorentz invariant variables, x (Bjorken) and y (inelasticity) are defined by

$$x = \frac{Q^2}{2p \cdot q} = \frac{Q^2}{2M\nu}, \tag{1.6}$$

$$y = \frac{p \cdot q}{p \cdot k}. \tag{1.7}$$

The Bjorken variable x can be interpreted as the fraction of the nucleon momentum carried by a parton in the frame, where the nucleon has infinite momentum, and where—consequently—the parton mass and transverse momentum are negligible.

To describe the kinematics of the inclusive process of reaction 1.1, a triplet of independent variables is sufficient, for example (E_ν, x, y), (E_ν, Q^2, ν) or (s, Q^2, W^2). In the deep inelastic case the mass of the muon can be neglected, $m_\mu/E_\mu \to 0$ and $m_\mu^2/Q^2 \to 0$, and the kinematical invariants expressed in laboratory frame variables become

$$Q^2 \overset{\text{(lab)}}{=} 4E_\nu E_\mu \sin^2(\theta/2), \tag{1.8}$$

$$\nu \overset{\text{(lab)}}{=} E_\nu - E_\mu, \tag{1.9}$$

$$s \overset{\text{(lab)}}{=} M^2 + 2ME_\nu, \tag{1.10}$$

$$y \overset{(lab)}{=} \frac{E_\nu - E_\mu}{E_\nu}. \tag{1.11}$$

Differential cross-section

To describe the deep inelastic charged current process the formulation of Aivazis et al. [25, 26], especially developed to avoid the artificial distinction between "light" and "heavy" quarks, is followed. The differential cross-section, neglect-

7

1. Charm production in neutrino charged current interactions

ing the muon mass, can be expressed as

$$\mathrm{d}\sigma = \frac{G_W^2}{2\Delta(s, m_{\nu_\mu}^2, M^2)} 4\pi Q^2 L^\mu{}_\nu W^\nu{}_\mu \mathrm{d}\Gamma, \qquad (1.12)$$

where $G_W = (G_F/\sqrt{2})/(1 + Q^2/m_W^2)$ with m_W denoting the mass of the W-boson and G_F the Fermi coupling constant. In the kinematic domain of deep inelastic neutrino reactions described in this thesis one can neglect the term Q^2/m_W^2 in the definition of G_W^2 which results in replacing $2G_W^2$ by G_F^2. The mass of the muon neutrino, m_{ν_μ}, is taken to be zero. $L^\mu{}_\nu$ and $W^\nu{}_\mu$ are dimensionless Lorentz tensors describing in terms of the most general Lorentz covariant form the lepton and hadron currents respectively, and $\mathrm{d}\Gamma$ represents the phase space acceptance for the outgoing muon. The factor $4\pi Q^2$ comes from the normalisation of L and W and the factor $2\Delta(s, m_{\nu_\mu}^2, M^2)$ represents the incident flux, with the triangle function

$$\Delta(a, b, c) = \sqrt{a^2 + b^2 + c^2 - 2(ab + bc + ca)}. \qquad (1.13)$$

The tensors with implicit summation over repeated indices can be written as

$$L^\mu{}_\nu = \frac{4}{Q^2}\left(2k^\mu k'_\nu + 2k'^\mu k_\nu - g^\mu{}_\nu Q^2 - 2i\varepsilon^\mu{}_\nu{}^{\rho\delta} k_\rho k'_\delta\right), \qquad (1.14)$$

$$W^\nu{}_\mu = -g^\nu{}_\mu W_1 + \frac{p^\nu p_\mu}{M^2} W_2 - i\frac{\varepsilon^{\alpha\beta\nu}{}_\mu p_\alpha q_\beta}{2M^2} W_3 + \frac{q^\nu q_\mu}{M^2} W_4$$
$$+ \frac{p^\nu q_\mu + q^\nu p_\mu}{2M^2} W_5 + \frac{p^\nu q_\mu - q^\nu p_\mu}{2M^2} W_6, \qquad (1.15)$$

where $g_{\mu\nu}$ is the metric tensor, $\varepsilon^{\mu\nu\rho\delta}$ the totally antisymmetric Levi-Civita tensor, and the W_i the Lorentz covariant hadron structure functions, which are functions of two Lorentz invariant kinematical variables, usually ν and Q^2. Still neglecting terms proportional to the muon mass one can write the differential inclusive CC cross-section in the laboratory frame variables as

$$\frac{\mathrm{d}^2\sigma}{\mathrm{d}E_\mu \mathrm{d}\cos\theta} = \frac{2E_\mu^2 G_W^2}{\pi M}\left(2W_1 \sin^2(\theta/2) + W_2 \cos^2(\theta/2)\right.$$
$$\left.\pm \frac{E_\nu + E_\mu}{M} W_3 \sin^2(\theta/2)\right), \qquad (1.16)$$

8

where the $+(-)$ sign in front of the parity violating function W_3 refers to the case of neutrino(anti-neutrino) scattering. The hadron structure functions W_4, W_5, W_6 do not appear in Equation 1.16 because they are multiplied by lepton vertex factors of order of the lepton masses.

It is customary to rewrite the nucleon hadron structure functions in terms of the scaling structure functions F_i

$$F_1(x, Q^2) = W_1(\nu, Q^2),\tag{1.17}$$

$$F_2(x, Q^2) = \frac{\nu}{M} W_2(\nu, Q^2),\tag{1.18}$$

$$F_3(x, Q^2) = \frac{\nu}{M} W_3(\nu, Q^2),\tag{1.19}$$

where the $F_i(x, Q^2)$ for any given x in the limit $Q^2 \to \infty$, the Bjorken scaling limit, depend only on x. This scaling property of the structure functions was predicted by Bjorken [22] and observed in the SLAC data [7,8]. On a closer and more accurate look the $F_i(x, Q^2)$ depend logarithmically on Q^2. The differential cross section in terms of the scaling structure functions F_i can be written as

$$\frac{d^2\sigma}{dxdy} = \frac{2ME_\nu G_W^2}{\pi} \left[y^2 x F_1 + \left(1 - y - \frac{Mxy}{2E_\nu} \right) F_2 \right. \\ \left. \pm y(1 - y/2) x F_3 \right],\tag{1.20}$$

where the $+(-)$ sign for F_3 refers to the case of neutrino(anti-neutrino) scattering. To leading-order in the electroweak coupling, Equations 1.16 and 1.20 are completely general, assuming only Lorentz invariance and neglecting lepton masses.

QCD allows to relate the measurable scaling structure functions F_i to the quark-gluon degrees of freedom of the nucleon, in terms of parametrised quark x-distribution functions as a function of Q^2. The shape of the quark x-distribution functions depends on the quark flavour considered. The total valence quark x-distribution for an isoscalar target has the shape as shown in Figure 1.2 for two different values of Q^2. For higher Q^2 the centre of gravity of the distribution shifts to lower values of x. The sea quarks dominate at smaller values of x as shown in Figure 1.3. In these plots two standard parametrisations of the quark distribution function are shown, those from CTEQ 3L [27] and GRV 94 LO [28].

1. Charm production in neutrino charged current interactions
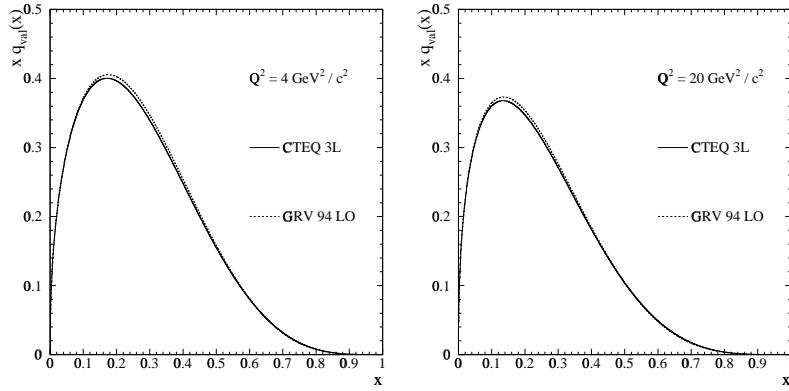
**Figure 1.2**: The total valence quark distribution $xq_{\mathrm{val}}(x, Q^2)$ for an isoscalar target at $Q^2 = 4$ GeV$^2/c^2$ (left) and $Q^2 = 20$ GeV$^2/c^2$ (right). The different curves represent parametrised fits from CTEQ 3L [27] and GRV 94 LO [28] as indicated.
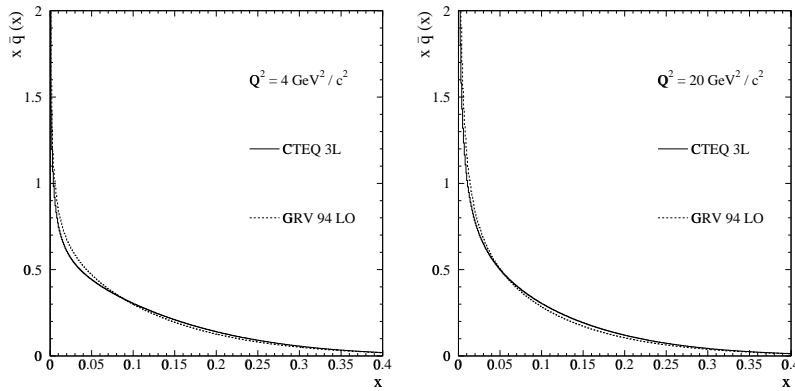

Figure 1.3: Similar to Figure 1.2 for the total anti-quark distribution function $x\bar{q}(x, Q^2)$.

1.2 Charm production

Going now from inclusive scattering to the semi-inclusive case of charm production, the symbol X in reaction 1.1 is from now on supposed to describe any hadronic state which includes a charmed hadron. Charm production in neutrino charged current reactions can conveniently be described in the helicity formalism, which incorporates both target mass and heavy quark mass effects. We note that the target nucleon mass is comparable to the charm quark mass, and non-negligible compared to the typical scale Q of the process in the kinematic domain of current interest. Following the formulation and notation of [25, 26], the differential CC cross section is expressed as

$$
\frac{\mathrm{d}^2\sigma}{\mathrm{d}x\mathrm{d}y} = G_W^2 \frac{yQ^2}{2\pi} \left[\frac{F_+ + F_-}{2}(1 + \cosh^2\psi) + F_0 \sinh^2\psi \right.
$$
$$
\left. \mp (F_+ - F_-)\cosh\psi \right],
$$
(1.21)

where the $-(+)$ sign in front of the $(F_+ - F_-)\cosh\psi$ term refers to the case of neutrino(anti-neutrino) scattering and where ψ, the hyperbolic rotation angle, is defined by

$$
\cosh\psi = \frac{2(p \cdot \{k + k'\})}{\Delta(-Q^2, p^2, p'^2)},
$$
(1.22)

representing a Lorentz boost between the standard lepton configuration, where the lepton momenta are collinear, and the standard hadron configuration, where the hadron momenta are collinear. The helicity structure functions F_-, F_0, F_+ for left-handed $(-)$, longitudinal (0), and right-handed $(+)$ vector bosons are defined as

$$
F_- = F_1 + \frac{1}{2}\sqrt{1 + \frac{Q^2}{\nu^2}}F_3,
$$
(1.23)

$$
F_0 = -F_1 + \left(1 + \frac{Q^2}{\nu^2}\right)\left(\frac{1}{2x}\right)F_2,
$$
(1.24)

$$
F_+ = F_1 - \frac{1}{2}\sqrt{1 + \frac{Q^2}{\nu^2}}F_3.
$$
(1.25)

The first term on the right hand side in Equation 1.21 involves the transverse scaling structure function $F_T = (F_+ + F_-)/2$, the second term the longitudinal scaling structure function $F_L = F_0$, whereas the third term is the parity-

1. Charm production in neutrino charged current interactions

violating term with $F_+ - F_-$ proportional to F_3. We note that in the zero target mass limit $M^2/Q^2 \to 0$, equivalent to $Q^2/\nu^2 = 4x^2 M^2/Q^2 \to 0$, the following approximations can be made: $F_\pm = F_1 \mp F_3/2$ and $F_0 = -F_1 + F_2/(2x)$. When longitudinal $W^\pm$ exchange can be neglected, $F_0 \to 0$, the last equation results in the Callan-Gross relation $F_2 = 2xF_1$ [29].

The helicity structure functions can be expressed in terms of CKM matrix elements, a kinematical factor, and the quark x-distribution functions of the nucleon. To leading-order (LO) QCD, the helicity structure functions for neutrino scattering producing a charm quark then are

$$F_\pm^{\nu\,LO} = |V_{ca}|^2 \frac{(Q^2 + m_a^2 + m_c^2) \mp \Delta(-Q^2, m_a^2, m_c^2)}{\Delta(-Q^2, m_a^2, m_c^2)} q_N^a(\chi), \tag{1.26}$$

$$F_0^{\nu\,LO} = |V_{ca}|^2 \frac{(m_c^2 - m_a^2)^2/Q^2 + (m_a^2 + m_c^2)}{\Delta(-Q^2, m_a^2, m_c^2)} q_N^a(\chi), \tag{1.27}$$

where a sum over contributing parton flavours a (s and d quarks) is implied. The quantity V_{ca} is the CKM matrix element, m_a the initial quark mass, m_c the charm quark mass. The a quark distribution $q_N^a(\chi)$ in the nucleon is a function of the modified scaling variable χ, accounting for target mass and quark mass effects, according to

$$\chi = \eta \frac{(Q^2 - m_a^2 + m_c^2) + \Delta(-Q^2, m_a^2, m_c^2)}{2Q^2}, \tag{1.28}$$

with η defined by

$$\frac{1}{\eta} = \frac{1}{2x} + \sqrt{\frac{1}{4x^2} + \frac{M^2}{Q^2}}. \tag{1.29}$$

This inverted form is chosen to show that η reduces to x in the zero target mass limit $M^2/Q^2 \to 0$.

For neutrino induced charm-production, the initial quarks (d and s) can be treated as massless, $m_a^2/Q^2 \to 0$, and one obtains for the LO cross section in our kinematic domain

$$\frac{\mathrm{d}^2\sigma^{\nu\,LO}}{\mathrm{d}x\mathrm{d}y} = 2G_F^2 \frac{yQ^2}{\pi} \left(|V_{cd}|^2 d_N(\chi) + |V_{cs}|^2 s_N(\chi)\right)$$

$$\times \left[\left(\frac{1 + \cosh\psi}{2}\right)^2 + \frac{m_c^2}{2Q^2}\frac{\sinh^2\psi}{2}\right], \tag{1.30}$$

12

with $\chi = \eta(1 + m_c^2/Q^2)$.

In Equation 1.30, the quark distribution functions evolve in Q^2 according to the Dokshitzer Gribov-Lipatov Altarelli-Parisi (DGLAP) equations [17–21]. Moreover, in the zero target mass limit, the expression for the cross-section in Equation 1.30 stays unchanged; only the definitions of χ and ψ simplify. In particular

$$\chi \xrightarrow[m_a^2/Q^2 \to 0]{} \eta \left(1 + \frac{m_c^2}{Q^2}\right) \xrightarrow[M^2/Q^2 \to 0]{} x \left(1 + \frac{m_c^2}{Q^2}\right) = \xi, \tag{1.31}$$

$$\cosh \psi \stackrel{(\text{lab})}{=} \frac{E_\nu + E_\mu}{\sqrt{Q^2 + \nu^2}} \xrightarrow[M^2/Q^2 \to 0]{} \frac{2 - y}{y}, \tag{1.32}$$

where ξ is called the "slow-rescaling" variable [30].

Figure 1.4 compares the variable χ with ξ. The initial strange quark mass correction to χ is only important at low values of Q^2. At $Q^2 = 1$ GeV/c^2 it is about a 1% correction. The target mass correction grows toward high x, whereas the dimuon data studied in this thesis are concentrated in the low x regions ($x < 0.5$). Therefore, taking the target and initial state quark masses into account for the slow-rescaling variable provides a rather small correction (less than 5% for $Q^2 \geq 5$ GeV/c^2) to the dominant m_c dependence of ξ.

Several corrections have to be taken into account when applying Equation 1.30.

1) Radiative effects.
Electromagnetic radiative effects smear the final state kinematics. If the outgoing muon emits a photon, the observed muon energy is correspondingly lowered and the derived hadron energy raised. A correction for such radiative effects is calculated for the inclusive charged current cross-section using the prescription of Bardin [31], and is assumed to be the same for the (semi-inclusive) dimuon cross-section in the selected kinematical domain. Due to the radiative corrections events from low y migrate to high y, or, for fixed values of Q^2 and E_ν, from high x to low x. There is almost no dependence on the neutrino energy and a small dependence on y, but the correction ranges from about +10% at low x to about -20% at high x for our energies.

2) Nuclear effects.
Most measurements on neutrino induced charm production are made using target nuclei with medium or large atomic number A. One must correct for the neutron (d-quarks) excess present in non-isoscalar targets. In addition, there are possibly more subtle nuclear effects, like the EMC effect [32], fluctuations

1. Charm production in neutrino charged current interactions

a) initial quark mass correction b) target mass correction
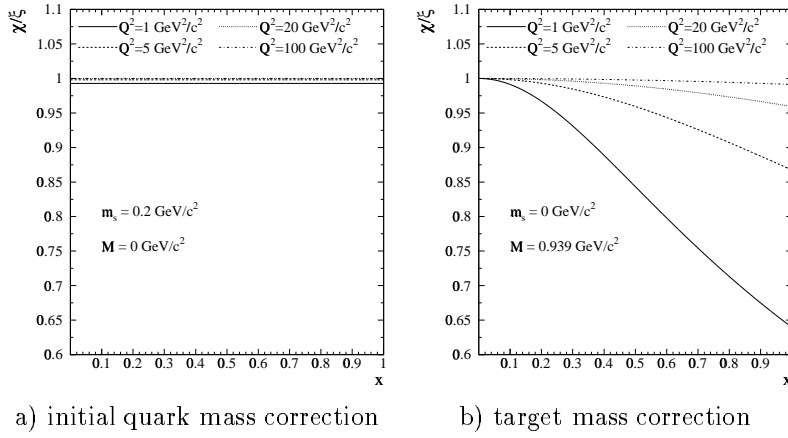
Figure 1.4: Relative effect of mass corrections for charm production to the ratio χ/ξ as a function of x for $m_c = 1.79$ GeV$/c^2$ in case of a) initial quark mass correction, and b) target mass correction at different Q^2-values.

of the virtual intermediate boson to mesons [33], gluon recombination [34, 35] and Fermi motion of nucleons inside the nucleus [36, 37]. Such effects have been observed and interpreted in terms of measured and calculated charged lepton structure function ratios for nucleus A and deuterium, F_i^A/F_i^D, where the Q^2 dependence is found to be insignificant. To correct for the neutron excess is straightforward, but to implement other nuclear effects would be ambiguous. However, one can estimate the level of systematic uncertainties due to nuclear effects in a calculated result by modifying in a phenomenological way the parton distributions used as input, in accordance with the nuclear structure function ratios.

For completeness, Equation 1.26, 1.27 and 1.30 also apply to the anti-neutrino case by replacing $\nu \to \bar{\nu}$, $F_\pm \to F_\mp$, $q_N^a \to \bar{q}_N^a$, $d_N \to \bar{d}_N$ and $s_N \to \bar{s}_N$. Since $F_0 \neq 0$ in neutrino and anti-neutrino scattering, the Callan-Gross relation $F_2 = 2xF_1$ [29] is not valid in LO QCD. But neglecting mass corrections the Callan-Gross relation holds in terms of the modified scaling variable χ, thus $F_2 = 2\chi F_1$.

14

Parton distributions

Before we can interpret our experimental data in terms of the above described formalism—in particular Equation 1.30—several additional assumptions and simplifications have to be made, in accordance with earlier experiments on charm production [38–42]. They are as follows:

1) Strong isospin symmetry, which implies:
a) the up quark distribution in protons is taken the same as the down quark distribution in neutrons and vice versa, thus
$$u^{\mathrm{p}}(x, Q^2) = d^{\mathrm{n}}(x, Q^2), \text{ and } d^{\mathrm{p}}(x, Q^2) = u^{\mathrm{n}}(x, Q^2),$$
where p and n refer to proton and neutron, and
b) the strange sea in protons and neutrons is the same, thus
$$s^{\mathrm{p}}(x, Q^2) = s^{\mathrm{n}}(x, Q^2).$$
From now on all parton distributions are expressed in terms of those of the proton, and the index p is omitted.

2) The non-strange (up and down) quark and antiquark components of the sea are assumed to be symmetric, so that $\bar{u}(x, Q^2) = u_{\mathrm{sea}}(x, Q^2)$, $\bar{d}(x, Q^2) = d_{\mathrm{sea}}(x, Q^2)$, in this terminology the u_{sea} contains only u and no $\bar{u}$ quarks. Furthermore an isospin symmetric sea is assumed resulting in $\bar{u}(x, Q^2) = \bar{d}(x, Q^2)$.

The total valence (in fact the d) quark distribution function for an arbitrary nucleus with A and Z as atomic and charge number can then be written as

$$x q_{\mathrm{val}}(x, Q^2) = \frac{A - Z}{A} x u_{\mathrm{val}}(x, Q^2) + \frac{Z}{A} x d_{\mathrm{val}}(x, Q^2). \tag{1.33}$$

The anti-quark distribution functions are combined to the total anti-quark distribution function as follows

$$x \bar{q}(x, Q^2) = x \bar{u}(x, Q^2) + x \bar{d}(x, Q^2) + x \bar{s}(x, Q^2). \tag{1.34}$$

The distribution functions for the total valence quark, Equation 1.33, and the total anti-quark distributions, Equation 1.34, cannot be derived in our case from a determination of F_2 and xF_3. We follow CHARM II [39, 40], and use two standard parametrisations from all known deep-inelastic scattering data CTEQ 3L [27] and GRV 94 LO [28]. They are shown in Figures 1.2 and 1.3 for an isoscalar target and taken from the CERN PDFLIB library [43].

Strangeness parametrisation

Using the assumptions mentioned above, but still allowing sufficient freedom for an independent measurement of the strange sea quark (in short: strangeness)

15

1. Charm production in neutrino charged current interactions

distribution function, the following method is used. The total valence quark and the total anti-quark distribution functions (from CTEQ 3L and GRV 94 LO) are kept fixed, while the parametrisations of the $\bar{u}$, $\bar{d}$, and $\bar{s}$ distribution functions are redefined using two additional parameters κ and α. The strangeness content of the nucleon is usually expressed through

$$\kappa = \frac{\int_0^1 \left[xs(x, Q_0^2) + x\bar{s}(x, Q_0^2) \right] \mathrm{d}x}{\int_0^1 \left[x\bar{u}(x, Q_0^2) + x\bar{d}(x, Q_0^2) \right] \mathrm{d}x}, \tag{1.35}$$

where $\kappa = 1$ would indicate a flavour SU(3) symmetric sea, and where Q_0 is a reference scale (in our case taken at 20 GeV$^2/c^2$). The dependence of κ on this reference scale is small as discussed in Section 1.6. The shape of the strangeness distribution is defined relative to that of the non-strange sea by the parameter α. The strangeness distribution is parameterised as

$$xs(x, Q^2) = x\bar{s}(x, Q^2) = A_s \left(1 - x \right)^\alpha \frac{x\bar{u}(x, Q^2) + x\bar{d}(x, Q^2)}{2}, \tag{1.36}$$

where $\alpha = 0$ implies that the strange sea and the non-strange sea have the same x dependence. At the same time the non-strange sea is parameterised as

$$\frac{x\bar{u}(x, Q^2) + x\bar{d}(x, Q^2)}{2} = \frac{x\bar{q}(x, Q^2)}{2 + A_s \left(1 - x \right)^\alpha}. \tag{1.37}$$

For given values of κ and α, the normalisation constant A_s can be solved numerically using the following equation

$$A_s = \kappa \left[\int_0^1 \frac{x\bar{q}(x, Q^2)}{2 + A_s \left(1 - x \right)^\alpha} \mathrm{d}x \right] \Big/ \left[\int_0^1 \frac{(1 - x)^\alpha x\bar{q}(x, Q^2)}{2 + A_s \left(1 - x \right)^\alpha} \mathrm{d}x \right]. \tag{1.38}$$

We note that A_s becomes identical to κ if $\alpha = 0$.

1.3   Fragmentation of charm quarks

The ν_μ CC interaction can produce a single charm quark in the final state. However, the bare charm quark—which has colour—is not observed; it forms a hadronic colour-neutral bound state. All of the nonperturbative processes that act to "dress" the charm quark so that it emerges as a hadron are known as

16

fragmentation or hadronisation processes. Although these processes cannot be described rigorously, their basic features can be described well by QCD inspired models.

Consider an initial quark Q with momentum p_Q. The probability that a hadron H with a momentum zp_Q in the interval $(z, z + \mathrm{d}z)$ is formed by the fragmentation of that quark is defined by $D_{H/Q}(z)\mathrm{d}z$, where $D_{H/Q}$ is the fragmentation function. When the energy of the initial quark is high with respect to the masses and transverse momenta which participate in the reaction, the fragmentation only depends on z, the fragmentation variable, where

$$z = p_H/p_H^{max}, \tag{1.39}$$

the hadrons maximum momentum is defined as $p_H^{max} = \sqrt{W^2/4 - m_H^2}$. The fragmentation variable can also be defined differently. Commonly used are the longitudinal momentum fraction relative to the W-boson direction: $z = p_{HL}/p_{QL}$; the momentum fraction of the hadron with respect to that of the initial quark: $z = p_H/p_Q$; in terms of the energy, $z = E_H/E_Q$, or a combination of both, $z = (E_H + p_H)/(E_Q + p_Q)$. These definitions are all equivalent at high energies, where $m_H^2/E_H^2 \to 0$ and $m_Q^2/E_Q^2 \to 0$.

In LO QCD the neutrino cross section for the production of a charmed hadron H factorises in the following way

$$\frac{\mathrm{d}^3\sigma^{\nu\,LO}}{\mathrm{d}x\mathrm{d}y\mathrm{d}z}(\nu\mathrm{N} \to \mu H\mathrm{X}) = \frac{\mathrm{d}^2\sigma^{\nu\,LO}}{\mathrm{d}x\mathrm{d}y}(\nu\mathrm{N} \to \mu c\mathrm{X})D_{H/c}(z). \tag{1.40}$$

This cross-section does not factorise in next-to-leading-order (NLO) QCD; then it contains a convolution as described in [44].

The analytical form of $D_{H/Q}(z)$ depends on the mass m_Q of the quark. For the light quarks (u, d and s), the Lund symmetric fragmentation function [45] is used

$$D_{H/Q}(z) = fz^{-1}(1 - z)^a \exp(-bm_t^2/z), \tag{1.41}$$

where f is a normalisation factor, $m_t = \sqrt{m_H^2 + p_t^2}$ is the hadrons transverse mass and p_t its transverse momentum, and where a and b are parameters of order 0.3 and 0.58 GeV^{-2}, respectively.

For heavy quarks, Peterson *et al.* [46] use the fact that fragmentation of a fast moving heavy quark Q into a hadron $H = (Q\bar{q})$ with a light quark q is

1. Charm production in neutrino charged current interactions

dominated by the inverse square of the energy difference. Taking longitudinal phase space into account, one gets the fragmentation function

$$D_{H/Q}(z, \epsilon_P) = f_H^P z^{-1} \left(1 - \frac{1}{z} - \frac{\epsilon_P}{1-z} \right)^{-2},$$ (1.42)

where f_H^P is the Peterson normalisation factor for hadron H, and ϵ_P a free parameter of order m_q^2/m_Q^2. This function peaks closer to $z = 1$ as ϵ_P decreases—and m_Q increases—as can be seen in Figure 1.5.
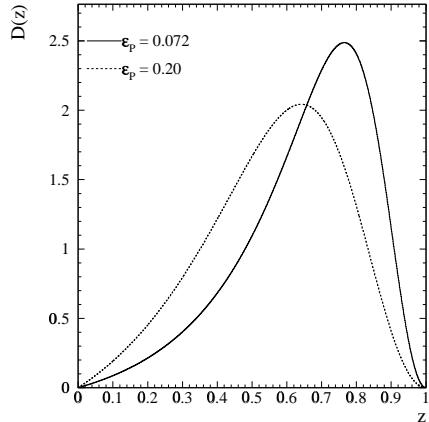
Figure 1.5: The Peterson *et al.* fragmentation function [46] for charm quarks as a function of z, shown for two different values of ϵ_P, $\epsilon_P = 0.072$ and $\epsilon_P = 0.20$, central values obtained by CHARM II [39, 40] and CCFR [41], respectively.

Collins and Spiller point out [47] that the Peterson *et al.* fragmentation function does not have the correct relation between the heavy quark fragmentation function and the heavy meson structure function. They proposed another parametrisation for the heavy quark fragmentation to solve this problem

$$D_{H/Q}(z, \epsilon_{CS}) = f_H^{CS} \left(\frac{1-z}{z} + \frac{2-z}{1-z}\epsilon_{CS} \right) (1+z^2) \left(1 - \frac{1}{z} - \frac{\epsilon_{CS}}{1-z} \right)^{-2},$$ (1.43)

where f_H^{CS} is the Collins-Spiller normalisation factor, and ϵ_{CS} a free parameter of order $\langle p_t^2 \rangle / m_Q^2$, with $\langle p_t^2 \rangle = (0.45 \text{ GeV}/c)^2$, p_t being the hadron's transverse momentum.

The normalisation factors f_H^P and f_H^{CS} are fixed by summing over all possible hadrons H containing Q,

$$\sum_H \int_0^1 D_{H/Q}(z)\mathrm{d}z = 1.$$ (1.44)

18

The transverse momentum of the charmed hadron with respect to the W-direction is on average small, $\langle p_t^2 \rangle = (0.45 \text{ GeV}/c)^2$. Generally the following distribution is used with a parameter β which is specific for the formed hadron

$$\frac{\mathrm{d}n}{\mathrm{d}p_t^2} \propto e^{-\beta p_t^2}. \qquad (1.45)$$

In our case the parameter $\beta = 1.70 \text{ (GeV}/c)^{-2}$ is taken to be the same for all formed charmed hadrons, because their masses are similar.

The argument of Collins and Spiller is not followed in previous LO QCD analyses, and for reasons of comparison we therefore stick to the Petersons form as well.

The gross features of charm fragmentation have been studied in $\mathrm{e^+e^-}$ collider experiments [48, 49] directly measuring the z fragmentation spectrum. In these experiments the fragmentation parameter is defined by $z = p_H/p_H^{max}$ where $p_H^{max} = \sqrt{E_{beam}^2 - m_H^2}$. In order to rely on fragmentation models studied at $\mathrm{e^+e^-}$ colliders, the variable z in neutrino charmed hadron production is evaluated in the W-nucleon centre-of-mass frame.

Experimentally, the fragmentation variable z can not be determined on an event-by-event basis, because the four vector of the charm quark and—in our case—of the charmed hadron can not be measured directly. However, the charmed hadron decays into a muon, and instead of the "theoretical" fragmentation variable z an experimental fragmentation variable is introduced and defined by

$$z_l = E_{\mu 2}/(E_{\mu 2} + E_{\text{had}}), \qquad (1.46)$$

with E_{had} and $E_{\mu 2}$ as the energies of the hadronic final state and muon from charm decay, respectively. The variable z_l plays a role similar to z in describing the main energy dependence of the fragmentation process. Relations between z_l and z can be studied in MC simulations.

To describe the fragmentation of charm quarks in terms of the fragmentation function we must know the fractions of various types of charmed hadrons produced. The Fermilab E531 collaboration [50] determined the production fractions for the different types of charmed particles in a wide-band neutrino beam using nuclear emulsion as target and detector. The $\mathrm{D^+}$ and $\mathrm{D_s^+}$ events that could not be determined without ambiguity, were counted as $\mathrm{D^+}$ events. To correct for this bias, a reanalysis was done [51] which uses the various lifetimes of the charmed particles. The fractions found for neutrino energies larger

than 30 GeV are: $(58 \pm 6)\%$ D^0, $(26 \pm 6)\%$ D^+, $(7 \pm 5)\%$ D_s^+ and $(7 \pm 4)\%$ Λ_c^+. These results are compatible with the fractions obtained by CLEO [48], where charmed particles are produced in e^+e^- annihilation at a centre-of-mass energy of 10.55 GeV. The D_s^+ and Λ_c^+ fractions increase to 13% and 17%, and the D^0 and D^+ fractions decrease to 53% and 16%, respectively, for neutrino energies larger than 5 GeV. In our description according to Peterson *et al.* we use the reanalysed E531 production fractions.

1.4   Charmed hadron decay

The probability to obtain a muon from a charm quark c depends on a) the fragmentation of the quark to any charmed hadron and b) the subsequent decay of any such hadron into a muon. In Table 1.1 the properties of charmed particles as given by the 1998 Particle Data Group (PDG) [52] are shown. The muon branching ratios are not well known. By assuming lepton universality one can calculate from the electron branching ratios the muon ratios by taking into account their mass difference. The average muon branching ratio of charmed hadrons B_c can be written as

$$B_c = \sum_H P_H \frac{\Gamma_\mu^H}{\Gamma^H},\qquad(1.47)$$

where $P_H = \int_0^1 D_H(z)\mathrm{d}z$ is the probability to obtain a charmed hadron H from a c quark ($H = D^0$, D^+, D_s^+ and Λ_c^+) and where Γ_μ^H/Γ^H is the inclusive muonic branching ratio for the charmed hadron H. Using direct measurements alone and the reanalysed E531 data yields [51] $B_c = (9.19 \pm 0.85_{CF} \pm 0.41_{BR})\%$, where the first error is the contribution due to the charmed hadron species

Table 1.1: The values for mass, lifetime and the inclusive muon as well as electron branching ratio for the charmed particles from the 1998 PDG [52].

hadron	mass (GeV/c^2)	lifetime (10^{-12} s)	$\to \mu X$ (%)	$\to e X$ (%)
D^0	1.8645±0.0005	0.415±0.004	6.6±0.8	6.75±0.29
D^+	1.8693±0.0005	1.057±0.015	>14	17.2±1.9
D_s^+	1.9685±0.0006	0.467±0.017	>5.8	8^{+6}_{-5}
Λ_c^+	2.2849±0.0006	0.206±0.012	>2.0	4.5±1.7

fractions and the second error is due to the charmed semi-muonic branching ratios.

Finally, the neutrino cross-section for the production of opposite-sign dimuons via charm production in LO QCD is given by

$$\frac{\mathrm{d}^3\sigma^{\nu\ LO}}{\mathrm{d}x\mathrm{d}y\mathrm{d}z}(\nu\mathrm{N} \to \mu^-\mu^+\mathrm{X}) = \frac{\mathrm{d}^2\sigma^{\nu\ LO}}{\mathrm{d}x\mathrm{d}y}(E_\nu, x, y, m_c, \kappa, \alpha)D_{H/c}(z, \epsilon)B_c,$$

(1.48)

where the dependence on the parameters m_c, κ, α, ϵ, B_c and kinematical variables E_ν, x, y, z is given explicitly. The parameters can be determined by comparing data as a function of the kinematical variables with a model using the above given cross-section (Section 1.7.1).

1.5   Background processes

There are processes which have opposite sign dimuons in the final state, but have not been produced by neutrino charged current single charm production as described above. Due to small cross-sections or imposed kinematical cuts most of the background sources are found to be negligible. We can thus ignore the contribution of intermediate resonances or the production of neutral strange particles in the final state, pair production of charm particles, diffractive production of strange charmed mesons and coherent muon pair production.

A possible source of uncertainty arises from the contamination of a ν_μ beam with $\overline{\nu}_\mu$ and vice versa. To divide dimuon events into those from incident ν_μ or $\overline{\nu}_\mu$ usually a separation procedure is used in which it is assumed that the primary—so called "leading"—muon has larger transverse momentum with respect to the direction of the hadron shower than the secondary muon, from the charmed hadron decay. In the wide-band ν_μ beam used for CDHS and CHARM II [38–40] the contamination of $\overline{\nu}_\mu$ is sufficiently low to be neglected. However in the $\overline{\nu}_\mu$ wide-band beams this is not the case and the separation procedure is used. This results in a contamination of ν_μ events in the $\overline{\nu}_\mu$ sample of about 6% for both experiments. In the CCFR analyses [41, 42] a wide-band ν_μ beam was used where the contamination of $\overline{\nu}_\mu$ was taken into account. Using the separation procedure a 1.1% (32%) contamination in the ν_μ ($\overline{\nu}_\mu$) sample was found to be present. In our experiment the contamination of anti-neutrinos is sufficiently low, 1.6%, to be neglected.

The main background to opposite-sign dimuon events from charm production is due to muonic decay of pions and kaons produced either directly at the

CC vertex or during hadronic shower development. This background ranges from 6 to 19% for antineutrino events and from 13 to 24% for neutrino events, as can be seen in Table 1.2, where a summary is given of data samples from various experiments. For our analysis this fraction is found to be 22%, see Section 3.9.

1.6   Current status

A number of experimental groups have studied neutrino charmed particle production [38–42, 53–59]. The currently most relevant results are obtained by the CDHS [38], CHARM II [39, 40], and CCFR collaboration [41]; all three performed a leading-order QCD analysis. CCFR also did an incomplete next-to-leading-order (NLO) analysis [42]. Table 1.2 gives the sizes of the samples used in the dimuon analyses of these experiments as well as backgrounds. In the CCFR(LO) analysis the dimuon cross-section was corrected for Callan-Gross violation, which was not done by CDHS or CHARM II.

The CDHS experiment used CERN narrow-band (anti-)neutrino beam to measure the total (anti-)neutrino cross section and performed precision electroweak and structure-function measurements with wideband beams during the early 1980s. Neutrino events from both narrow-band and wideband neutrino beams are used for their dimuon analysis. The experiment used a detector consisting of toroidally magnetised iron plates sandwiched between planes of scintillator and drift chambers. The momentum and charge-sign of the muons were determined by the bend in the magnetic field, with an average resolution of 9%. The hadronic energy resolution of the calorimeter varied, depending on the segmentation of the iron, from $\sigma_{\rm had}/E_{\rm had} \sim 0.58/\sqrt{E_{\rm had}}$ to $0.70/\sqrt{E_{\rm had}}$.

The dimuon results from the CCFR experiment includes data taken in 1985 and 1987 and runs at Fermilab. The wideband neutrino beam had no sign selection, resulting in a large contamination (13%) of $\overline{\nu}_\mu$ in the ν_μ beam. The detector is constructed as a target calorimeter followed by a toroid muon spectrometer. The calorimeter consists of iron plates interspersed with scintillators and drift chambers, with a hadronic energy resolution $\sigma_{\rm had}/E_{\rm had} = 0.89/\sqrt{E_{\rm had}}$. The toroid spectrometer has five sets of driftchambers for muon tracking as well as hodoscopes for triggering; its momentum resolution is $\Delta p/p = 11\%$.

The CHARM II experiment collected data during the period 1987-1991, using the same wideband neutrino beam as the CDHS experiment. This experiment was optimised for detection of electrons. The detector's target was composed of 48 mm thick plates of glass and interspersed between the plates were

Table 1.2: Summary of data samples from neutrino and anti-neutrino induced dimuon events for the experiments discussed in the text. The total number of events without background subtraction and the percentage of background events is given.

experiment	ν_μ induced		$\overline{\nu}_\mu$ induced	
	events	Bkgnd	events	Bkgnd
CDHS [38]	11041	13%	3684	6%
CCFR(LO) [41]	5044	16%	1062	11%
CCFR(NLO) [42]	5030	16%	1060	11%
CHARM II [39, 40]	4111	24%	871	19%

streamer tubes, providing digital and analog hit information. Between every five sets of plates and streamer tubes were scintillation counters. The resolution for hadronic showers using the streamer tubes was $\sigma_{\text{had}}/E_{\text{had}} \sim 0.52/\sqrt{E_{\text{had}}}$. The muon spectrometer consisted of magnetised iron toroids instrumented with scintillation counters and drift chambers. The resolution was $\Delta p/p = 13\%$ at 20 GeV/c.

In Table 1.3 the dimuon charm results of the above experiments are given. We note that the parameter $\epsilon_{CS\prime}$ is not the original parameter of the Collins-Spiller fragmentation function of Equation 1.43, but a parameter of the slightly modified fragmentation function

$$D_{H/Q}(z, \epsilon_{CS\prime}) = f_H^{CS\prime} \left(\frac{1-z}{z} + \frac{2-z}{1-z}\epsilon_{CS\prime} \right) (1+z)^2 \left(1 - \frac{1}{z} - \frac{\epsilon_{CS\prime}}{1-z} \right)^{-2}. \tag{1.49}$$

We note that the factor $(1 + z^2)$ has changed to $(1 + z)^2$, which causes a slight change in the shape of the function. The larger changes are absorbed in the normalisation factor $f_H^{CS\prime}$. We also note that the errors on the CCFR(LO) and CCFR(NLO) values are correlated, because the same data set was used in both analyses.

The following remarks can be made about the parameters:

- The charm quark mass value m_c from the CCFR(NLO) analysis differs at the 1.3 σ level from the CCFR(LO) result. The CHARM II analysis—performed at LO—finds a value which is compatible with both CCFR results.

1. Charm production in neutrino charged current interactions

Table 1.3: Comparison of neutrino dimuon charm results. Statistical and systematic errors are added in quadrature and symmetrised using $\sigma^2 = (\sigma_-^2 + \sigma_+^2)/2$ except for ϵ_P and $\epsilon_{CS'}$ of the CCFR experiment which are statistical only. For CHARM II [39, 40] and CCFR [41, 42], $\langle z \rangle$ is calculated from the Peterson *et al.* fragmentation function [46] using the fitted value of ϵ_P. For CDHS [38], the range for ϵ_P is obtained from the determination of $\langle z \rangle$. All these derived numbers are given in parentheses.

	CDHS	CCFR(LO)	CCFR(NLO)	CHARM II
		0.245 ± 0.005	0.203	
c quark production				
m_c (GeV/c^2)	1.50 (fixed)	1.31 ± 0.24	1.70 ± 0.19	1.79 ± 0.38
κ	0.48 ± 0.08^a	0.373 ± 0.048	0.477 ± 0.058	0.388 ± 0.095
α	0 (fixed)	2.50 ± 0.65	-0.02 ± 0.65	1.12 ± 1.29
c quark fragmentation				
ϵ_P	([0.02,0.14])	0.20 ± 0.04	0.20 ± 0.04	0.072 ± 0.017
$\epsilon_{CS'}$	([0.02,0.46])	^{b}	0.81 ± 0.14	0.19 ± 0.07
$\langle z \rangle$	0.68 ± 0.08	(0.56 ± 0.02)	(0.569 ± 0.010)	(0.66 ± 0.02)
charmed hadron decay				
B_c (%)	8.4 ± 1.5^a	10.5 ± 0.9	10.91 ± 0.85	9.05 ± 0.98

^{a}Corrected for the PDG98 [52] values of V_{cd} and V_{cs}.

^{b}Not available.

- The strange quark magnitude following from κ is found to be smaller than unity, indicating that the sea is not SU(3) symmetric. Also the CCFR(LO) and CCFR(NLO) results of κ are different at the 1.4 σ level. In the CCFR(LO) analysis no Q^2 dependence of κ is found.

- The positive value of α from the CHARM II and CCFR(LO) analyses indicate a possible tendency that in LO QCD the strange sea is softer than the non-strange sea. The strangeness distribution resulting from the CCFR(NLO) and CCFR(LO) analyses can be seen in Figure 1.6. The fact that the NLO distribution is about twice as large as the one at LO can be attributed to the same behaviour for the total quark sea distribution $x\bar{q}(x)$, as shown in Figure 1.7, and thus is not special for strangeness.

24
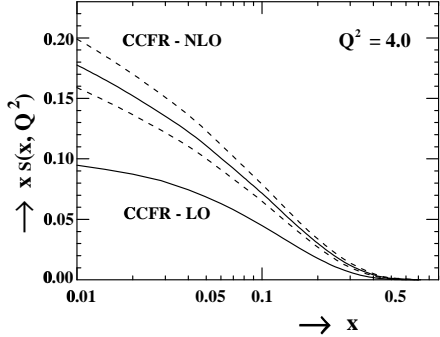
Figure 1.6: The strangeness distribution $xs(x, Q^2 = 4.0 \text{ GeV}^2/c^2)$ determined by the CCFR collaboration [42] at NLO and LO QCD. The dashed curves around the NLO curve indicate the $\pm 1\sigma$ uncertainty in the distribution.
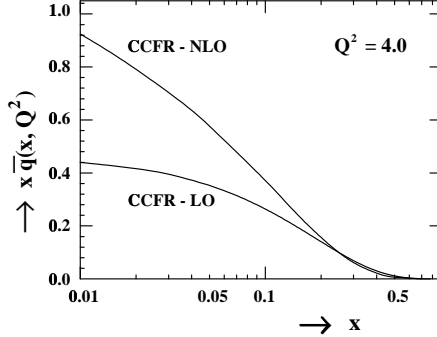
Figure 1.7: Same as Figure 1.6 for the quark sea distribution $x\overline{q}(x, Q^2 = 4.0 \text{ GeV}^2/c^2)$

- The notable discrepancy between mean values of the charm quark fragmentation momentum $\langle z \rangle$, determined by CHARM II and CCFR(LO), can be interpreted as due to an energy dependence of this parameter. The mean visible neutrino energies of the CHARM II and CCFR(LO) dimuon samples are about 115 and 200 GeV, and the mean visible energies for anti-neutrinos are about 70 and 155 GeV, respectively.

- The values of B_c from all experiments are consistent, providing a good overall check of the physics models. The values agree with an indirect determination $B_c = (9.19 \pm 0.94)\%$ as described in Section 1.4.

Figure 1.8 shows the ratio R_{vis} of CC charm dimuon to single muon cross-section for ν_μ and $\overline{\nu}_\mu$, as a function of the neutrino energy. With these curves and the number of expected CC events in an experiment, one can estimate the number of charm dimuon events. These figures are based on the parameters from the CDHS, CCFR(LO) and CHARM II analyses for the kinematical domain covered by the CHARM II analysis. The discrepancies between the curves are of the same order as the errors on the individual curves.

By assuming the CKM matrix elements V_{cd} and V_{cs} to be known one can determine the values of m_c, α, κ, B_c and ϵ. When the CKM matrix elements

# 1. Charm production in neutrino charged current interactions
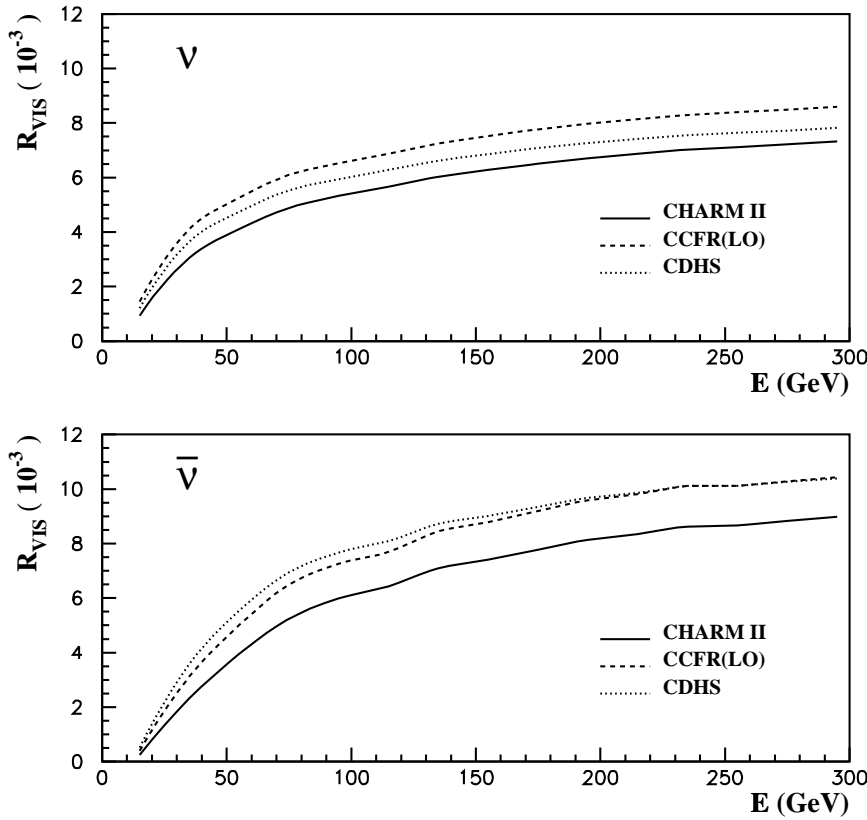
Figure 1.8: Opposite-sign dimuon to single muon cross-section ratio R_{vis} for $Q^2 > 6 \text{ GeV}^2/c^2$ and $\nu > 15$ GeV, approximately covering the CHARM II data sample for $E_\nu > 35$ GeV, for neutrinos (top) and antineutrinos (bottom). The various curves correspond to the cross-section ratios calculated with the parameters resulting from the CHARM II [39, 40], CCFR(LO) [41] and CDHS analyses [38]. Picture taken from [40].

are left as free parameters one measures the values of m_c, α, $|V_{cs}|^2 B_c \kappa/(\kappa + 2)$, $|V_{cd}|^2 B_c$ and ϵ. The sensitivity to $|V_{cd}|$ is increased by isolation of the valence quark contribution to charm production. This can be done by either measuring the charm cross section at high x, where the sea quark contributions are small,

or by subtracting the anti-neutrino cross section from the neutrino cross section, as can be seen in Equation 1.30. Using an external value of B_c one can extract the value of the CKM matrix element $|V_{cd}|$. The CCFR(LO) analysis gives a value of 0.209 ± 0.012, the CHARM II analysis 0.209 ± 0.017, and CCFR(NLO) 0.232 ± 0.019. These values compare well with the 1998 PDG value [52], 0.221 ± 0.002, which is determined from measurements of all individual matrix elements and the unitarity constraint on the CKM matrix assuming three generations. Using external values of both B_c and κ one can extract the value of the CKM matrix element $|V_{cs}|$. The CCFR collaboration [60] performed an independent measurement of the strange sea content, by using charged current ν_μ and $\overline{\nu}_\mu$ induced events where the dimuon events are removed from the sample. The strange sea content as determined by κ is found to be $\kappa = 0.453 \pm 0.106^{+0.028}_{-0.096}$, and does not show a significant x dependence. Using this value of κ, an external value of B_c and the value of $|V_{cs}|^2 B_c \kappa/(\kappa + 2)$ measured by CCFR(NLO), a value of $|V_{cs}| = 1.05 \pm 0.10^{+0.07}_{-0.11}$ is found, which is consistent with the 1998 PDG value [52] of 0.9745 ± 0.0005.

In the CCFR(NLO) analysis no shape difference between the $xs(x)$ and $x\overline{s}(x)$ distributions is found. In the same analysis no significant difference in the muonic decays of charmed particles and anti-particles is established.

1.7 Monte Carlo generators

To confront experimental data with the theory outlined in this chapter, it is necessary to bring the theory in "experimental form". This implies that a) essentially all instrumental effects including selections and cuts have to be applied to the theoretical cross section, or b) the experimental data have to be "corrected" for the instrumental effects. In both cases one needs a full experimental Monte Carlo (MC) simulation [61] of the experiment, including all relevant physics and instrumental aspects. Below we summarise the main aspects of the MCDIMUON generator specifically designed for dimuon charm analysis, and the CHORUS MC generator JETTA used for most of the CHORUS analysis. The neutrinos produced by the neutrino beam generator GBEAM (Section 3.7) are used as input for both event generators.

1.7.1 MCDIMUON

The dimuon event generator MCDIMUON—developed by Vincent Lemaître [39, 40] to describe opposite sign dimuon events with the CHARM II detector—

1. Charm production in neutrino charged current interactions

produces a data set of opposite sign dimuons according to the theoretical model given in this chapter, with the following input and assumptions:

- The nucleon is considered to be at rest in the laboratory frame and no Fermi motion or nuclear binding energy is taken into account. No nuclear effects are included, except the neutron (d-quarks) excess present in our target.

- The CTEQ 3L parton distribution functions [27] of the total valence quark distribution function $xq_{\mathrm{val}}(x, Q^2)$ (see Equation 1.33) and the total anti-quark distribution function $x\bar{q}(x, Q^2)$ (see Equation 1.34) are taken from the CERN PDFLIB library [43].

- $s(x, Q^2) = \bar{s}(x, Q^2)$.

- The masses of the charm quark and the nucleon are not neglected in the hard-scattering cross-section. This cross-section is given by Equation 1.30, with the modified scaling variable according to Equation 1.28. The initial quark masses are assumed to be $m_d = 0.01$ GeV/c^2 and $m_s = 0.2$ GeV/c^2, for the d and the s quark, respectively. The masses used are a bit larger than the ones given by the 1998 PDG [52] ($m_d = 3-9$ MeV/c^2 and $m_s = 60 - 170$ MeV/c^2). However, when looking at Figure 1.4 one can see that even when using these larger masses the effect of initial quark masses on the slow-rescaling variable (see Equation 1.31) is smaller than 0.5% for $Q^2 > 5$ GeV^2/c^2, and negligible compared to the target mass effect.

- The fragmentation of charm quarks is described by the Peterson *et al.* fragmentation function of Equation 1.42 being the same for all charmed hadrons produced. Excited charmed hadrons are not taken into consideration. The transverse momentum distribution of the charmed hadron is described by Equation 1.45.

- A correction for radiative effects is calculated for the inclusive charged current cross-section using the prescription of Bardin [31], and assumed to be the same for the (semi-inclusive) dimuon cross-section.

- The decay of charmed hadrons only depends on the phase space. Anisotropies due to decay matrix elements are not taken into account.

The MCDIMUON cross section calculation uses values of various parameters as shown in Table 1.4 for given values of the parameters m_c, κ, α, ϵ_P and

28

Table 1.4: The values of various parameters used for the production and decay probabilities of charmed hadrons.

parameter			fragmentation		muonic decay branching ratios		muonic decays	
$\beta \ (\mathrm{GeV}/c)^{-2}$	1.70	$c \to \mathrm{D}^0$	0.60	B_{D^0}	0.081	$\mathrm{D} \to \pi\mu\nu$	0.07
$|V_{cd}|$	0.221	$c \to \mathrm{D}^\pm$	0.26	$B_{\mathrm{D}^\pm}$	0.167	$\mathrm{D} \to \mathrm{K}\mu\nu$	0.60
$|V_{cs}|$	0.975	$c \to \mathrm{D}_{\mathrm{s}}^\pm$	0.07	$B_{\mathrm{D}_{\mathrm{s}}^\pm}$	0.110	$\mathrm{D} \to \mathrm{K}^*\mu\nu$	0.33
		$c \to \mathrm{D}^{*0}$	0.00	$B_{\Lambda_{\mathrm{c}}}$	0.045	$\mathrm{D} \to \mathrm{K}\pi\mu\nu$	0.00
		$c \to \mathrm{D}^{*\pm}$	0.00			$\Lambda_{\mathrm{c}} \to \mathrm{p}\mu\nu$	0.02
		$c \to \mathrm{D}_{\mathrm{s}}^*$	0.00			$\Lambda_{\mathrm{c}} \to \Lambda\mu\nu$	0.38
		$c \to \Lambda_{\mathrm{c}}$	0.07			$\Lambda_{\mathrm{c}} \to \mathrm{pK}\mu\nu$	0.31
						$\Lambda_{\mathrm{c}} \to \Lambda\pi\mu\nu$	0.29

D stands for $\mathrm{D}^\pm$, D^0, $\overline{\mathrm{D}}^0$ and $\mathrm{D}_s^\pm$.

K^*, D^{*0} and $\mathrm{D}^{*\pm}$ stand for $\mathrm{K}^*(892)$, $\mathrm{D}^*(2010)^0$ and $\mathrm{D}^*(2010)^\pm$, respectively.

The decay into $\pi\mu\nu$ stands for all Cabibbo-suppressed modes.

B_c. The values of $|V_{cd}|$, $|V_{cs}|$, the muon branching ratios and specific muonic decays are derived from the 1994 PDG [62], which are consistent with the values from the 1998 PDG [52]. The weighted-average muonic-decay branching ratios are calculated using all semileptonic $\mathrm{D}^\pm$, D^0 and $\overline{\mathrm{D}}^0$ decay results. The prescription of the 1994 PDG was followed for this averaging, taking the mass difference between electron and muon into account. The numbers in the fragmentation column are based on [51], and the value of β, describing the transverse momentum distribution of the charmed hadron (Equation 1.45), is determined by averaging the values used by E531 [58], CDHS [38] and CCFR [41].

The selection of neutrino type and momentum at the creation vertex are given by GBEAM (see Section 3.7), properly representing real data probabilities [63]. The following steps are taken:

Structure function parametrisation
The total valence quark and anti-quark distribution functions (Equations 1.33 and 1.34) are kept constant, while the parametrisations of the $\bar{u}$, $\bar{d}$, and $\bar{s}$ distribution functions are redefined using the two additional parameters. These are κ, related to the strange quark content, Equation 1.35, and α, the strangeness shape parameter, Equation 1.36.

1. Charm production in neutrino charged current interactions

Hard scattering

For a given neutrino energy, E_ν, and the nucleon being at rest in the laboratory system, neglecting Fermi motion, one calculates the kinematics of the charged current reaction. The kinematical variables are drawn at random according to a uniform phase space density; in particular x and y are drawn from a uniform distribution in the interval [0,1] and the angle of the primary muon in the plane perpendicular to the neutrino direction is drawn from a uniform distribution in the [0,2π] interval. For each triplet (E_ν, x, y), two weights are associated with the event: the first one, P_{CC}, is proportional to the inclusive charged current cross-section and the second one, $P_{2\mu}$, is proportional to the cross-section for a dimuon final state. Explicitly

$$P_{cc} \propto \frac{\mathrm{d}^2\sigma^{cc}}{\mathrm{d}x\mathrm{d}y}, \tag{1.50}$$

according to Equation 1.21 and

$$P_{2\mu} \propto \frac{\mathrm{d}^3\sigma^{2\mu}}{\mathrm{d}x\mathrm{d}y\mathrm{d}z}(E_\nu, x, y, m_c, \kappa, \alpha) D_{H/c}(z, \epsilon) B_c, \tag{1.51}$$

according to Equation 1.48. The fragmentation variable z is drawn from a uniform distribution in the [0,1] interval and it specifies the kinematics of the charmed hadron.

Fragmentation of the c quark

The fragmentation is described in two steps. In the first step a charmed hadron is selected according to the probabilities in Table 1.4. Assuming that the fragmentation function is the same for all charmed hadrons, one determines from the fragmentation variable z the momentum P_D^* of the charmed hadron in the W-nucleon centre-of-mass system. The hadron momentum in the laboratory system is given by

$$P_{\mathrm{D}} = \gamma\beta E_{\mathrm{D}}^* + \gamma P_{\mathrm{D}}^*, \tag{1.52}$$

where the Lorentz parameters are given by

$$\gamma = \frac{\nu + M}{\sqrt{W^2}}, \tag{1.53}$$

30

and

$$\gamma\beta = \frac{\sqrt{(\nu + M)^2 - W^2}}{\sqrt{W^2}}. \tag{1.54}$$

The charmed hadron transverse momentum with respect to direction of the W-boson is drawn from the distribution of Equation 1.45. The azimuthal angle is drawn from a uniform distribution in the $[0,2\pi]$ interval.
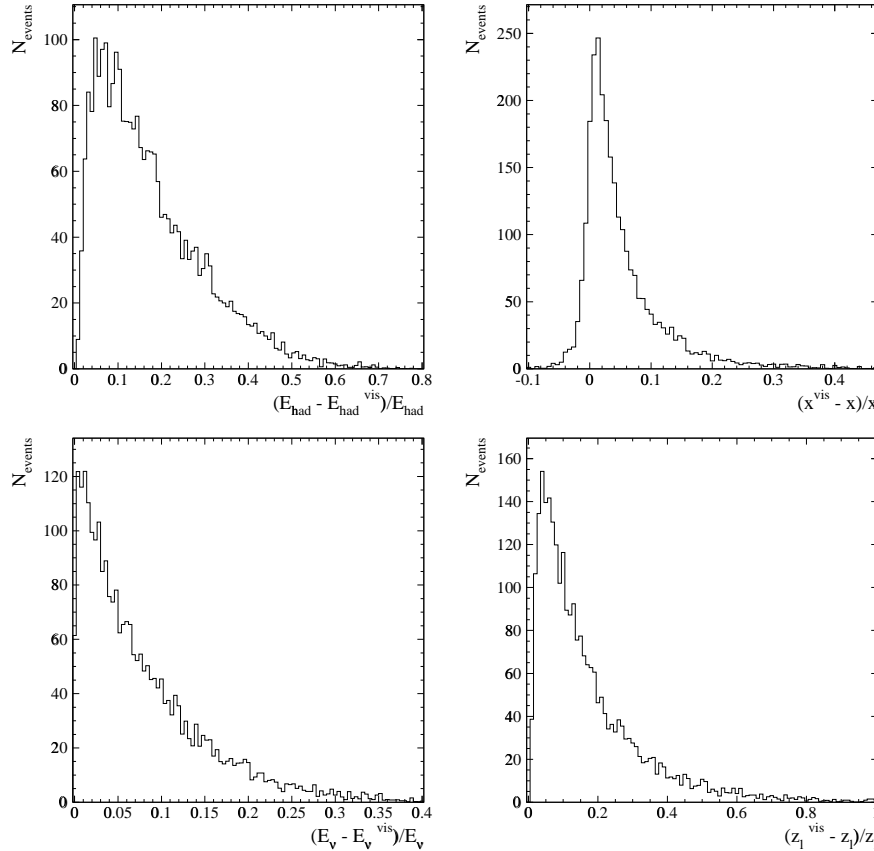

Figure 1.9: Relative influence of the undetected neutrino from charm decay on the variables E_{had}, x, E_ν and z_l for MCDIMUON events.

Charmed hadron decay

Three or four body decay of charmed hadrons is simulated taking into account the branching ratios B given in Table 1.4. We note that only the relative factors of the branching ratios B are important because together with the fragmentation probabilities it is normalised to the average muon branching ratio B_c (see Equation 1.47).

The four-vectors of the decay products are determined in the centre-of-mass system of the parent particle and calculated using phase-space only. The results for the neutrino and muon are then transformed to the laboratory system by the appropriate Lorentz transformation.

The energy and momentum of the hadronic shower is calculated by assuming energy and momentum conservation, and using the kinematics of the nucleon, incident neutrino, primary muon, secondary muon and the neutrino from charmed hadron decay. This method provides a reasonable estimate for the four momentum of the hadronic shower although the fragmentation of the charm quark and the nucleon remnants are not simulated in detail.

When comparing dimuon MC with real data events, one must take into account that the neutrino from charm decay escapes detection. Therefore kinematical variables with the "vis" label, standing for "visible", are introduced to indicate that the corresponding value of the kinematical variable is only approximate. In Figure 1.9 one can see the relative influence of this effect on the kinematical variables E_{had}, x, E_ν and z_l. The distributions are made using the MCDIMUON event generator utilising our final results, as given in Table 4.6, and using the same selections as for the real data (Section 3.6). The relative influence on E_{had} is presented because the neutrino from charm decay has a direct effect on the measurement of the energy of the hadronic final state. The average energy of the neutrino from charm decay is about 9 GeV and its distribution is peaked at low energies and falls off towards higher energies. On average about 17% of E_{had} and 8% of E_ν are taken up by this neutrino. The relative effect on x and z_l is about 5 and 19%, respectively.

1.7.2 JETTA

The event generator JETTA (based on Jetset [64, 65], Lepto [66] and Tauola [67–69] with some modifications specific for CHORUS [70]) generates neutrino-induced MC events, including opposite-sign dimuon events. The CERN neutrino beam is simulated by GBEAM and with these neutrinos as input JETTA produces the hard scattering neutrino-nucleon interaction including the

Table 1.5: Muonic decay channels and relative branching ratios (BR) for the charmed particles implemented in JETTA. The decays to "μ^+anything" are used as a normalisation.

channel	BR	channel	BR
$D^+ \to \mu^+$anything	1.000	$D^0 \to \mu^+$anything	0.448
$D^+ \to \mu^+\nu_\mu\overline{K}^0$	0.407	$D^0 \to \mu^+\nu_\mu K^-$	0.198
$D^+ \to \mu^+\nu_\mu\overline{K}^*(892)^0$	0.378	$D^0 \to \mu^+\nu_\mu\overline{K}^*(892)^-$	0.157
$D^+ \to \mu^+\nu_\mu\overline{K}^0\pi^0$	0.029	$D^0 \to \mu^+\nu_\mu\overline{K}^0\pi^-$	0.012
$D^+ \to \mu^+\nu_\mu K^-\pi^+$	0.029	$D^0 \to \mu^+\nu_\mu K^-\pi^0$	0.012
$D^+ \to \mu^+\nu_\mu\overline{K}^*(892)^0\pi^0$	0.064	$D^0 \to \mu^+\nu_\mu\overline{K}^*(892)^0\pi^-$	0.023
$D^+ \to \mu^+\nu_\mu\overline{K}^*(892)^-\pi^+$	0.064	$D^0 \to \mu^+\nu_\mu\overline{K}^*(892)^-\pi^0$	0.023
$D^+ \to \mu^+\nu_\mu\pi^0$	0.006	$D^0 \to \mu^+\nu_\mu\pi^-$	0.012
$D^+ \to \mu^+\nu_\mu\eta$	0.006	$D^0 \to \mu^+\nu_\mu\rho(770)^-$	0.012
$D^+ \to \mu^+\nu_\mu\eta'(958)$	0.006	$\Lambda_c^+ \to \mu^+$anything	0.262
$D^+ \to \mu^+\nu_\mu\rho(770)^0$	0.006	$\Lambda_c^+ \to \mu^+\nu_\mu\Lambda^0$	0.105
$D^+ \to \mu^+\nu_\mu\omega(783)$	0.006	$\Lambda_c^+ \to \mu^+\nu_\mu\Sigma^0$	0.029
$D_s^+ \to \mu^+$anything	0.465	$\Lambda_c^+ \to \mu^+\nu_\mu\Sigma^*(1385)^0$	0.029
$D_s^+ \to \mu^+\nu_\mu\eta$	0.116	$\Lambda_c^+ \to \mu^+\nu_\mu n$	0.017
$D_s^+ \to \mu^+\nu_\mu\eta'(958)$	0.116	$\Lambda_c^+ \to \mu^+\nu_\mu\Delta(1232)^0$	0.012
$D_s^+ \to \mu^+\nu_\mu\phi(1020)$	0.174	$\Lambda_c^+ \to \mu^+\nu_\mu p\pi^-$	0.035
$D_s^+ \to \mu^+\nu_\mu K^+K^-$	0.029	$\Lambda_c^+ \to \mu^+\nu_\mu n\pi^0$	0.035
$D_s^+ \to \mu^+\nu_\mu K^0\overline{K}^0$	0.029		

fragmentation of the produced quarks, and the decay of short-lived particles (like τ, $D^\pm$, D^0, $\overline{D}^0$, $D_s^\pm$ and $\Lambda_c^\pm$).

JETTA is developed to simulate an inclusive CC data sample and to deal correctly with interactions where the lepton mass can not be neglected. The nucleons in the nucleus have Fermi motion and the kinetic energy distribution of the nucleon is given by $dn/dE_{kin} \propto \sqrt{E_{kin}}$, with a maximum kinetic energy of 27 MeV. The parametrisations of the quark distribution functions are taken from EHLQ [71,72], which give the proper total neutrino cross-section. JETTA describes neutrino interactions with $W^2 > 2\,\mathrm{GeV}^2/c^2$, and initial and final state radiations are not included.

The semileptonic branching ratios of the charmed hadrons are explicitly given in Table 1.5. Not all branching ratios are known; a fair amount of ex-

trapolation from our knowledge of the inclusive semileptonic branching ratio and the exclusive branching ratios for low multiplicities is involved to obtain the relevant numbers for the channels with higher multiplicity. A simple $V - A$ matrix element—in the limit that decay product masses may be neglected and that quark momenta can be replaced by hadron momenta—is used to calculate the four-vectors of the decay products.

In order to take care of heavy quark production and fragmentation the following modifications have been introduced:
1) The threshold in the charm production cross-section due to the charm quark mass of 1.35 GeV/c^2, is taken into account by multiplying the CC cross-section for "light" quarks with $(M + m_c + m_{\rm rem} + m_d)^2/W^2$, where M, m_c, $m_{\rm rem}$ and m_d are the masses of the nucleon, charm quark, target remnant and the down quark, respectively. It has to be noted that the quark distribution functions in the charm cross-section are given as a function of x and not χ, as is the case in the LO QCD formalism of Equation 1.30.
2) String fragmentation [73] is used for the quark hadronisation. For charm quarks the Peterson et $al.$ fragmentation is utilised with $\epsilon_P = 0.072$, the value obtained by CHARM II [39, 40].

1.7.3   Discussion

Both generators described above are used in our analysis. JETTA is utilised for the calculation of detector effects in Chapter 3 while MCDIMUON is used in a fitting procedure for the extraction of the physics information from the experimental data in Chapter 4. To test the overall consistency between the two MC generators a comparison of distributions essential for our study are shown in Figure 1.10 for $x^{\rm vis}$, $y^{\rm vis}$, $E_\nu^{\rm vis}$ and $z_l^{\rm vis}$. The same event selection as for real data is employed (Section 3.6) and all distributions are normalised with a single fixed constant.

In general the distributions shown in Figure 1.10 are compatible, although the MCDIMUON $x^{\rm vis}$ distribution is more peaked at lower values than with JETTA, for the $y^{\rm vis}$ and $E_\nu^{\rm vis}$ distributions it is just the other way around. The difference in the $E_\nu^{\rm vis}$ distributions and $x^{\rm vis}$ are mostly due to the differences in input distributions. Although the projected distributions are comparable, it is not excluded that in certain regions of the four-dimensional phase-space the MCDIMUON and JETTA distributions differ significantly. Although in JETTA the threshold behaviour of the charm quark production is not properly taken into account, the effects appear to be negligible in the projected distribu-
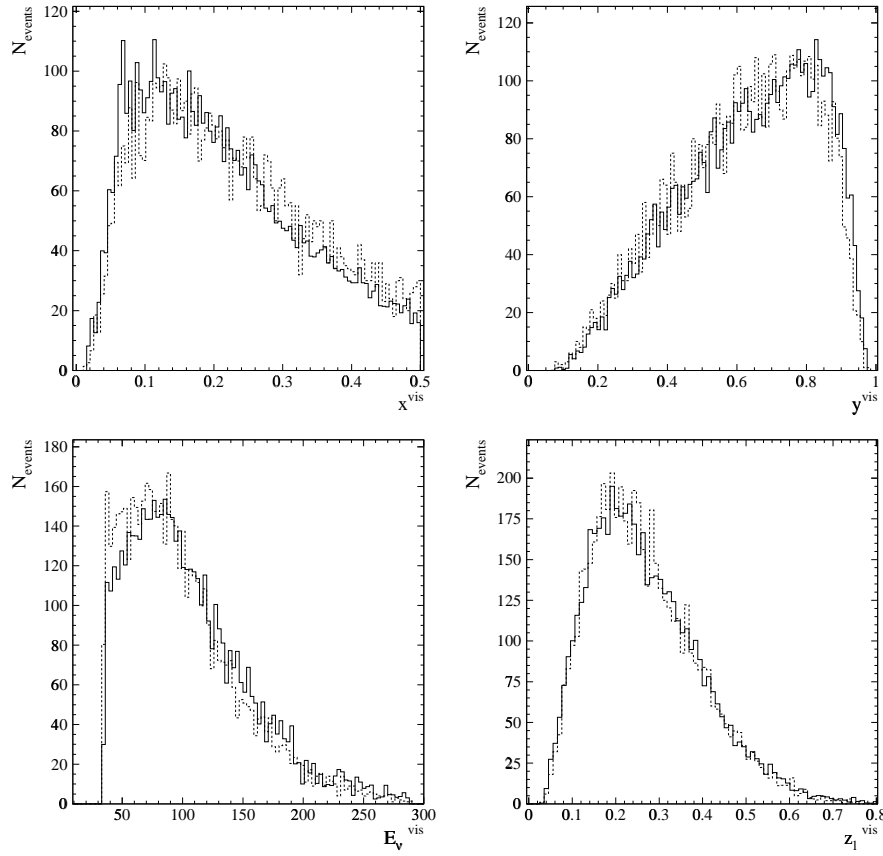
**Figure 1.10**: MCDIMUON (solid line) and JETTA (dashed line) distributions of x^{vis}, y^{vis}, E_ν^{vis} and z_l^{vis}.

tions. We believe that, even though the distributions are not fully compatible, the use of two different MC chains—one for the evaluation of corrections, and the other one for the extraction of the physics information—is justified for our present work.

1. Charm production in neutrino charged current interactions

36

Chapter 2

CHORUS apparatus

The CHORUS (CERN Hybrid Oscillation Research apparatUS) detector has been primarily designed to search for neutrino oscillations in the $\nu_\mu \to \nu_\tau$ appearance channel with the CERN Super Proton Synchrotron (SPS) Wide Band Neutrino Beam (WBB). The experimental setup consists of a large emulsion target, scintillating fibre tracker planes with opto-electronic readout, a set of trigger hodoscope planes, an aircore magnet, a calorimeter based on a lead-scintillating-fibre technique and a muon spectrometer.

A trigger system selects neutrino interactions in the emulsion target region and in other parts of the detector. In this chapter the CHORUS detector is described with special emphasis on the neutrino beam, the calorimeter, the muon spectrometer and the trigger, which are important for the study of charm production in deep inelastic neutrino scattering presented in this thesis. A description of the data acquisition and the online monitoring system complete the chapter.

2.1 Conceptual design

The signature for $\nu_\mu \to \nu_\tau$ oscillation in the CHORUS experiment is the explicit detection of the vertex in the charged current (CC) interaction $\nu_\tau N \to \tau^- X$, in combination with the subsequent decay topologies of the short-lived τ^- (mean life $\tau = 291$ fs). An event is shown schematically in Figure 2.1. The main τ^- decay channels relevant for the search are the one-prong decays (the "kink" events): $\tau^- \to \mu^- \overline{\nu}_\mu \nu_\tau$, and $\tau^- \to (hadron^-)(n\pi^0)\nu_\tau$, where $(hadron^-)$ can be a π^- or K^- often accompanied by zero or more neutral pions indicated by $(n\pi^0)$.
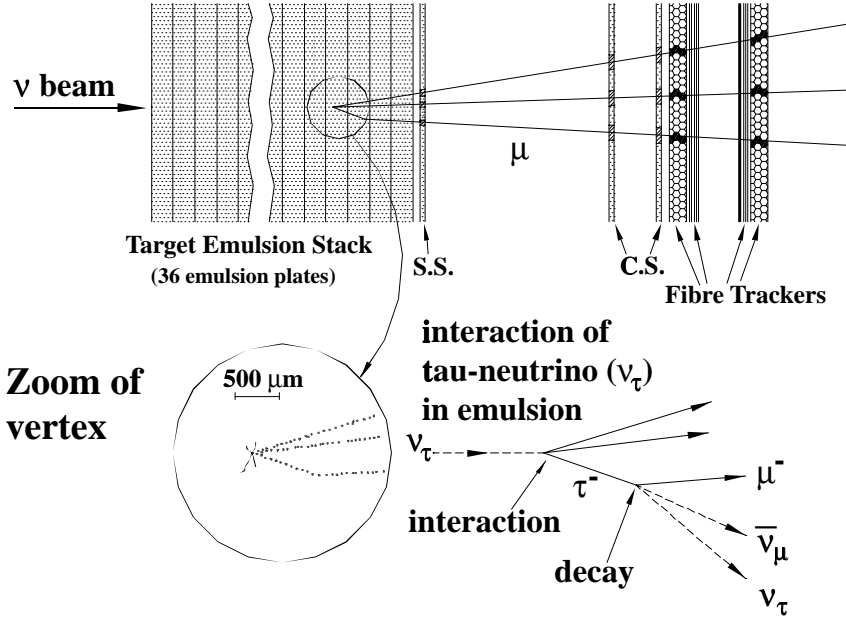
Figure 2.1: Schematics of a ν_τ charged current interaction in the emulsion target, followed by the subsequent decay of the τ^-. The interface emulsion sheets—important elements in the tracking—are labelled CS and SS, respectively.

Also the three-prong decay (the "star" events): $\tau^- \to (\pi^+\pi^-\pi^-)(n\pi^0)\nu_\tau$ is considered. The branching ratios of these decays are 17.4%, 49.5% and 14.6%, respectively [52]. Due to limitations the experimental setup the decay to electrons is not considered.

At the typical energies of the WBB, the τ leptons produced—in the case of oscillations—have an average flight path of order 1 mm.

CHORUS adopted the "hybrid" approach of combining emulsion and electronic detection techniques. A schematic diagram of the CHORUS apparatus is presented in Figure 2.2.

For the neutrino oscillation search (different from the work described in this thesis) the 770 kg nuclear emulsion target plays a central role. Nuclear emulsions provide three dimensional spatial information with a resolution of
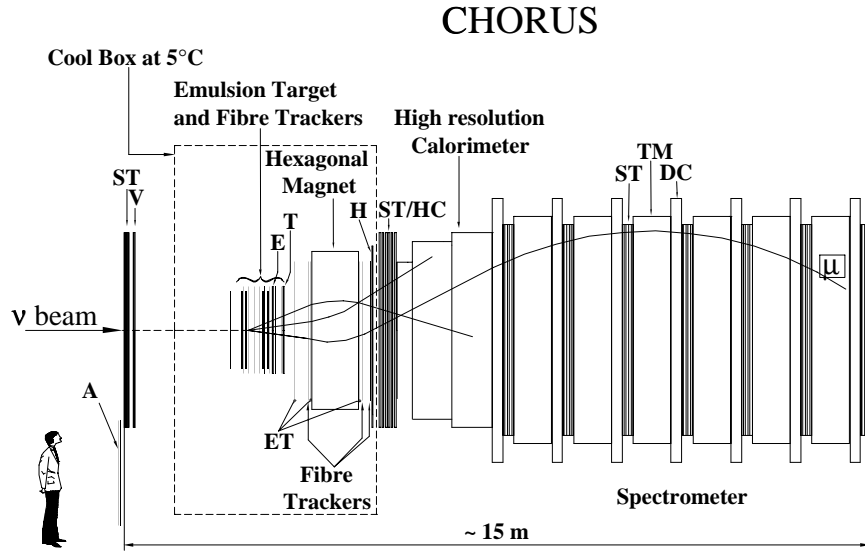
CHORUS

Figure 2.2: Schematic diagram (side view) of the CHORUS detector. The trigger and veto hodoscopes are denoted by A, V, E, T, H, while ST, TM and DC stand for streamer tubes, iron toroidal magnets and drift chambers, respectively, of the muon spectrometer system. The detector upgrades in 1996 on the emulsion trackers and honeycomb chambers are denoted by ET and HC, respectively. In the actual setup, individual modules are mounted vertically while the central axis of the apparatus is inclined at 42 mrad to match the neutrino beam axis.

the order of 1 μm, as well as a high hit density of 300 hits/mm. They are unique in the unambiguous detection of short-lived particles, with a flight path of order 1 mm.

Downstream of the emulsion target are the electronic detectors (Figure 2.2). They provide measurements of the kinematical variables and track predictions crucial for a) the selection of events for emulsion scanning, and b) the suppression of background events resembling the typical decay topologies. The fibre tracker system provides accurate trajectory predictions backward to the emulsion target. A two-track resolution of about 500 μm is crucial for full event reconstruction with high efficiency. Together with a hexagonal aircore magnet,

the fibre tracker also allows to measure the charge and momentum of traversing particles. The calorimeter provides high resolution measurements for the energies and directions of the hadrons and electrons, as well as intermediate tracking information for the muon. The charge and the momentum of muons are measured in the muon spectrometer.

The trajectories of charged particles reconstructed in the fibre tracker are traced back through thin interface emulsion sheets. These are placed directly downstream of the emulsion target, where the scanning starts. Once track segments are found in these interface sheets one can extrapolate with high accuracy into the emulsion target, to locate the vertex positions. Using the information given by the electronic detectors, events with kinematics close to the ν_τ charged current interactions, N_{ν_τ}, can be preselected out of the background of ν_μ interactions, N_{ν_μ}, (expected ratio $N_{\nu_\tau}/N_{\nu_\mu} \sim 10^{-5}$). In this way the required scanning time for the emulsions is reduced by a factor of about 10. Once events with the typical decay topologies are located in the emulsion target, further kinematic reconstruction and particle identification provide the constraints to differentiate between the τ^- signals and the background events which show similar topologies (charm decays and elastic scattering of hadrons).

The CHORUS coordinate system is a right-handed Cartesian system where the x-axis is the horizontal projection of the neutrino beam axis, the z-axis points vertically upwards, and the y-axis is horizontal and points approximately along the North-South axis from Gex towards Bellegarde.

2.2 Neutrino beam

The CERN West Area Neutrino Facility (WANF) [74, 75] of the CERN SPS provides a beam of ν_μ with energies mostly above the threshold for charged current ν_τ interactions. Protons are accelerated in the SPS to an energy of 450 GeV with a repetition cycle of 14.4 s. They are extracted in two 6 ms long spills (called Fast Slow 1 and 2), separated in time by 2.7 s and focused onto a beryllium target. This target can sustain high proton intensities (up to 1.8×10^{13} for each of the 2 spills), and the interacting protons produce mainly pions (90%) and kaons (9%). The neutrinos originate from direct and indirect decays in flight of these parent mesons, in an about 290 m long vacuum tunnel. The important decay modes for muon neutrino generation are $\pi^+ \to \mu^+ + \nu_\mu$, $K^+ \to \mu^+ + \nu_\mu$, $K^+ \to \pi^0 + \pi^+$, with $\pi^+ \to \mu^+ + \nu_\mu$. Most of the neutrinos are from the first two decay modes. For the generation of $\overline{\nu}_\mu$ the reactions are similar, the parents being negatively charged. However the abundance of the

Table 2.1: The CERN SPS Wide Band Neutrino beam compositions at the location of the CHORUS emulsion target (transverse dimensions 1.44×1.44 m^2), as derived from the neutrino beam simulations.

neutrino type	flux (ν per proton on target)	average energy (GeV)
ν_μ	$5.56 \cdot 10^{-3}$	26.6
$\overline{\nu}_\mu$	$2.97 \cdot 10^{-4}$	23.7
ν_e	$4.7 \cdot 10^{-5}$	39.6
$\overline{\nu}_e$	$1.0 \cdot 10^{-5}$	35.6

latter—and consequently of the $\overline{\nu}_\mu$—is smaller by a factor 19 (see Table 2.1). Electron neutrinos are also generated, but in even much smaller quantities, via $K^+ \rightarrow \pi^0 + e^+ + \nu_e$, $\mu^+ \rightarrow e^+ + \nu_e + \overline{\nu}_\mu$, $K_L^0 \rightarrow \pi^+ + e^- + \overline{\nu}_e$, and $K_L^0 \rightarrow \pi^- + e^+ + \nu_e$.
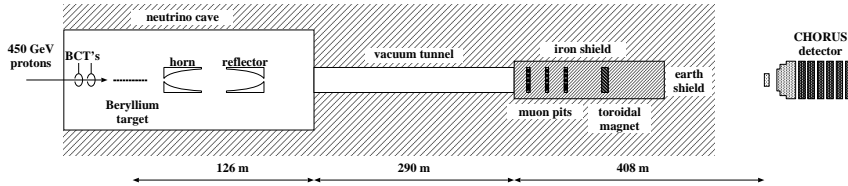

Figure 2.3: Schematic overview of the CERN West Area Neutrino Facility (not to scale).

The WANF layout is shown in Figure 2.3. Two beam-current transformers (BCTs) measure the number of incident protons. Positive (negative) mesons are focused (defocused) by the horn and the reflector, originally conceived by van der Meer [76]. After the vacuum tunnel iron and earth shielding prevents the remaining mesons, and any unwelcome decay products (like muons) to enter the CHORUS detector. The neutrino beam is indirectly monitored by the Neutrino Flux Monitoring system (NFM) [74] on the basis of the flux distributions of muons in three muon pits in the iron shield.
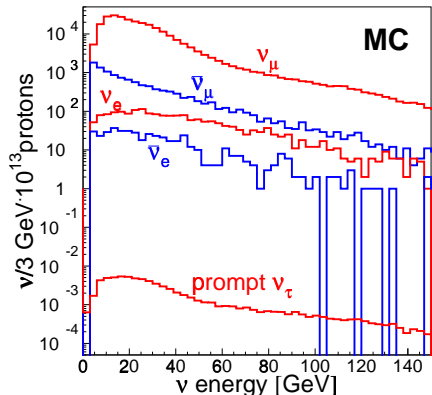
Figure 2.4: Energy spectra of the different neutrino components in the CERN SPS Wide Band Neutrino Beam at the location of the CHORUS emulsion target (transverse dimensions 1.44×1.44 m^2), as derived from the neutrino beam simulations.

Table 2.1 summarises the predicted abundance and mean energies of all neutrino species present in the WBB as obtained by using a full Monte Carlo simulation [77–79]. Figure 2.4 shows the predicted energy spectra of the different components of the neutrino beam crossing the CHORUS emulsions (1.44×1.44 m^2 area).

2.3   Emulsion target

The emulsion setup consists of two components: a) the emulsion target, where the neutrino interactions of interest for the oscillation search occur; and b) the emulsion sheets, which are used as a high accuracy tracking interface between fibre trackers and target.

The target consists of four parts called stacks. Each stack consists of 36 emulsion sheets, each consisting of a 90 μm thick tri-acetate cellulose foil coated on both sides with a 350 μm emulsion layer. Downstream of each emulsion stack are three interface emulsion sheets (see Figure 2.1), each consisting of an acrylic plate 800 μm thick coated on both sides with with a 100 μm thick emulsion layer. A "special sheet" (SS) is located at the downstream side of each emulsion stack. Two "changeable sheets" (CS) are positioned downstream of the emulsion target. To provide favourable background conditions for the recognition of the predicted tracks in the emulsion the changeable sheets are replaced after one to three months exposure to the neutrino beam.

Each set of emulsion stacks is exposed to the beam for two years of data taking. The total exposure time in the beam is about 10 months. To reduce emulsion fading (the erasing of the image due to diffusion), the emulsion stacks

are kept at a temperature of $(5.0 \pm 0.5)^\circ$C in a coolbox (see Figure 2.2). More information on the emulsion target can be found in [1].

2.4 Hexagonal spectrometer

A magnetic spectrometer of hexagonal shape is located between the target region and the calorimeter for the measurement of the curvature and consequently the charge and momentum of particles before they enter the calorimeter. It consists of an aircore magnet with a toroidal field and fibre tracker planes (see Section 2.5).

The hexagonal aircore magnet is made of six equilateral triangles with 1.5 m sides, 0.75 m in depth, and housed in a cylinder with 3.6 m diameter. Windings of thin aluminium sheets cover all faces of the triangles, producing in each triangle section a homogeneous field parallel to the outer side. The field strength has no radial dependence.

The magnet current is pulsed with a duty factor of $\sim 4 \times 10^{-3}$, to follow the time structure of the neutrino beam. A field of 0.12 T is obtained. More details on the magnet design, construction and operation can be found in [1, 80].

The momentum measurement is also used to measure the momentum of low energy (1-2 GeV/c) muons which do not reach the muon spectrometer. The spectrometer is installed as an integral part of the target region in the coolbox.

2.5 Fibre trackers

To provide tracking downstream of the emulsion target scintillating fibres are adopted because of their good spatial resolution and resolving power of neighbouring tracks. The fibre tracker system [1, 81–83] contains more than one million plastic scintillating fibres of 500 μm in diameter each and is also located in the coolbox. It consists of two main components:

1. **Target tracker (TT)**
   The target region consists of four emulsion stacks and eight target tracker modules. Each tracker module consists of four projection planes (Y, Z, and each rotated by 8°). A major role of the target tracker is to locate the stack where the neutrino interaction takes place, and to make accurate track predictions at the interface emulsion sheets. Both types of information are essential for track scanning, vertex finding and backtracking into the emulsion target.

43

2. **"Diamond-shaped" magnet tracker (DT)**

There are three magnet tracker modules, one upstream and two downstream of the aircore toroidal magnet. Each hexagonal tracker module consists of two planes. Each plane contains three adjacent parts called "paddles" giving measurements of three coordinates at 120° with respect to each other. The second plane is rotated by 60° with respect to the first, providing measurements of the complementary coordinates. Both the aircore magnet and the magnet tracker have the same sixfold symmetry such that one of the two coordinates measured by each module is in the bending plane.

Fibre ribbons with 7 layers in a "staggered" geometry are used to build the projection planes of the target trackers and the paddles of the diamond-shaped magnet tracker. At the readout ends, the fibre ribbons are bundled together and coupled to a total of 58 optoelectronic readout chains, each of them consisting of four image intensifiers and a CCD camera in series. The CCD camera contains an image zone and a memory zone, which enables the system to record two events in one neutrino spill.

For both fibre trackers (TT and DT) the achieved hit residuals (deviation of hits from the best fitted trajectory) for beam muons is $\sigma \sim 330~\mu$m, while the "track-element" (the centre of gravity of all hits in one ribbon) residual is $\sigma \sim 185~\mu$m. The two-track resolution is $\sigma \sim 380~\mu$m, thus two parallel tracks can be separated when they are about 1 mm apart. The prediction accuracies in position (deviation of the target tracker predictions on the emulsion sheets from the found tracks) and angle are $\sigma \sim 150~\mu$m and ~ 2.5 mrad, respectively. Folding in the expected intrinsic resolution for the emulsion sheets, the angular resolution of the fibre tracker is $\sigma \sim 2$ mrad. The momentum resolution $\Delta p/p$ of the hexagonal spectrometer results from the quadratic combination of two terms: a constant term of 22%, from the multiple scattering in the traversed material and a term proportional to the momentum which reflects the measurement accuracy $(\Delta p/p)_{meas} = 3.5\% \times p$ GeV/c.

2.6 Calorimeter

For the work described in this thesis, the calorimeter plays the central role. It is used as the target and measures the energy of the shower as well. Therefore it is described here in considerable detail.

The hadron shower from a neutrino interaction needs to be measured with good angular and energy resolution by a calorimeter. A good angular resolution is needed for events occurring in the emulsion, and a good energy resolution is needed for calorimeter events as well. In order to detect the decay to muons of a) short living particles produced in the emulsion target (in particular τ), and b) to be able to find a vertex for the events originating in the calorimeter, it is necessary to track muons through the calorimeter efficiently, and to match their trajectories with those determined by the other detectors.

The calorimeter was designed to fulfill these requirements. It is the first large scale application of the "spaghetti" technique of embedding scintillating fibres into a lead matrix [84, 85]. Scintillating fibres of 1 mm diameter and lead as passive material were chosen, with a lead to scintillator volume ratio of 4:1. This choice increases both compensation—the response of the electromagnetic and non-electromagnetic components of hadronic showers being the same, the $e/h = 1$ condition—and the quality of sampling. Consequently it optimises hadronic energy resolution [84, 86]. The fibres are placed in directions approximately perpendicular to the beamline, to allow angular measurements of the showers, as well as tracking of muons. The most downstream part of the calorimeter is not of spaghetti type but a lead-scintillator-strip sandwich with the same 4:1 ratio as the upstream parts.

The calorimeter has a modular construction, in which the elements are arranged to form planes perpendicularly to the beam, alternating in the horizontal (H) and vertical (V) direction. To reconstruct with good accuracy the centre of gravity of the energy deposited by the hadrons produced, the width of the modules is chosen much smaller than the size of the average hadron shower. Longitudinally, the calorimeter consists of three sectors with decreasing granularity. In the downstream direction these are called EM, HAD1 and HAD2. The EM sector has been designed to measure the electromagnetic component of the hadronic shower in neutrino induced emulsion target events, while the other two sectors complete the measurement of the hadronic component apart from some leakage at the back into the muon spectrometer (see Section 2.8.2). The total depth corresponds to 144 radiation lengths and 5.2 hadronic interaction lengths. Between subsequent "H" and "V" planes, streamer tube chambers have been inserted to allow tracking of any passing charged particles. The streamer tube chambers, which are also used in the muon spectrometer, are described in Section 2.7.3.

The calorimeter is shown in Figure 2.5 and its features are described in Table 2.2. A detailed description of the construction and tests of the three sectors can be found in [87].

Table 2.2: Calorimeter features.

	EM	HAD1	HAD2	Total
Radiation length: X_0	21.5	55.2	67.1	143.8
Interaction length: λ_{int}	0.78	2.0	2.44	5.22
Number of planes	4	5	5	14
Read-out cells (ROC) per plane	62	40	36	628
ROC dimensions (cm^3)	$4\times4\times262$	$8\times8\times335$	$10\times10\times369$	—
Density per plane (g/cm^2)	37.33	76.09	92.23	990.92

2.6.1 Electromagnetic sector

The electromagnetic (EM) sector contains 4 planes (two H and two V planes), each of 31 modules. Individual modules consist of extruded layers of grooved lead and plastic scintillating fibres positioned in the grooves. The groove diameter is 1.1 mm, the groove separation is 2.2 mm and the layer thickness 1.9 mm. The material, the same as for the HAD1 and HAD2 modules, is lead and 1% admixture of antimony, to improve the mechanical properties. A module consists of a pile of 21 layers, 2620 mm long and 82.4 mm wide, and 740 fibres of 3050 mm length. On either side of the module, fibres are assembled in two hexagonal bundles, defining two different readout cells (ROC) with about 40×40 mm^2 cross-section. Each module, the same as for the HAD1 and HAD2 modules, is packed into a stainless steel box open at both ends. Each of the fibre bundles is coupled to a 1" photomultiplier (PM), type Hamamatsu R1355/SM, by a plexiglas light guide.

2.6.2 Hadronic sector

The hadronic sector consists of two sectors HAD1 and HAD2. The HAD1 sector consists of 5 planes (three H and two V planes). A plane is formed by 40 modules, each made of 43 extruded layers of lead identical in width and groove size to those used for the EM sector, but with a length of 3350 mm. The scintillating fibres have 3810 mm length, for a total of 1554 fibres per module. Fibres are collected at both ends in a hexagonal bundle coupled by a light guide to a 2" PM, type Thorn-EMI 9839A.

The HAD2 sector consists of 5 planes (two H and three V planes) with 18 modules each, making a total of 90 modules. Each module has five alternate
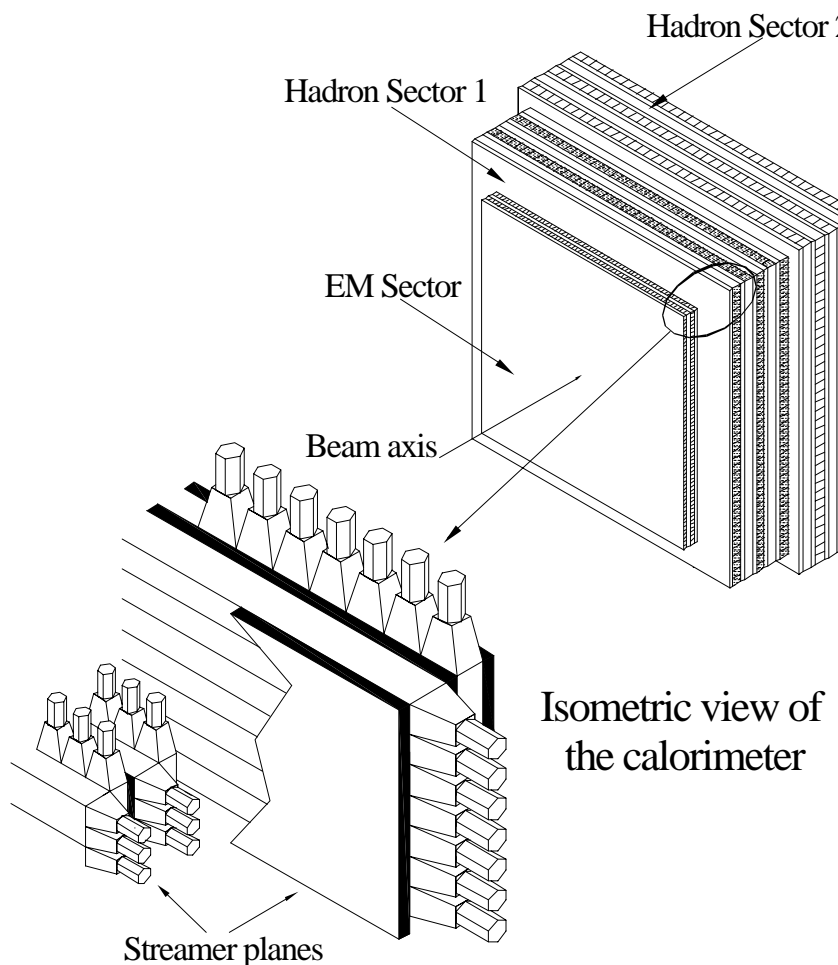
Figure 2.5: Schematic view of the calorimeter.

layers of lead bar ($3690 \times 200 \times 16$ mm^3) interleaved with two adjacent scintillator strips ($3714 \times 100 \times 4$ mm^3 each). Each of the two groups of five scintillators is coupled to 2" PMs at both ends via plexiglas light guides; therefore, a single module is viewed in total by four PM tubes, and contains two ROCs.

The analog signals of the 1256 PMs of the calorimeter are digitised by dualrange 8-bit Analog to Digital Converters (ADCs). The nominal ratio of the conversion factors for the two ADCs (high/low sensitivity) is set to 20 for all the channels: the actual value of this ratio for each ADC is determined and monitored experimentally by using neutrino events. The ADC integration gate is 220 ns wide.

2.6.3 Performance

The intrinsic performance of the calorimeter has been determined in several measurements [87,88] with test beams of well defined energy, for single modules and the completely assembled calorimeter. In the latter case, the calorimeter, mounted on rails, was shifted sideways with respect to its normal location in the CHORUS detector, to be placed on the axis of the SPS X7 test beam [89].
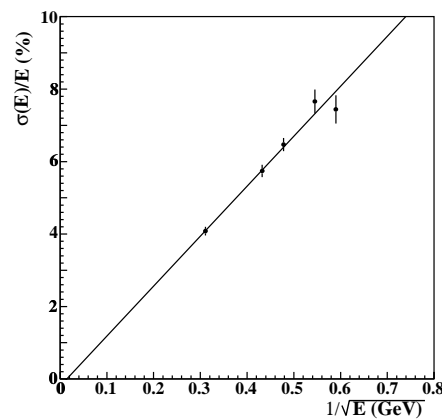

Figure 2.6: The energy resolution for electrons of the calorimeter. The solid line indicates the fitted resolution curve.
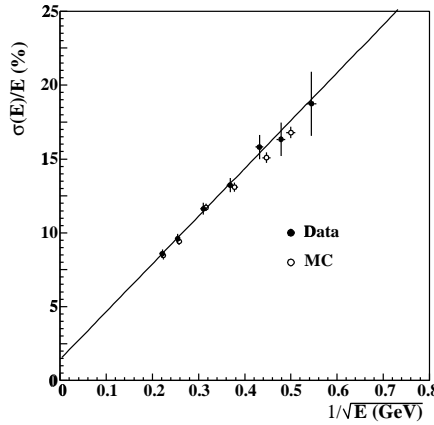
Figure 2.7: The pion energy resolution of the calorimeter. The open circles show the Monte Carlo prediction, the closed ones the data. The solid line indicates the fitted resolution curve to the data.

The electron response has been studied [88] for different beam momenta in the range from 2.5 to 10 GeV/c. The response of each module is obtained by computing the geometric mean of the two photomultiplier signals (see Section 2.8.1). For each momentum, a Gaussian fit was performed to the distribution of the calorimeter signal, the sum of the calibrated responses of all modules. The intrinsic energy resolution $\sigma(E)/E$, is plotted in Figure 2.6 as a function of the electron energy. The energy dependence is well fitted by the function

$$\left(\frac{\sigma(E)}{E}\right)_{e^-} = \frac{(13.8 \pm 0.9)\%}{\sqrt{E\,(\text{GeV})}} + (-0.2 \pm 0.4)\%. \tag{2.1}$$

This result agrees with Monte Carlo predictions. By studying electron showers developing in different calorimeter zones, the non-uniformity in the electromagnetic response was estimated to be of the order of 5%. This non-uniformity is mostly due to a reduction of the signal response near the EM module edge, where no active material is present.

The response to pions was studied in the range from 3 to 20 GeV/c. The measured pion momentum dependence is found to be linear up to the highest energy within less than 2%. From a Gaussian fit to the response distributions one determines the intrinsic energy resolution $\sigma(E)/E$, which is plotted in Figure 2.7 as a function of the pion energy. The errors assigned to each point include a systematic uncertainty of about 2%, evaluated by applying different event selection criteria to the data, and by studying pions hitting different calorimeter positions. This uncertainty is smaller than the one for the electron case. The main reason is the larger number of calorimeter modules involved in a hadron shower. The energy dependence of the hadronic resolution is parametrised as

$$\left(\frac{\sigma(E)}{E}\right)_{\pi^-} = \frac{(32.3 \pm 2.4)\%}{\sqrt{E\,(\text{GeV})}} + (1.4 \pm 0.7)\%. \tag{2.2}$$

The predictions of a Monte Carlo simulation, also shown in Figure 2.7, are consistent with the data.

The shower direction can be determined event by event from the knowledge of the centre of gravity coordinates in the different planes. The angular resolution at 10 GeV/c for the two projections is about 60 mrad (HWHM). From

the electron and pion response of the calorimeter the experimental e/π ratio is determined and ranges from about 1.23 at 3 GeV/c to about 1.12 at 10 GeV/c. Further details on the performance of the calorimeter may be found in [88].

2.7   Muon spectrometer
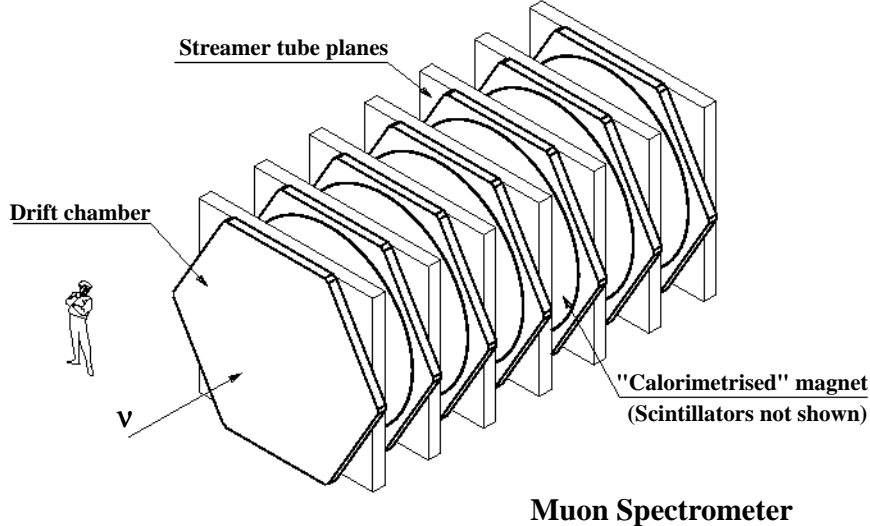
Figure 2.8: Muon spectrometer global overview.

The role of the muon spectrometer in the CHORUS detector is to identify muons and determine their trajectory, momentum and charge. The spectrometer is located downstream of the calorimeter whose 5.2 hadronic interaction lengths filter out nearly all the particles produced by neutrino interactions in the emulsion target except muons with momentum larger than 1.5 GeV/c. As displayed in Figure 2.8, the spectrometer is constructed from six toroidally magnetised iron modules and tracking detector planes consisting of drift chambers and limited streamer tubes (more details on each part are shown in Figure 2.9). In addition, scintillator planes interleaved with the magnet iron provide at the entrance of the spectrometer a measurement of the leakage of hadronic showers from the back of the calorimeter into the muon spectrometer. The fast signals from these scintillator planes are also used for triggering.

Scintillators

8 Streamer tube planes

PM

Drift chamber

20 Iron disks

Magnet excitation coil
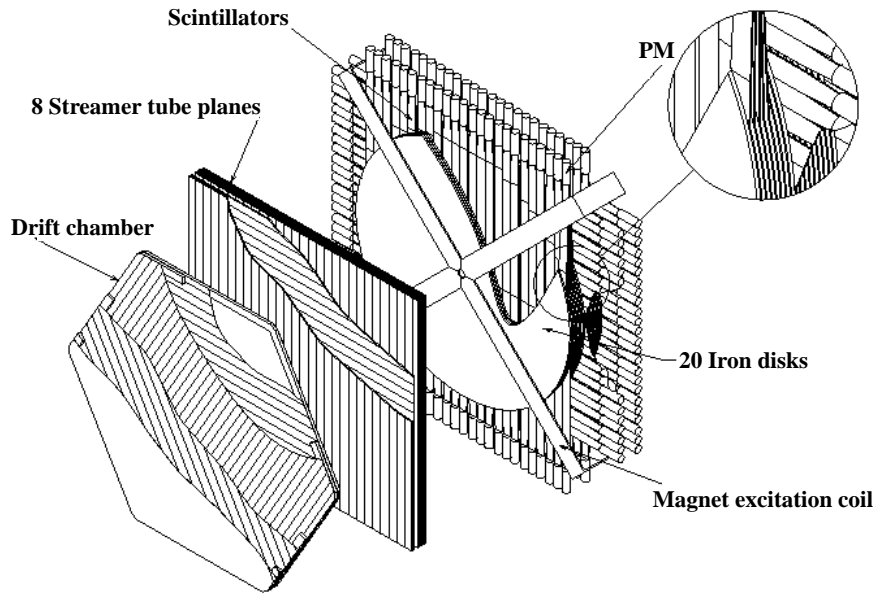
Drift chamber, streamer tube pack and magnet module

Figure 2.9: Muon spectrometer details of a driftchamber, a streamer tube pack and a magnet module.

The momentum resolution of the muon spectrometer system is evaluated from data obtained with a test beam of negative muons (see Section 2.8.2). The reconstructed $(1/p)$-distribution gives a resolution of about 19% at 71 GeV/c. A Monte Carlo simulation is used to determine the muon momentum resolution at lower momenta and the results are shown in Figure 2.10. The momentum scale is cross checked for low momentum muons by determining their stopping range [90] inside the spectrometer and deriving their momentum from the range-energy relation [91].

2.7.1   Magnets

The momentum of a muon traversing the spectrometer is determined from the change of its trajectory along the six toroidal magnets, originally used as calorimeter modules in the upgraded CDHS detector [92, 93] and, later, in the

CHARM II spectrometer [94–96]. Each magnet is constructed from twenty 25 mm thick iron disks with an outer diameter of 3.75 m, interleaved with 5 mm thick scintillator planes inserted into 6 mm gaps between the disks. The entire assembly, housed in a protective aluminium box, has a total thickness of 660 mm. Each magnet weighs about 43 tons.

The iron is magnetised by four water cooled copper coils passing through a 85 mm wide hole in the centre of each magnet. The field inside the iron [92, 93] is nearly symmetric in azimuthal angle and varies by 25% along the radius, providing a field integral of approximately 0.85 Tm per magnet. To maximise the acceptance for τ^- decays and ν_μ interactions in the calorimeter, the polarity of the current of 700 A is set such that negatively charged muons are focused, that is, bent towards the centre of the magnets. The magnets are separated by 1208 mm along the beam and placed vertically. The centres of the magnets are positioned such as to follow the 42 mrad slope of the beamline.

2.7.2 Drift chambers

The seven drift chambers [97, 98] are part of the original detector used by the CDHS experiment, and provide tracking in the muon spectrometer system. They are mounted in each of the seven tracking gaps on both sides of the six magnets, and centred along the neutrino beam axis. Each chamber consists of three hexagonal drift planes oriented at 60° with respect to each other, the wires of the rear plane being oriented horizontally. Each plane has 62 parallel sense wires (40 μm diameter, 3.75 m long) separated by 60 mm and interleaved with cathode wires.

The chambers are filled with a 60% argon - 40% ethane mixture. The anode sense wires and the cathode wires are held at a potential of 3700 V and -1000 V, respectively. An approximately uniform electric field along the 30 mm drift path is obtained by another row of field correction wires. The drift velocity is typically 53 μm/ns. Signals are amplified by chamber mounted pre-amplifiers and then readout by TDCs with 10 ns resolution operating in "common stop" mode. These TDCs can record up to 4 hits per event, sufficient to handle neutrino data since typically only one track (the muon) is recorded in the spectrometer. The signals are distributed in such a way that any four consecutive wires are readout by different TDC units.

The hit resolution of the drift chambers is about 1 mm and the efficiency better than 99% per plane. With each chamber, right-left ambiguities can be resolved for 83% of forward going tracks.

2.7.3   Streamer tube chambers

Each of the seven drift chambers is followed by a stack of eight limited streamer tube planes of the former CHARM II calorimeter [94–96], slightly modified to reduce cross talk. They provide measurements of track segments in each gap and eliminate unresolvable right-left ambiguities in the corresponding drift chamber.

Each plane, covering an active area of 3.67×3.67 m^2, consists of 352 square-shaped limited streamer tubes with the inner area of 9×9 mm^2 and an average wire spacing of 10.5 mm. The tubes are operated with a 27% argon - 73% isobutane mixture, plus a 0.4% admixture of water vapour to prevent organic deposits onto the wires. A positive high voltage of 4300 V is applied to a conductive graphite coating of the inner PVC tube walls. The anode wires are held at ground potential and coupled directly to the electronics.

External to the streamer tubes are 176 cathode pickup strips, 18 mm wide with 21 mm spacing, orthogonal to the wire direction. They measure the track position along the wire, identified as the centre of gravity of the induced charge distribution. Consecutive planes have alternating horizontal and vertical wire orientations, so that each stack of streamer tubes in a tracking gap provides up to eight independent coordinate measurements in each of the two views. On average, a forward going muon produces 3.6 wire hits and 3.2 usable strip hits per view in a gap.

The original CHARM II electronics have been upgraded to supplement the digital tube readout with drifttime measurement. The drift velocity is 54 μm/ns. The maximum drifttime is 90 ns for normal incidence tracks.

The signals from each group of 8 consecutive wires are combined to form 44 drifttime cells per plane. Since the occupancy of the muon spectrometer is low, the digital hit pattern can be used to uniquely identify the wire in a cell. There are fewer than 0.1% broken wire channels and the hit efficiency per plane for beam muons is (90 ± 2)%, consistent with the geometrical acceptance.

Signals from four consecutive cells are multiplexed to a single input of a 10 ns TDC of the same type as used for the drift chambers. The multiplexing is achieved by delaying the four signals by about 300 ns with respect to each other, therefore allowing the cell number to be uniquely defined by the signal timing. The delays are measured regularly during data taking and a final hit resolution of about 800 μm is achieved. A logical OR of all wires in the plane is readout by a 1 ns TDC. This precise measurement is useful for cross calibration of the 10 ns TDCs, and supersedes low resolution measurements in the case of a single track.

All cathode strips have individual analog readout channels, with the charge digitised by dual range flash ADCs. Clusters with two and more neighbouring cathode strips having signals above the threshold are used for subsequent analysis. The resulting effective hit efficiency for the strip readout is $(80 \pm 2)\%$. The induced charge distribution is virtually independent of the cluster width, with 95% of the charge contained in three central strips. Therefore, the cluster centre of gravity is calculated using only the maximum charge strip and its two neighbouring strips. The relatively high noise rate limits the hit resolution to 2.4 mm (RMS) per plane for the streamer chambers strip readout. However, this is sufficient to provide a constraint on the right-left ambiguity in the streamer tube drift distance measurement, as well as a measurement in the case of wire readout inefficiencies or failures.

Streamer chambers are also used in the other parts of the experiment for tracking purposes. There are 4 planes in front of the veto scintillators, 6 planes (only 4 planes in the 1994 run), called the "Tracker Streamer Tubes" (TST), between the trigger plane H and the calorimeter, and 22 planes interleaved between the calorimeter segments. Originally, all these planes had only digital readout. In 1995 the TST planes were upgraded by adding a drifttime readout with 1 ns TDCs. The TST planes were replaced by a honeycomb tracker in August 1996.

The methods of track finding and track fitting for the muon spectrometer are described in [99, 100].

2.7.4   Scintillators

The scintillators embedded in the magnets are used primarily for triggering and the scintillators in the first two magnets for measuring the longitudinal energy leakage from the calorimeter. In addition, a precise range measurement and thus a momentum determination of muons with a momentum of less than 5 GeV/c at the entrance to the spectrometer is possible using the sampling of the iron by the scintillator planes (Figure 2.10).

Each scintillator layer in a magnet consists of 24 strips of 150 mm width, each strip consisting of two independent halves separated by a mirror. Five consecutive layers have the same horizontal or vertical strip orientation and form a readout plane, with every five consecutive halfstrips in the beam direction forming "halfcounters" viewed by a single PM [92, 93]. Thus, each magnet has four readout planes, two with vertical and two with horizontal "counters". After summing the uncalibrated signals from opposite halfcounters, the sum

signal is split with a passive divider and 90% is digitised and 10% is used for triggering. The digitisation is performed using ADCs with an integration gate of 170 ns width.

The original CDHS trigger electronics have been upgraded to provide a wider set of primary trigger signals, which are used in the central trigger decision logic (Section 2.9) as well as in standalone subsystem triggers. The efficiencies of the trigger logic are close to 100%.

The calorimetric capability of the spectrometer scintillators is limited by their transparency, strongly degraded since they were built 15 years ago. The signal of a minimum ionising particle varies by factor of about 5 along the 1.80 m long central halfcounter. However, for the main emulsion triggers (Section 2.9), with the longitudinal leakage from the calorimeter not exceeding 2%, a superior shower energy resolution in the muon spectrometer is not required. For events induced in the calorimeter, a significant improvement in total shower energy reconstruction can be obtained by summing the calorimeter and the muon spectrometer energy deposition measurements (Section 2.8.2).

2.8 Calibration

During the 12 s SPS interburst intervals, data are taken for the different sub-detector systems to calibrate and monitor their responses. Cosmic ray events are taken to calibrate different elements of the detectors and to monitor time variations of the response. In addition, the calorimeter and the spectrometer need an "absolute" calibration in energy or momentum. Therefore, test beams of electrons, muons and pions have been used to determine their absolute energy and momentum scale. Data from high momentum punch through muons associated with the neutrino beam has been taken once per month, the aircore magnet pulsing being switched off, to monitor the relative alignment of the various detectors.

Below we summarise the main calibration procedures for the calorimeter and the spectrometer. These are actually implemented in the standard offline analysis.

2.8.1 Calorimeter

Three steps are needed for the determination of the calorimeter response:

- *Equalisation* of the signals from each individual photomultiplier (PM) within each sector (EM, HAD1 and HAD2), performed by measurements

with penetrating cosmic rays. An equalisation constant is computed for each PM by selecting cosmic muons crossing the central region of the modules ($\pm$ 100 mm), and correcting for the effective track length. The statistical error for this procedure is at a 5% level, while the systematic effects due to the time dependence of the PM gain and to the position dependence of the energy response are less than 3%. Cosmic ray events are also used to create a data base of the malfunctioning PMs (inactive or noisy) during the running periods, and for the online monitoring of the calorimeter.

- *Intercalibration* among different sectors: to combine the signals of the three different sectors, two intercalibration constants are needed, namely those of HAD1 and HAD2 relative to EM. These constants are determined experimentally using pions of known momentum interacting at different calorimeter depths, and studying the sharing of the shower energy between different sectors [88].

- *Overall energy calibration*: the calorimeter response to the incoming particles is determined by adding the energy deposited in all the modules, once the equalisation and intercalibration procedures previously described are performed. Since each module is equipped with one PM on each end, there are different possible definitions of the energy deposition, according to the ways the two PM signals (L and R) are combined. The geometric mean $S_g = \sqrt{S_L \times S_R}$ is chosen since its response (hence the energy derived) is independent of the hit position along the length of the module. For the channels which are noisy or inactive during the data taking, the signal from the other PM on the same cell is used, after correcting for the light attenuation based on the hit position.

The measured shape of the calorimeter signal distribution for pions is well fitted to a Gaussian. The calibration and intercalibration procedure do not introduce any appreciable bias in the determination of the overall calorimeter response. The results on resolution and energy dependence of the calorimeter response, already been presented in Section 2.6, serve as a reference for the here summarised calibration procedure, applied to each actual data set.

2.8.2   Muon spectrometer

Negatively charged muons of 75 GeV/c momentum from the SPS West Area are used for calibrating the momentum measurement of the muon spectrometer.
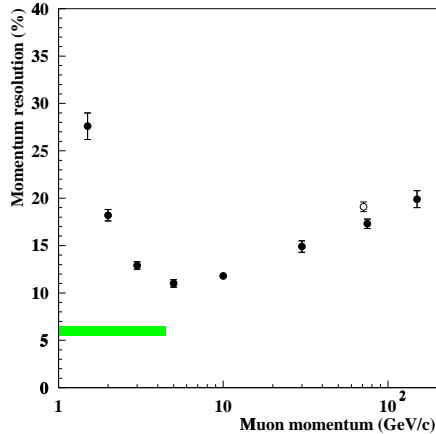
Figure 2.10: The muon spectrometer momentum resolution as a function of the incident momentum. The full dots denote Monte Carlo events, and the open dot at 71 GeV/c test beam muons. The shaded band corresponds to muons stopping in the spectrometer, with their momentum determined by range.

Due to ionisation losses in the detectors and beam elements upstream, the beam momentum is (71 ± 2.5) GeV/c at the entrance to the spectrometer. The derived momentum resolution [1] is shown in Figure 2.10.

Similar to the calorimeter calibration, cosmic muons recorded in the interburst period (the about 12 s between Fast Slow 2 and Fast Slow 1, see Section 2.2) are used for the scintillation counter equalisation and for the determination of the light attenuation curves. The correction for the light attenuation is needed because, unlike in the calorimeter, the counters are equipped with a PM on one end only, and with a mirror installed on the other end. Cosmic rays are also used for the online monitoring of the efficiencies of all the spectrometer elements.

The first two spectrometer magnets also serve as calorimetric shower leakage detector. The energy calibration is performed together with the calorimeter calibration in pion beams at different energies. The method is similar to intercalibration of the calorimeter sectors. The pions interact at different calorimeter depths, and the shower energy leakage into the spectrometer is determined as a difference between the nominal beam energy and the energy deposited in the calorimeter. The leakage is plotted in Figure 2.11a as function of the corresponding spectrometer response. The calibration curve obtained this way is used for shower leakage correction, as demonstrated by Figure 2.11b.

The internal alignment of the spectrometer components (drift chamber planes, streamer tubes, cathode strips and the scintillators) is done with 100 GeV/c testbeam muons recorded with the magnetic field turned off. The global alignment relative to the rest of the CHORUS detector is done by reconstructing
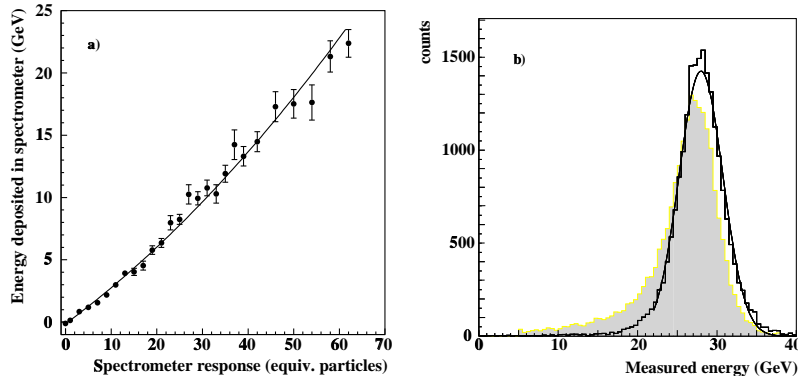
Figure 2.11: Spectrometer as calorimeter shower leakage detector: a) Spectrometer scintillator calibration with 7 to 28 GeV/c test beam pions. The shower energy leaking from the calorimeter into the spectrometer is shown as function of the measured spectrometer response (in equivalent particles). b) Reconstructed energy distributions for 28 GeV/c test beam pions. Shaded histogram: the calorimeter measurement alone (25.5 ± 5.3 GeV), solid histogram: the sum of the calorimeter and the muon spectrometer measurements (27.9 ± 3.2 GeV).

high momentum (neutrino beam related) muons traversing the entire detector. The corresponding "alignment" events are also used for precise "time-zero" calibrations needed for drifttime measurements.

A detailed description of the calibration of the muon spectrometer system can be found in [99].

2.9   Trigger system

The trigger system has been designed to select neutrino events induced in a) the emulsion target and b) the calorimeter and muon spectrometer. The other important task is the synchronisation of the data taking with the time structure of the neutrino beam. Central in the present work is the circumstance that the calorimeter acts as a neutrino target. Therefore, the calorimeter triggers are the most important here. In the calorimeter typically one hundred interactions per neutrino spill occur. To keep dead time low only about five of these are

selected by the trigger system to be read-out and recorded on tape.

The emulsion trigger accepts events originating in the emulsion target and rejects background from cosmic rays, muons from the beam, and neutrino interactions outside the emulsion target. Additionally, trigger modes for neutrino induced events in the calorimeter or spectrometer are provided for physics as well as for calibration and alignment purposes. Apart from the signals from the five trigger planes (see below), the trigger system uses signals from the calorimeter and spectrometer scintillators. The main input of the trigger system comes from five scintillator trigger planes, in the downstream direction denoted as: anti (A), veto (V), emulsion (E), timing (T) and hodoscope (H) planes, with their positions indicated in Figure 2.2.

The planes consist of two layers of scintillator strip counters each positioned just behind each other in the beam direction. The two layers are staggered by one half width, such that the geometrical efficiency of the planes is 100%. The layers consist of strips, with their thickness minimised to reduce loss of tracking precision due to multiple scattering. In Table 2.3 the number and dimensions of the strips in each plane are summarised. They are:

- The A plane (vertical strips) is located just downstream below the floor in front of the detector. It is used to veto events due to interactions in the ground upstream of the detector.

- The V plane is located in the beamline upstream of the emulsion target. In addition to the 20 vertical strips, there are three horizontal strips, one covering the top part of the calorimeter, two on the bottom.

- The E plane (strips vertically) is located downstream of the emulsion target between the two last fibre tracker biplanes. The E plane serves to reject neutrino interactions occurring in the iron support structure of the target region and in the image intensifier chains used to readout the fibre trackers.

- The T and the H plane (strips horizontally) are located behind the last fibre tracker plane and in front of the calorimeter respectively.

An emulsion event trigger corresponding to a neutrino interaction in the target region is defined by a combination of hits from the strips in planes E, T and H consistent with a track with $|\tan(\theta)| < 0.20$ with respect to the neutrino beam axis. This requirement mainly rejects cosmic rays and events originating in or below the floor. A veto is formed by any combination of

Table 2.3: Segmentation characteristics of trigger hodoscopes.

Plane	A	V	E	T	H
Number of strips/layer	16	20	7	15	20
Strip width (cm)	20	20	20	10	10
Strip length (cm)	200	320	148	160	200
Orientation	vert	vert	vert	hor	hor
Area covered (cm^2)	200×320	400×320	150×148	160×160	200×200

hits in the hodoscopes V or A. A precise timing between the T and V plane (2 ns at FWHM) is needed to avoid vetoes due to backward going particles in good emulsion events. The timing precision is achieved by coupling the T and V scintillator strips on both sides to a photomultiplier (PM), and deriving a position independent mean time signal.

The size of the V plane has been chosen to fully cover the area defined by the angular acceptance of the E, T and H planes, as well as the calorimeter and muon spectrometer.

The trigger decision is made in four steps: 1) the formation of a strobe signal to start the pre-trigger, which makes a fast decision by checking a minimum set of conditions. The rate is about 300 strobes per 10^{13} protons on target. 2) the second level trigger and 3) main trigger decision both based on pattern information. A complex chain of VME (VersaModule Eurocard) Programmable Logic Units processes the various input signals. Patterns are built based on detector signals still allowing to count planes, to check vetoes and to apply fiducial volumes. 4) Final trigger pattern formation. The second level and main trigger decision patterns are sent to a VME Logic Matrix Unit. Coupled with the other predefined parameters like scaledown factors, this information is translated into a 16-bit trigger output pattern. Each bit corresponds to a different readout pattern, allowing for a different set of subdetectors to be read out for different triggers.

Some triggers have to be scaled down in rate. This is done by a specific enable signal generated at a reduced rate according to the desired down-scale factor.

Timing of signals important for the trigger are also monitored during data taking. In Figure 2.12 some timing histograms for the trigger system are given. The plots give information about the time structure of signals from the two
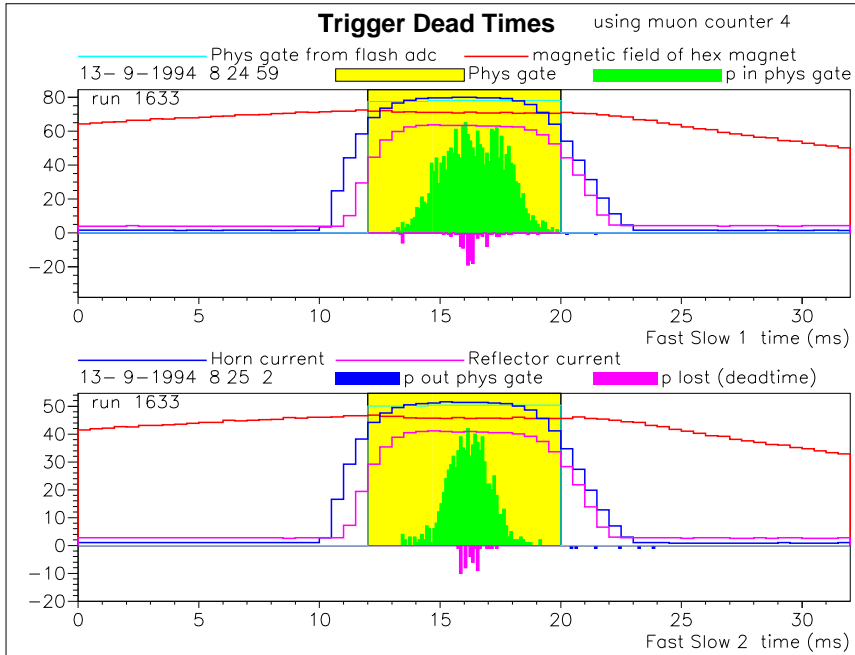
Figure 2.12: The trigger timing histograms as used online. The amount of protons corresponding to the deadtime is displayed as negative values. See text for details.

SPS Fast Slow (FS) beam extractions, the top plot for FS 1 and the lower one for FS 2 spill. Both histograms give similar information, containing the current of horn and reflector of the neutrino beam, the magnetic field of the CHORUS hexagonal magnet along with the physics gate (the timing acceptance for neutrino events), all in time slices of 0.5 ms. The information on the time structure of the neutrino spills and the time dependence of the read-out and decision deadtime is clocked by the muon rate of the neutrino beam (which is counted in slices of 100 μs), inside one of the muon pits in the iron shield. The beam muon rate is proportional to the neutrino flux.

Not only the time structure of the individual signals, but in particular their time correlation can be watched in the timing plots. The flat top of the horn and reflector current, the hexagonal magnetic field as well as the physics gate should be structured in time such as to fully cover the time distribution of the

2. CHORUS apparatus

protons on target.

The trigger system also selects events which originate in the calorimeter. For these "calo" events additional information is needed from the trigger planes A, V and H, as well as from the calorimeter and spectrometer scintillators. The A, V and H planes act as a veto for events generated upstream of the calorimeter. Beam related muons and interactions which occur in front of the calorimeter (e.g. in the target region) are rejected in this way. A fiducial volume trigger condition selects events occurring in the central part of the calorimeter, in order to optimise acceptance corrections and muon reconstruction efficiency.

The calorimeter two-track trigger is implemented to record events for the study of charm physics. It requires at least four planes of the hadronic part—HAD1 and HAD2—of the calorimeter and two out of the first four magnets of the muon spectrometer to show activity. The fiducial volume condition implies that the neutrino interaction takes place in the central region of the ten upstream planes of the calorimeter. In addition, a two-track signal has to be fulfilled either by at least three planes in the hadronic part of the calorimeter with exactly two hits or at least two muon spectrometer magnets with two or more hits.

The calorimeter charged-current trigger selects events for the study of neutrino-lead interactions, to derive the beam flux and to extract structure functions. The penetration condition requires a muon to penetrate at least two magnets of the muon spectrometer and to activate at least five planes in the hadronic part of the calorimeter. The fiducial volume condition implies that accepted neutrino interactions take place in the central region of the six upstream planes of the calorimeter.

The calorimeter quasi-elastic trigger provides events with little hadronic activity, useful for measuring the neutrino energy spectrum. The penetration condition requires activity in at least three of the six downstream planes of the calorimeter and at least two magnets of the muon spectrometer. The fiducial volume condition requires that the neutrino interaction takes place in the central part of the nine upstream planes of the calorimeter. Events with two or more hits in at least three calorimeter planes are vetoed.

Finally, for normalisation and efficiency monitoring purposes a calorimeter minimum bias trigger is implemented. The definition of this trigger has been changed over the life of the experiment. During the datataking period of our work it requires only activity in the last plane of the electromagnetic part of the calorimeter.

The calorimeter charged-current and minimum bias triggers are for our datataking downscaled by a factor of 6 and 40 respectively, in order to minimise deadtime for the oscillation search. More information on the trigger system in CHORUS is given in [101].

2.10   Data acquisition system

The CHORUS data acquisition (DAQ) software is implemented as much as possible on computers running a standard UNIX system. For the low-level real-time parts, however, the simpler and faster OS-9 real-time kernel is used.

The frontend of the DAQ system consists of 38 different CPUs, running OS-9 plus the REMote Operating System (REMOS) [102]. REMOS creates an object oriented multiprocessor environment for real time applications and offers procedures to read the digitised signals from the detector, to collect, validate, compress, and eventually send them to a storage device. It also includes procedures [103] to exchange messages among OS-9 processes and to sent messages to the UNIX side.

Each of the detector subsystems (trigger, opto-electronics, calorimeter and muon spectrometer) is equipped with a local DAQ system. All these subsystems are interconnected in a tree-like structure via the VME Inter Crate (VIC) bus, as well as through Ethernet. Data are collected at the root of the tree by the event builder.

The run-control process, operational on the event builder CPU, communicates with the *Run-Control* graphical user interface (GUI) process. The GUI resides on the UNIX cluster, that consists of five IBM RS-6000 PowerPC workstations and handles the interaction between the physicist on shift and the DAQ system. The full events collected by the event builder are sent as messages to a dispatcher process on a UNIX machine. The dispatcher [104] is a general-purpose message-based data distribution programme. These events are used for online monitoring, and histogramming.

A "slow-control" system [105] monitors low and high voltages of the detectors and their read-out hardware, temperatures, gas flows etc. An alarm is generated for any channel whose value is outside its allowed range.

Monitoring facilities for the neutrino beam performance are provided by display of various histograms like beam profiles and time structures collected using detectors at the SPS West Area Neutrino Facility (WANF). More information on the CHORUS data acquisition can be found in [1] and [106].

2.11 Online monitoring

A well designed online monitoring system is important in setting up and running an experiment. Its function is to enable performance evaluation for all detector elements, by building histograms on important detector aspects. The online monitoring system has been designed in a modular way such that the various tasks are performed by different processes, like those to fill histograms, to display them and to test detector elements either visually or automatically.

2.11.1 Histogramming

The CHORUS team developed its own histogramming package [107]. It is a library written in the object oriented language C++. The package contains six types of histograms: 1- and 2-dimensional, profile, integer 1- and 2-dimensional histograms as well as two-tuples. Profile histograms are histograms in which the bin contents are analysed for their mean and standard deviation, rather than simply summed. Two-tuples are a way of handling (x, dx, y, dy) information.

For all these histograms there are two types, "ordinary" and "volatile". The ordinary histograms are saved and reset at the beginning of a new run, and the volatile ones can be saved or reset during the run, but can also be used to accumulate data over more than one run. The histograms are written to disk so that the viewing and checking is independent of the data taking. This allows easy manipulation and comparison of histograms taken at different times, e.g. new with old or with a reference (for automatic checking).

Higher level histograms are made by the offline analysis process CHO-RAL [108] (e.g. efficiency histograms, where track finding is needed). This Fortran-programme uses the CERN HBOOK package [109]. To view these histograms with the online monitoring histogram viewer (HV) an interface [110] to convert these histograms to the CHORUS online histogram format has been made.

The histograms are saved at specific times. The *Run-Control* automatically sends every 15 minutes a message to the histogram processes to save the ordinary histograms. The ordinary histograms are saved when a run has finished, the volatile ones are only saved on explicit user request.

Another type "automatic" histograms are continually displayed without user request. Those are never written to disk. These are—at a specified time or event interval—automatically sent to processes to be displayed. An example of automatic histograms is given in Figure 2.13 where histograms of the hit
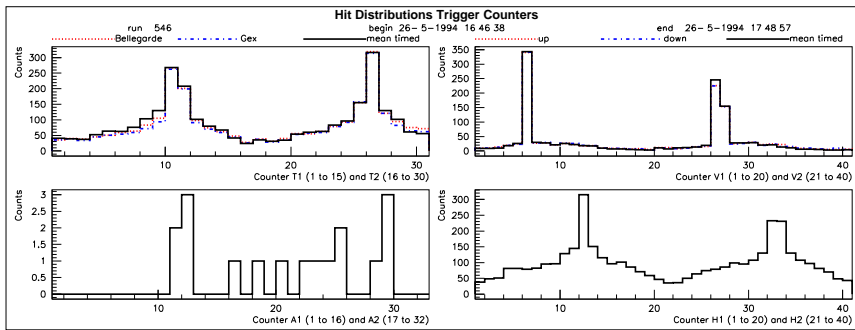
Figure 2.13: Trigger counter histograms as displayed online. See text for details.

distributions of the trigger planes T, V, A and H are shown. The high peaks in the hit distributions of the trigger planes T, V and H arise from a pion beam (in the 2.7 s interval between the two beam extractions Fast Slow 1 and 2), used in this case to check the intercalibration of the energy released in the fibre trackers and the calorimeter. Because the T and V strips are readout on two sides and their mean time is also formed, three histograms for these planes are displayed superimposed.

2.11.2 Histogram viewing

The online monitoring histogram viewer (HV) (see Figure 2.14) is the process to display histograms on user request. The Tcl/Tk [111] interpreter is used as the graphical user interface package. For displaying the histograms HBOOK [109], HIGZ and HPLOT [112] are applied. With HV the selected and displayed histograms can be printed, reset (only volatile ones) or saved. For the last two options a message is sent to the histogram processes.

The HV process needs input from the DAQ to find the directory and file name of any histogram to be presented. Therefore, the event builder produces files at DAQ startup, with this information.

More information on the histograms being displayed is available as well as a facility to locate spiky or dead zones in a histogram. Additional functionality such as change of scale is useful to check the detailed structure of the histograms.
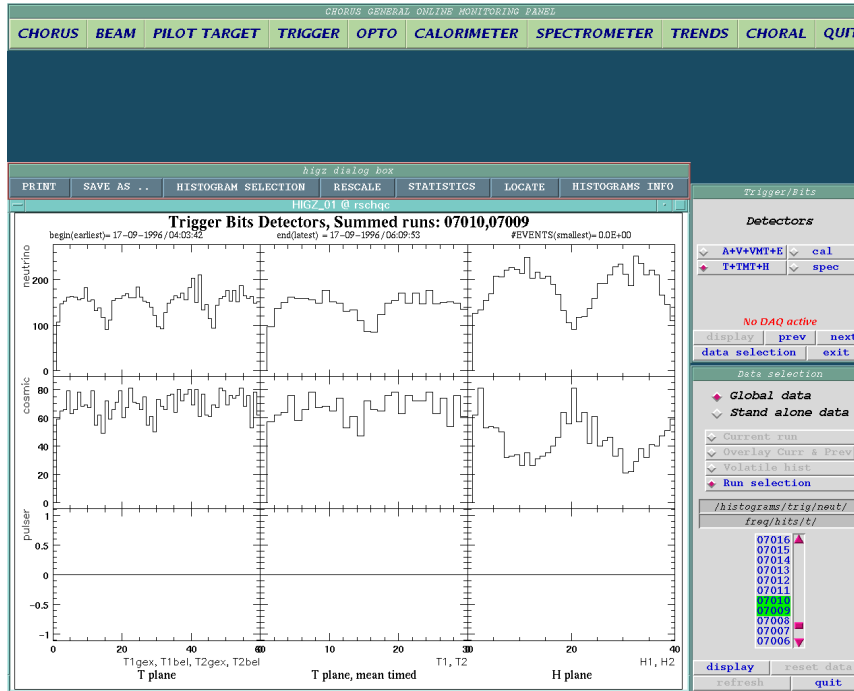
Figure 2.14: The online monitoring histogram viewer. As an example the hit distributions of the trigger planes T (singles and mean-timed) and H are displayed for neutrino events and cosmic events and for trigger calibration events (pulser) for the runs 7009 and 7010.

Chapter 3

Data analysis

In this chapter the analysis procedure with its steps is described. First of all an overview is given. Then the muon track reconstruction, the vertex finding and the computation of the kinematical variables are discussed. Thereafter the run and event selection is described, and a first comparison of data with simulated events is made. From Monte Carlo studies the reconstruction and trigger acceptances are determined and the background is evaluated. Finally the data are arranged for the fitting procedure in the next chapter, and a discussion and summary are given.

3.1   Introduction

The aim of our work is to probe the structure of the nucleon, particularly the (Bjorken-x) distribution of strangeness—strange sea quarks and antiquarks—in shape and magnitude. It is achieved by studying deep inelastic neutrino induced events with two emitted opposite sign muons and a hadronic shower in the final state. One muon originates from the charged current (CC) interaction of the neutrino with the nucleon producing a charm quark. The second muon emerges from weak decay of the charmed hadron resulting from fragmentation of the charm quark. Thus not only the strangeness distribution in the nucleon, but also the charm production mechanism, fragmentation, and muonic decay of charmed hadrons enter in our studies.

To describe the charm production dimuon cross-section in LO QCD (Equation 1.48) four independent kinematical variables are needed; we choose E_ν^{vis}, x^{vis}, y^{vis}, and z_l^{vis}. The label "vis" stands for "visible" and is used here to

3. Data analysis
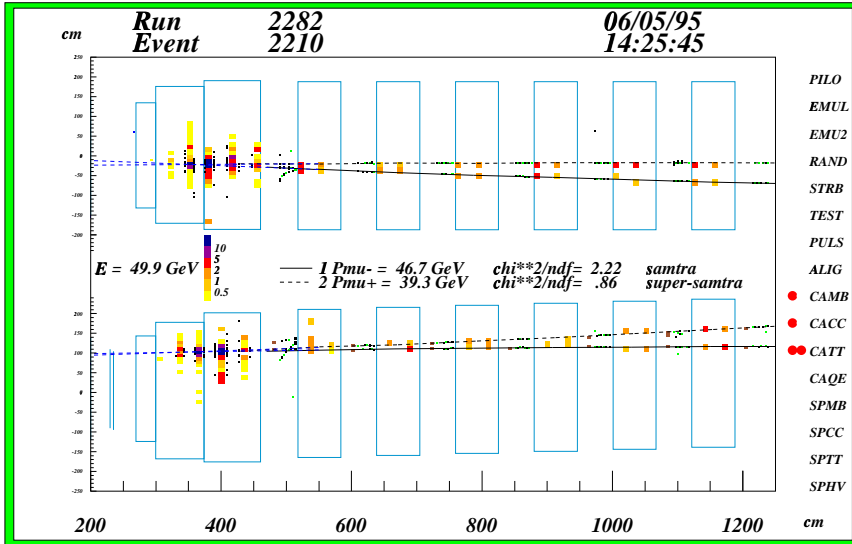
Figure 3.1: An example of a $\mu^-\mu^+$ event originating in the CHORUS calorimeter, top view (top) and side view (bottom). The neutrino beam comes from the left. The energy of the primary (negatively charged) and secondary muon are $E_{\mu 1} = 48.2$ GeV and $E_{\mu 2} = 40.8$ GeV, respectively. The shower energy $E_{had}^{vis} = 46.9$ GeV, $Q^{2,vis} = 29.3$ GeV$^2/c^2$, $x^{vis} = 0.178$, and $y^{vis} = 0.645$.

indicate that the corresponding value of the kinematical variable is only approximate because the neutrino from charm decay can not be detected experimentally. Due to the small number of events a statistically meaningful four-dimensional analysis of the experimental data can not be achieved. Instead the data are projected in terms of "standard" distributions: a one dimensional histogram of the fragmentation variable z_l^{vis} (10 intervals) and a two dimensional histogram of the neutrino energy E_ν^{vis} versus Bjorken x^{vis} (8×5 intervals).

To measure the above process the CERN neutrino beam is used with the CHORUS calorimeter as target, which provides at the same time a measurement of the energy and direction of the hadronic shower. The momenta and charges of the two muons are determined with the CHORUS muon-spectrometer. An example of such an event is shown in Figure 3.1.

Signals of the CHORUS calorimeter, spectrometer, and other sub-detectors are recorded as "raw" data. Over a running period of one year they amount to

about 400 Gb. These data include physics events from so called emulsion, calorimeter, and spectrometer triggers, as well as calibration events. The present analysis is based on the data recorded during the 1995 running period, originating in the calorimeter and fulfilling the calorimeter two-track trigger condition. This amounts to about 1.2M events corresponding to about 12 Gb of data. The total amount of calorimeter two-track trigger events covering the years 1994-1998 constitute about five times the data used in our analysis.

Event reconstruction starts from the raw data using the analysis package CHORAL [108]. The analysis process involves a series of steps. The calibration of the calorimeter and muon-spectrometer is performed first. Thereafter —as outlined below— the muon track parameters and momenta as well as the energy of the hadronic shower are determined for each calorimeter two-track trigger event. With this information the vertex location and kinematical variables are computed.

With a global checking procedure inappropriate and unreliable runs are removed, such that accepted data runs are internally consistent. By applying "safe" kinematic cuts to the data we select events of interest while rejecting part of the background. The 949 events thus obtained constitute our "experimental data" sample. In addition a similarly accepted sample of 144 same-sign negative dimuon events is used to study the behaviour of the background.

To extract the desired physics information from the experimental data a comparison is needed with a model which is implemented in a Monte Carlo (MC) generator. Our choice here is the charm event generator MCDIMUON, based on the "dimuon" model described in Chapter 1. It simulates the neutrino induced production, the fragmentation and subsequent muonic decay of the charm quark. The z_l^{vis} distribution is particularly sensitive to the fragmentation process, the two-dimensional $(x^{\mathrm{vis}}, E_\nu^{\mathrm{vis}})$ distribution to the mass of the charm quark, as well as to the strangeness content and distribution in the nucleon. The average branching ratio of charmed hadrons into muons is related to the overall normalisation of both histograms. Finite detector resolution, reconstruction and trigger inefficiencies distort the data, thus one must correct for these effects. In MCDIMUON the hadron shower is represented by a single four-vector, not suitable for the CHORUS detector simulation programme EFICASS and therefore can not be used for this purpose. Instead, a more generally applicable chain of MC simulation programmes is used to calculate the trigger and reconstruction acceptance correction in each interval of the standard distributions. This chain consists of the following programmes: 1) the neutrino beam generator GBEAM, 2) JETTA to generate deep inelastic neutrino events

with opposite sign dimuons in the final state, 3) the CHORUS detector simulation programme EFICASS, and 4) the reconstruction programme CHORAL, which can be used for MC events as well as for real data. Using this MC chain we derive the ratio for each interval of the number of accepted over generated events. These ratios are used to correct the real data for various acceptances.

Furthermore an estimate is needed for background—not originating from charm production and decay—with two opposite sign dimuons and a hadronic shower in the final state. Such events arise from the decay of mainly pions and kaons produced in the interaction and contribute to same-sign and opposite-sign dimuons alike. The background is evaluated in two ways. First the shape of the same-sign dimuon, $\mu^- \mu^-$, distribution is assumed to be the same as for the $\mu^- \mu^+$ background apart from a scale factor obtained from a MC study. This preliminary estimate is used to perform a global check on our data and to make a series of comparisons between JETTA and our real data. A more refined way corrects the real $\mu^- \mu^-$ data for the scale factor in each interval of the standard distributions. The real data and best determined background estimate, with corrections for detector effects provide our final set of histograms. Together they embody the input data for our fitting procedure of Chapter 4 to obtain our main physics results.

3.2   Muon track reconstruction

After the calibration (Section 2.8) the muon spectrometer data are processed to find muon tracks and to determine their momentum and charge sign. In the CHORAL package different methods are applied in parallel. The track finding part of the SAMTRA method is based exclusively on the drift chamber information while DATSPC (Digital Analog Time information in the SPeCtrometer) uses streamer chamber data—both wire and strip hits—as well. Both methods are based on a fast tree algorithm [113] to find track projection candidates in each of three drift-chamber projections, and of two streamer-tube projections. The whole sample of track projection candidates is subjected to 3D reconstruction criteria to obtain space track candidates. For this process DATSPC uses the driftchamber hits consistent with the projection candidates.

The momentum is determined with different fit methods through the space tracks. The BLFIT procedure is based on averaging the bend-angles in individual spectrometer magnets. The momentum fitting part of SAMTRA uses a global fit along the length of the track taking into account the energy loss in iron and scintillators and multiple scattering [100, 114]. A third method, Super-

SAMTRA, uses the DATSPC tracks and the corresponding driftchamber hits together with the SAMTRA momentum fitting part to obtain a momentum value. For muons in the low momentum range the CAMMOR method is applied to determine the stopping range [90] inside the spectrometer, allowing to derive the momentum through the range-energy relation [91]. This method provides a better resolution (factor 2 at 5 GeV/c which increases towards lower momenta) compared to the other ones, but only works below 5 GeV/c.

Each of the above methods can result for each muon in a track vector with starting point and direction at the entry plane of the spectrometer, momentum value and charge sign (except CAMMOR). Thus for each muon track in each event there are usually several track candidates and momentum values. A decision routine chooses the "best" result, taking into account the reconstructed track length, the fit quality (χ^2), and whether the muon stopped inside the muon-spectrometer. The result is added to the event information.

We note that the detection and reconstruction inefficiencies are reduced by using two independent track finding methods based on different detector information, drift versus streamer chambers. For the final sample of our analysis (see Section 3.6) about 65% of the muons have their final momentum value obtained by SAMTRA, the other ones by Super-SAMTRA. This fraction turns out not to depend on the fitted muon momentum. CAMMOR does not contribute due to the cuts on the muon energy and track length and BLFIT results are removed by the decision routine which chooses the "best" result.

3.3 Vertex finding

When at least one muon track is found, the next step is to check whether the event is consistent with the interaction of a neutrino in the calorimeter. The actual primary interaction point (the "vertex") for calorimeter events can be found using calorimeter (scintillator) information, or muon-spectrometer track information, or a combination of both. To allow efficiencies to be almost independent of the event type (single or multiple muons), track information of only one muon is used.

The vertex position along the beam direction, the x direction, can be found approximately by using the signals of the calorimeter scintillator planes. Several variations of the method have been investigated using Monte Carlo data. The vertex is positioned 1) in the middle of the most upstream scintillator plane with an energy deposit larger than some preset threshold value; 2) the same as 1) but in addition requiring that all scintillator planes downstream

should also have a signal above the same preset threshold; 3) in the middle of the scintillator plane where some preset upstream fraction of the total calorimeter energy is deposited; 4) the same as 3) but using the signals for a linear interpolation over the thickness of the "vertex" plane. The typical accuracies of the four methods are 6.3, 8.0, 5.9 and 5.2 cm (RMS) respectively.

Including track information from the muon with the highest momentum— the error due to multiple scattering in the calorimeter is then smallest—has also been studied. The muon track found in the muon-spectrometer is retraced upstream through the calorimeter. Calorimetric information is supplied by measuring the total energy and direction of showers in the calorimeter. Thus we come to two other methods: 5) the point of closest approach between the backtracked highest momentum muon and the hadronic shower direction (linear fit to the centres of gravity of the scintillator signals for each calorimeter plane); and 6) backtracking the highest momentum muon from the spectrometer into the calorimeter, and positioning the vertex where the track and the most upstream scintillator hit are mutually compatible. These two methods have an accuracy of 28, 3.2, 3.8 cm and 14, 2.4, 2.5 cm for the x, y, z directions respectively. We note that the accuracy in the x direction is a factor of two larger than for the previous methods. For the fifth method this is due to the small angle between the muon momentum vector and the direction of the hadron shower, while for the sixth method it arises from the 9 cm width of the calorimeter scintillators. For checking purposes events with more than one muon are used by backtracking the two most energetic muons. The vertex is located at the position where the distance between the two tracks reaches a minimum compatible with the uncertainty due to multiple scattering of the two muons. This method has an accuracy of 25, 1.8, 2.1 cm for the x, y, z directions respectively. Its results are consistent with the other methods, in all cases where the two muons come from the same vertex. That criterion is satisfied if the calculated minimum distance between the two muon tracks in the vertex plane—the calorimeter scintillator plane where the vertex is positioned—is smaller than some preset value of about 10 cm. The accuracy in the x direction is about 4 times smaller than in the first four methods due to the small angle between the muons and their multiple scattering.

On the basis of various MC studies the best method turns out to be a combination of methods 4 and 6 (see also [115]). The vertex x coordinate is found most accurately by using calorimeter scintillator energy information only. The optimum location is found where a specific fraction of the total calorimeter energy is deposited upstream of the scintillator vertex plane, determined with
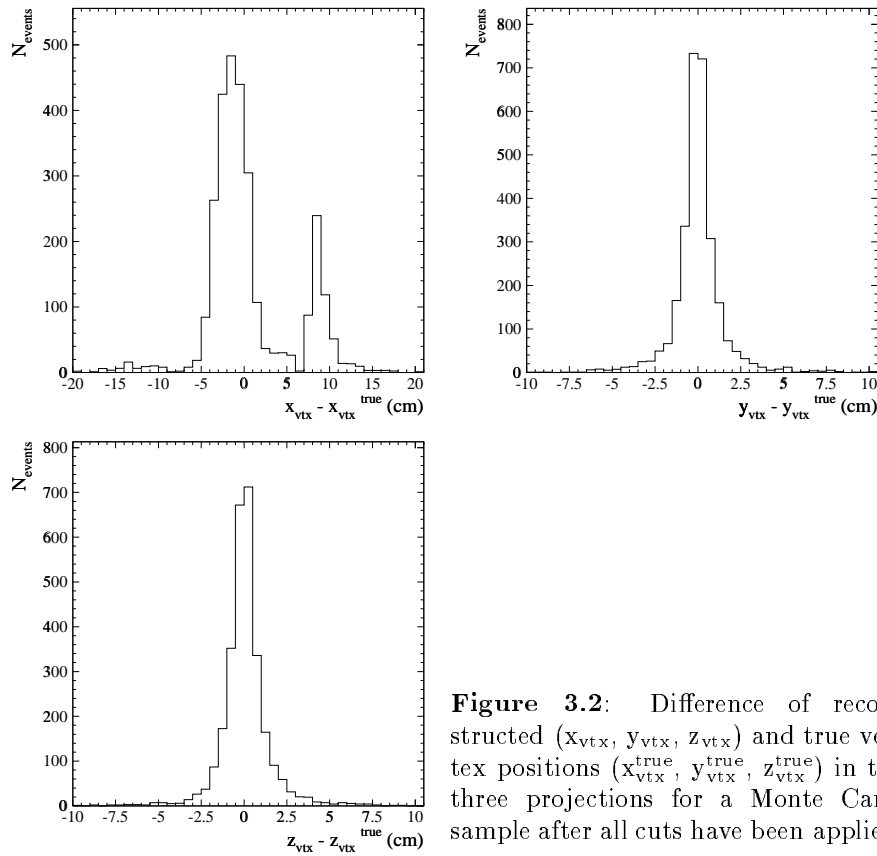
Figure 3.2: Difference of reconstructed (x_{vtx}, y_{vtx}, z_{vtx}) and true vertex positions (x_{vtx}^{true}, y_{vtx}^{true}, z_{vtx}^{true}) in the three projections for a Monte Carlo sample after all cuts have been applied.

method 4. This fraction (2.5%) can be understood in terms of the average energy deposit backward with respect to the interaction vertex. A drawback of the latter method is that it fully relies on MC events for determining the specific fraction. The y and z coordinates of the vertex are found by extrapolating the track of the highest momentum muon to the vertex plane. The resolutions obtained by the applied method are shown in Figure 3.2. The distribution of the vertex deviations in the beam direction has a double peak structure, where the second peak corresponds to a vertex misidentification by one calorimeter scintillator plane of about 10 cm downstream of the true vertex position. The deviations for the y and z coordinate are centred around zero. The estimated accuracy (RMS) of the final vertex finding procedure is found to be 5.2 cm in x, 1.6 cm in y and z, respectively. In the data no distinction can be made between

the two peaks of the vertex resolution in the x direction, so the total RMS is given. The dependence on single or multiple muon track events is found to be negligible. By applying this procedure to the real data, the estimate of the vertex position in the calorimeter volume is determined and added to the event information.

3.4   Kinematical variables

Once the muon track parameters as well as the vertex coordinates are known for each event, the reconstructed muon parameters at the vertex are computed. This results in $\vec{p}_{\mu i}$, $E_{\mu i}$ for $i = 1, 2$, where index 1 denotes the "leading muon", the muon with the highest momentum of the negatively charged ones. In case of single negatively charged muon events $\vec{p}_{\mu 2}$ and $E_{\mu 2}$ are set to zero. The calculated muon energy loss in the calorimeter is subtracted from the measured total energy deposit to obtain the shower energy $E_{\mathrm{had}}^{\mathrm{vis}}$, where the label "vis" indicates that the neutrino from charm decay escapes detection (see Chapter 1). No correction for missing energy in the calorimeter event due to shower leakage into the muon spectrometer is applied. The following experimental kinematical variables are derived:

- $E_{\nu}^{\mathrm{vis}} = E_{\mu 1} + E_{\mu 2} + E_{\mathrm{had}}^{\mathrm{vis}}$

- $Q^{2,\mathrm{vis}} = 2 E_{\nu}^{\mathrm{vis}} (E_{\mu 1} - \vec{p}_{\mu 1} \cdot \vec{x}_{\nu}) - m_{\mu}^2$, where $\vec{x}_{\nu}$ is the unit vector parallel to the neutrino beam direction

- $x^{\mathrm{vis}} = Q^{2,\mathrm{vis}} / (2M [E_{\mu 2} + E_{\mathrm{had}}^{\mathrm{vis}}])$

- $z_l^{\mathrm{vis}} = E_{\mu 2} / (E_{\mu 2} + E_{\mathrm{had}}^{\mathrm{vis}})$

Once muon tracks and momenta, the vertex location, and the kinematical variables are computed and added to the event information we can select the appropriate dimuon data.

3.5   Run selection

For the final analysis we need to ensure that the data are internally consistent and represent a stable state of the CHORUS apparatus. Therefore we developed a method to select runs. The data are grouped according to data taking runs, covering usually periods of 1 to 2 hours and including about 600 calorimeter

two-track trigger events. The stability and consistency of measured variables are checked by studying the run dependence of their average behaviour. This is particularly important because the calorimeter signals are not always stable. We note that of the about 600 events per run on average 0.8 survive in our final data sample. This is due to trigger impurities, single muon events with shower leakage into the spectrometer, and selections and cuts presented in the next section. The criteria for accepted data runs, after applying the calorimeter and muon–spectrometer calibration and only considering events fulfilling the calorimeter two-track trigger condition, are the following.

First, it is verified that the trigger definition is correct. Then for the average energy deposit in the individual calorimeter planes the runs with the largest deviation are spotted by an automatic procedure. For these runs an eye-scan of histograms with all calorimeter information per read-out cell is made to determine misidentified "hot" or "dead" channels. Runs containing these are eliminated.

Furthermore, minimum requirements are set as a quality check. The average number of protons on target per burst is required to be above $0.5 \cdot 10^{13}$. The number of calorimeter two-track trigger events is taken to be at least 200 and the number of non-reconstructible events less than 5%. Runs with deviations of the mean trigger deadtime larger than four times the normal value are removed as well. Unstable running periods with similar variations in the number of triggers per proton on target are also rejected.

By selecting events with at least one muon and applying some loose cuts, the average values per run for the following important variables are calculated: the total calorimeter energy, the vertex position, the track fit-quality and the momentum of the leading muon, the hadronic energy, the neutrino energy, and the kinematic variables Q^2, ν, W^2, x and y. For all these variables the runs with the largest deviations are removed successively in an automatic procedure until the total χ^2 probability is larger than 10^{-3}. At this level no significant bias is introduced.

Using the above described criteria, from the available 2172 calibrated runs 969 runs (approximately 30% of the calorimeter two-track trigger data) are not included in the physics analysis. One third of the thus removed events is lost because of unidentified dead or hot channels in the calorimeter, the other data loss being rather evenly due to the other selection criteria.

To improve the remaining data set we apply selections to the individual events of the runs that pass the run selection.

3.6   Event selection

To select muons we require the muon–spectrometer tracks to reach at least the fifth spectrometer tracking gap. This is needed to obtain an acceptable momentum measurement and to exclude non-muon tracks from punch-through hadrons (mostly pions). Muons that are not properly related in time to the neutrino interaction (mostly out-of-time beam muons) are rejected, by requiring that at least three spectrometer scintillators in each projection have in-time hits within 170 ns along the muon track. If this is not the case for all muons, the event is discarded.

As described in Section 2.9 a hit in the H scintillator plane within a 50 ns time window vetoes the event. After applying all cuts about 15% of the events is lost due to this H-plane veto. For MC events from the CHORUS detector simulation programme EFICASS, no time information is provided, and thus no time window veto can be applied. Therefore, in this case all events with a H-plane hit are vetoed. Due to this discrepancy between the real CHORUS trigger data and the simulated data, in first instance more events are vetoed in the simulation than in real data. This discrepancy, however, is largely removed by increasing—for the real data—the veto time window from 50 ns to 2 μs for hits in the H plane using TDC information.

In accordance with the trigger fiducial volume the vertex is required to be located in the calorimeter with a cross section of 180×180 cm^2 around the beam axis. To solve the H-plane veto problem up to the level required by our approximate simulation and statistical precision, we apply a fiducial cut such that events with their vertex in the EM sector are not included. Effectively we only use the first hadronic sector of the calorimeter as our target.

Events are selected when the two most energetic muons have opposite charge or—to estimate the background—both have negative charge. Moreover, the two muon tracks have to be consistent with a common charm production and decay region. Therefore the distance d_{yz} between the two muon tracks in the vertex plane has to be smaller than 10 cm. Hereby tracking information inside the calorimeter is not used, so the muon track vectors at the vertex are—apart from a translation—identical to those found by the spectrometer track-fitting. Distributions of d_{yz} and the two projections d_y, d_z as shown in Figure 3.3, are centred around zero with an RMS of about 3 cm. Events where the distance is larger than 10 cm are mostly due to background and therefore discarded.
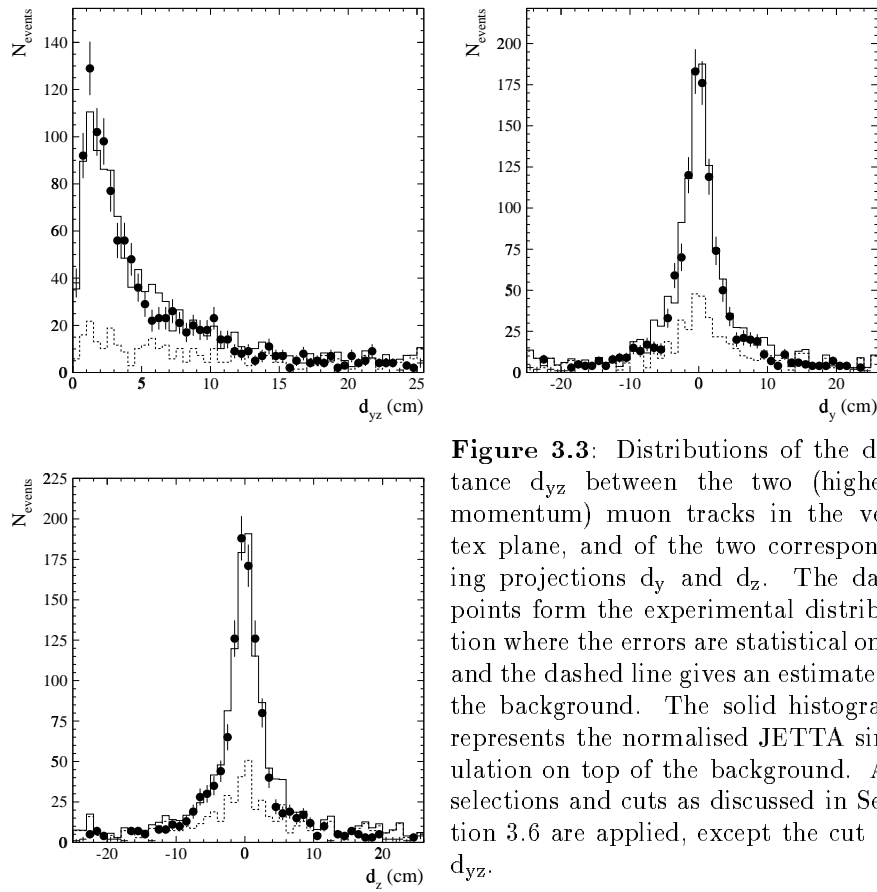
Figure 3.3: Distributions of the distance d_{yz} between the two (highest momentum) muon tracks in the vertex plane, and of the two corresponding projections d_y and d_z. The data points form the experimental distribution where the errors are statistical only and the dashed line gives an estimate of the background. The solid histogram represents the normalised JETTA simulation on top of the background. All selections and cuts as discussed in Section 3.6 are applied, except the cut on d_{yz}.

The final sample to be used because of the model limitations is obtained by imposing the following additional selections:

- The muon energies $E_{\mu1}$, $E_{\mu2} > 6$ GeV and the hadronic energy $E_{\text{had}}^{\text{vis}} > 5$ GeV,

  to ensure good reconstruction quality and control over acceptances. The high muon energy criterion also drastically reduces the meson decay background (Section 3.9).

- $x^{\text{vis}} < 0.5$ and $Q^{2,\text{vis}} > 5.5$ GeV$^2/c^2$,

  dictated by the choice of the parton distribution parametrisation. The first cut is applied because the CTEQ 3L [27] parton distributions in the

MC model are without correction for nuclear effects in our lead target nuclei. The nuclear effect can be relatively large at $x > 0.5$ [116, 117]. The $Q^{2,\mathrm{vis}}$ criterion is set because the parton distributions used in the MC model are valid for $Q^2 > 4 \ \mathrm{GeV}^2/c^2$.

- $E_\nu^{\mathrm{vis}} > 35 \ \mathrm{GeV}$,

  to ensure a consistent description of the fragmentation process for neutrino data [51] and e^+e^- data [48], and to reduce the amount of Λ_c^+ produced as mentioned in Section 1.3.

For events with more than two muons, the two most energetic muons are used in the subsequent analysis. The muon from the primary vertex, the leading muon, in the $\mu^-\mu^-$ background sample is assumed to be the most energetic one, and in the $\mu^-\mu^+$ sample it is the μ^- by definition, thus implicitly assuming that all events are ν_μ (not $\overline{\nu}_\mu$) induced. This last assumption can be made because the $\overline{\nu}_\mu$ contamination in the CERN ν_μ beam is small ($\overline{\nu}_\mu/\nu_\mu = 5.3\%$), and the kinematical selection reduces this contamination to 1.6%. The final number of opposite sign dimuon events after applying all selections and cuts is 949. For the same-sign dimuon background sample this is 144.

3.7 Comparison of data and Monte Carlo

Various MC simulation programmes are used. The neutrino beam generator GBEAM [79] describes the interaction of SPS beam protons with the WANF beryllium target for the production of mesons. The mesons are tracked subsequently through the horn, reflector and the decay tunnel. Their decay produces neutrinos with given flavour, creation-vertex and four-momentum.

With the GBEAM neutrinos as input the event generator JETTA (Section 1.7.2) generates neutrino-induced opposite-sign dimuon events. It describes the hard scattering neutrino-nucleon interaction as well as fragmentation of the produced quarks, and the decay of short-lived particles, like τ, $\mathrm{D}^\pm$, D^0, $\overline{\mathrm{D}}^0$, $\mathrm{D}_s^\pm$ and $\Lambda_c^\pm$.

The simulation of the interactions and shower development in the CHORUS detector is performed in EFICASS (Emulsion FIbre Calorimeter Spectrometer Simulation) using the GEANT package [118]. EFICASS contains the complete geometrical setup of the detector, takes care of the tracking of particles through active and passive media, and converts the information of the active elements into detector "signals", representing the calibrated raw data response of the apparatus. These signals are stored in the same format as delivered by the

DAQ system in order to be processed in the same way as the real data by the same reconstruction and analysis programme CHORAL. In the MC case the initial physics simulation parameters based on previous experiments are included in the event description.

To check the overall consistency of our dimuon data—after selections and cuts—we show in Figures 3.4-3.7 the data in one-dimensional projections for many different kinematical variables. In these figures the data points represent the experimental opposite sign dimuon distributions, the dashed line a corresponding estimate for the background and the solid line the MC distributions, on top of the background. The background distributions are experimental $\mu^-\mu^-$ distributions (with 144 events) multiplied by a factor 1.45, as determined in Section 3.9 using the JETTA MC generator. In this estimate a symmetry is assumed between the positively and negatively charged mesons in the hadronic shower. The MC sample (2882 events) is normalised to the background subtracted number of events.

The shapes of the distributions are in most cases influenced by our data selection.

- The vertex distribution in the x direction, x_{vtx}, should in principle be flat, but it decreases towards lower x_{vtx} due to the H plane veto (Section 2.9). The distributions in the y and z direction are symmetric and centred around the beam axis.

- The mean $E_{\text{had}}^{\text{vis}}$ is about 39 GeV, the mean $Q^{2,\text{vis}}$ is about 20.7 GeV$^2/c^2$, and the mean $W^{2,\text{vis}}$ is about 82 GeV$^2/c^2$.

- The leading muon mean energy is about 40 GeV and larger than the secondary muon energy (about 15 GeV). This difference is indicative for distinct production mechanisms.

- The leading muon average track angle is about 0.1 while for the secondary muon it is about 0.07 radians.

- The distributions for the azimuthal angles is flat for both muons, consistent with expectations, because of the azimuthal symmetry of the physics and the CHORUS apparatus.

- The leading muon average transverse momentum with respect to the neutrino is about 2.6 GeV/c, while for the secondary muon it is about 0.86 GeV/c. This difference reflects mostly the difference in the muon energy distributions.

79

3. Data analysis
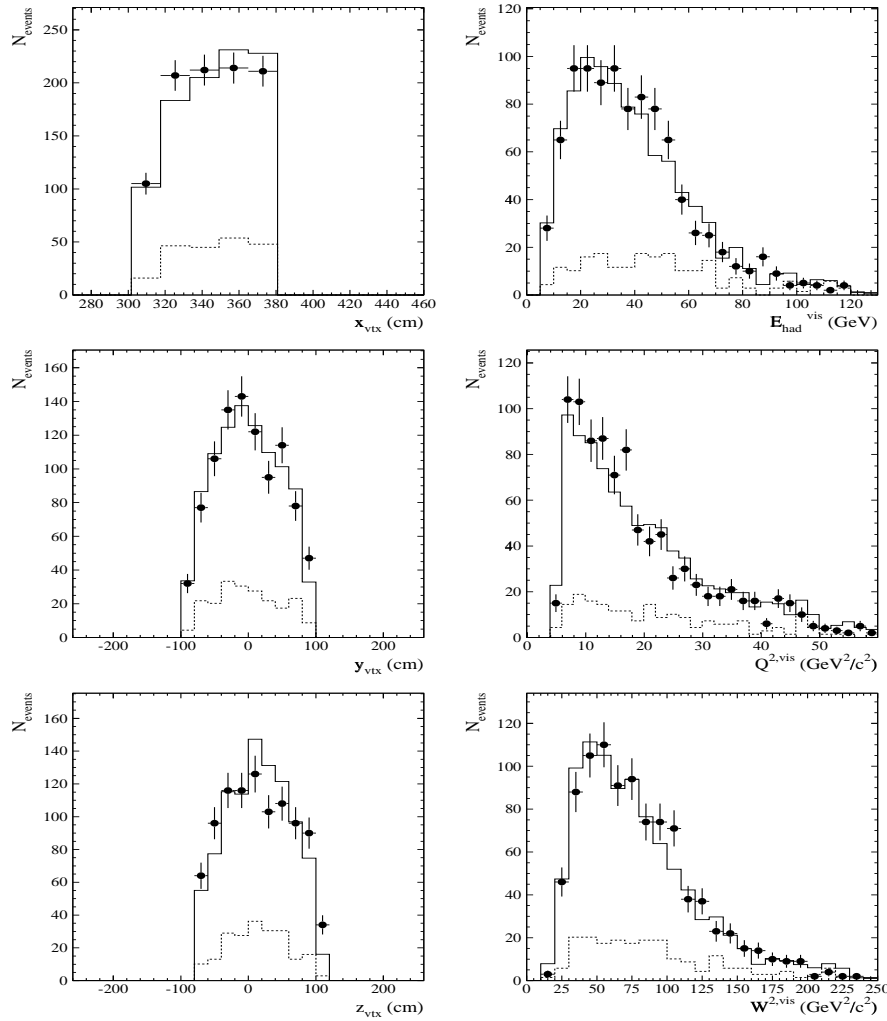
Figure 3.4: Comparison between real data and MC (JETTA) simulated opposite sign dimuon distributions for the vertex position in the x (x_{vtx}), y (y_{vtx}) and z (z_{vtx}) direction (figures at left) and for the kinematical variables E_{had}^{vis}, $Q^{2,vis}$, and $W^{2,vis}$ (figures at right). The data points are the experimental distributions where the errors are statistical only. The solid line represents the simulated distribution on top of an estimate for the background (dashed line).
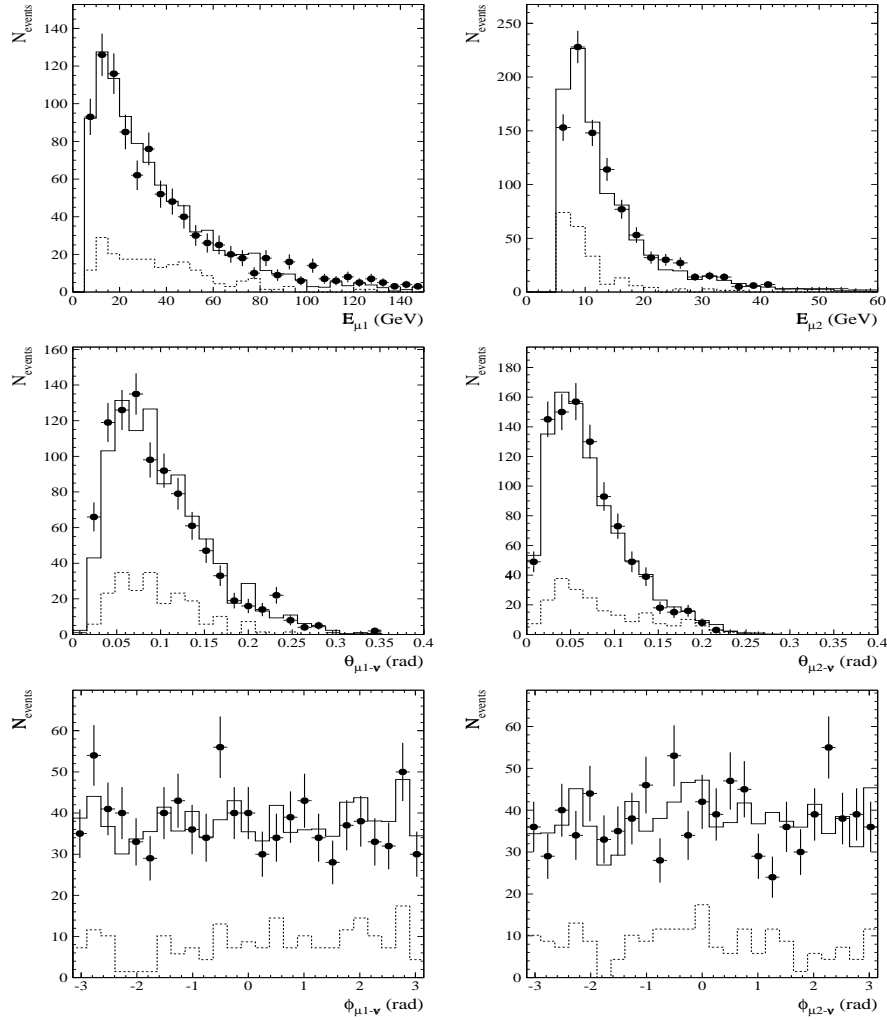
Figure 3.5: Comparison as in Figure 3.4 for the energy of the primary and secondary muon $E_{\mu 1}$ and $E_{\mu 2}$ (top), the muon track angles with respect to the neutrino beam, $\theta_{\mu 1-\nu}$ and $\theta_{\mu 2-\nu}$ (middle), and the corresponding azimuthal angles, $\phi_{\mu 1-\nu}$ and $\phi_{\mu 2-\nu}$ (bottom).
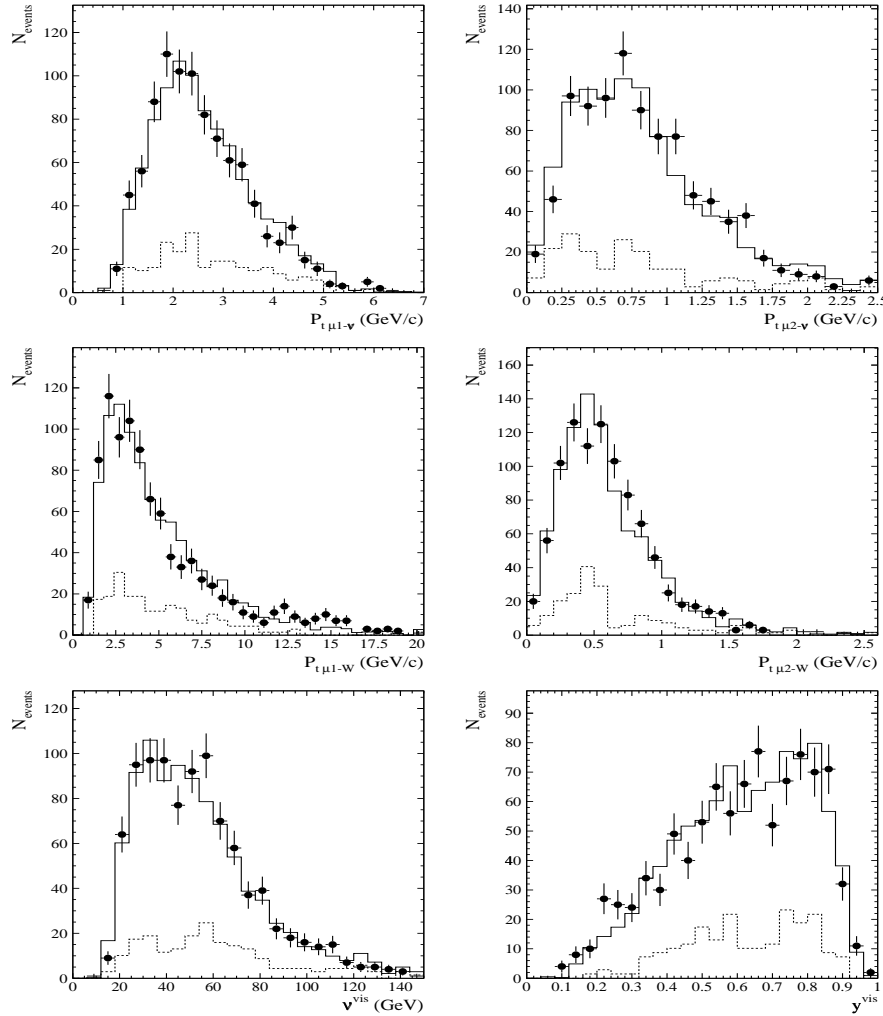
Figure 3.6: Comparison as in Figure 3.4 for transverse muon momenta with respect to the neutrino beam direction, $P_{t\mu1-\nu}$ and $P_{t\mu2-\nu}$ (top), and with respect to the reconstructed W-boson direction, $P_{t\mu1-W}$ and $P_{t\mu2-W}$ (middle), and for ν^{vis}, and y^{vis} (bottom).
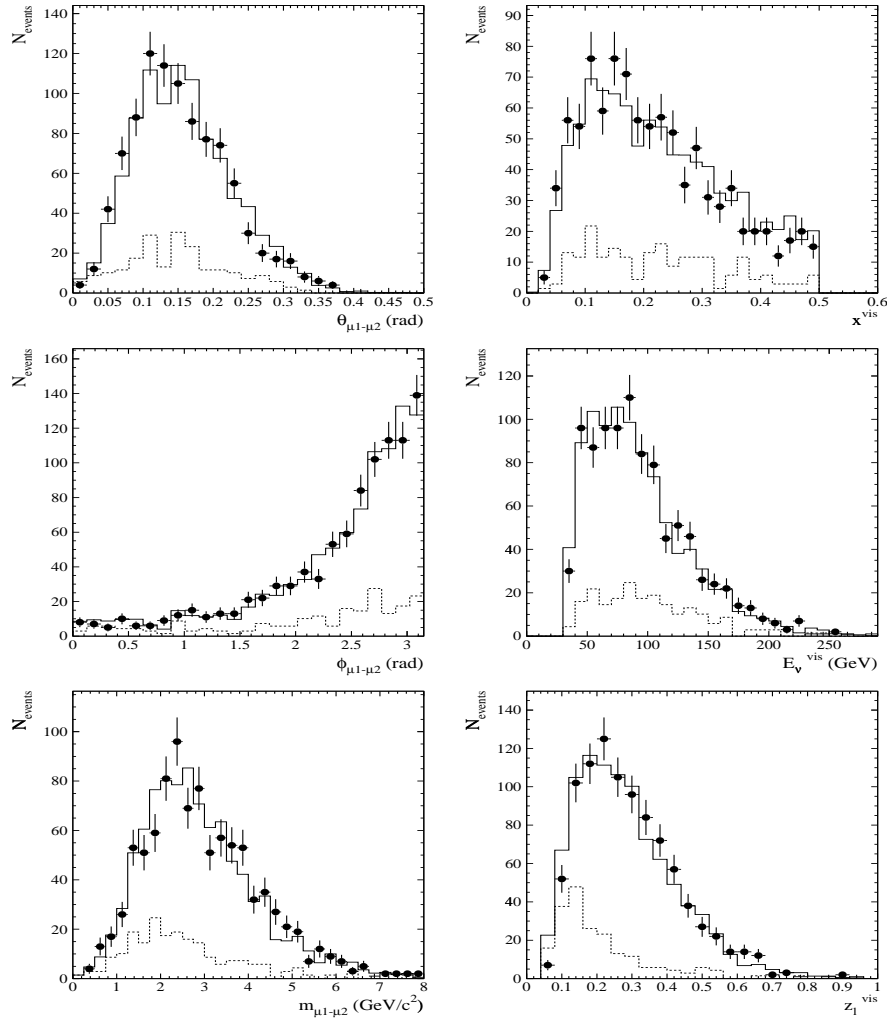
Figure 3.7: Comparison as in Figure 3.4 with on the left side the angle between the two muon momentum vectors, $\theta_{\mu 1 - \mu 2}$, the azimuthal angle between the two muon momentum vectors, $\phi_{\mu 1 - \mu 2}$, the invariant mass of the two muons, $m_{\mu 1 - \mu 2}$. On the right hand side the Bjorken x^{vis}, the neutrino energy E_ν^{vis}, and the fragmentation variable z_l^{vis}.

- The leading muon average transverse momentum with respect to the reconstructed W-boson direction, $P_{t\mu 1-\text{W}}$, is about 5.4 GeV/c, while for the secondary muon, $P_{t\mu 2-\text{W}}$, it is about 0.63 GeV/c. Although not needed for our analysis, it is clear that using the $P_{t\mu 1-\text{W}} > P_{t\mu 2-\text{W}}$ selection a global way to characterise opposite dimuon events as those induced by either ν_μ or $\overline{\nu}_\mu$ can be found.

- Although, the y^{vis} distribution for CC events should be flat, due to the cuts on $E_{\text{had}}^{\text{vis}}$, $E_{\mu 1}$, $E_{\mu 2}$ and E_ν^{vis} and the presence of the charm threshold the distribution is distorted.

- The average opening angle for the two muon tracks is about 0.15 radian, while the average azimuthal angle between the two muon momentum vectors is about 2.4 radian. The two muon momenta are almost back to back in the plane perpendicular to the neutrino beam.

- In the invariant mass distribution of the two muons no $J/\psi(1\text{S})$-signal around 3.1 GeV/c^2 is present; this is because of the small cross section and the $E_{\text{had}}^{\text{vis}} > 5$ GeV cut.

- The x^{vis} distribution has an average of about 0.22 and its shape is expected from the applied cuts and the underlying s and d quark distribution functions.

- The E_ν^{vis} spectrum with an average of 94 GeV is correlated with the E_ν spectrum, and effected by the charm threshold.

- The average z_l^{vis} is about 0.29.

We conclude that in the 24 projections, the background estimate together with the JETTA MC data are—within the statistical accuracy—in good overall agreement with the real data. This provides a good starting point for an elaborate understanding of our acceptance and background corrections, and for the final preparation of our data to allow quantative parameter fitting and their physics interpretation.

3.8 Reconstruction and trigger acceptance correction

To evaluate the reconstruction and trigger acceptance the JETTA MC chain—described in Section 3.1—is used to generate opposite sign dimuon events.

The first muon originates from the charged-current neutrino-nucleon interaction process producing among others a charmed hadron. The second muon comes from the semi-leptonic decay of the charmed hadron. The standard Jetset fragmentation scheme is used to describe the hadronisation process in detail, although the threshold behaviour of the charm quark production is not properly taken into account. The JETTA output events are utilised as input to EFICASS to obtain the corresponding detector responses. From the input and output events of EFICASS our standard distributions as discussed in Section 3.1 are obtained. The bin-by-bin ratios from these input and output distributions represent the MC predictions for the detector acceptances. In our case these ratios are almost insensitive to details of the assumptions in JETTA, including those of the charm production cross section.

For each interval in the $(x^{\mathrm{vis}}, E_\nu^{\mathrm{vis}})$ or z_l^{vis} distributions the total acceptance, $\varepsilon_{\mathrm{tot}}$, can be factorised as follows:

$$\varepsilon_{\mathrm{tot}} = \frac{N_{RCT}}{N_G} = \frac{N_{GC}}{N_G} \cdot \frac{N_{RC}}{N_{GC}} \cdot \frac{N_{RCT}}{N_{RC}} = \varepsilon_{\mathrm{cut}} \cdot \varepsilon_{\mathrm{rec}} \cdot \varepsilon_{\mathrm{trig}}, \qquad (3.1)$$

where N_G denotes the total number of generated (GBEAM $\rightarrow$ JETTA $\rightarrow$ EFICASS) events in the interval, N_{GC} the number of events out of the N_G events that survive the applied cuts as calculated from the "vis" variables before the detector simulation (MC truth), N_{RC} the number of reconstructed events with cuts on the reconstructed variables (after detector simulation), and N_{RCT} the number of reconstructed events with cuts on the reconstructed variables and accepted by the trigger condition. The parameters $\varepsilon_{\mathrm{cut}}$, $\varepsilon_{\mathrm{rec}}$ and $\varepsilon_{\mathrm{trig}}$ represent the acceptance (efficiencies) for surviving cuts, reconstruction and triggering, respectively.

The total acceptances over the full parameter space are found to be $\varepsilon_{\mathrm{tot}} = 0.132 \pm 0.002$, $\varepsilon_{\mathrm{cut}} = 0.247 \pm 0.003$, $\varepsilon_{\mathrm{rec}} = 0.707 \pm 0.008$ and $\varepsilon_{\mathrm{trig}} = 0.755 \pm 0.007$, respectively where the errors are statistical only. We note that the values of these acceptances (except $\varepsilon_{\mathrm{tot}}$) depend on their definition given in Equation 3.1. Note that the total acceptance correction ($1/\varepsilon_{\mathrm{tot}} = 7.60 \pm 0.13$) is large, which—without special care—can result in sizable systematic effects.

Because we can not compare the JETTA generated events with the real data in the region outside our applied cuts, the acceptance correction applied in our detailed analysis only includes the reconstruction and trigger acceptance correction ($1/\varepsilon_{\mathrm{rec+trig}} = N_{GC}/N_{RCT} = 1.873 \pm 0.027$) and not the cut acceptance corrections. Furthermore we can only compare the JETTA model with the real data using distributions as a function of the visible kinematical vari-

ables. Therefore the acceptance correction implicitly transforms the real data distributions into corresponding distributions as a function of the "true" MC "visible" kinematical variables.

To properly calculate the combined reconstruction and trigger acceptance including smearing due to experimental uncertainties, we calculate for each interval the following numbers: $N_{GC\ RCT}$, number of events generated, reconstructed and trigger accepted, all in the same interval, $N_{GC\ \overline{RCT}}$, similarly number of events generated but not reconstructed and not trigger accepted, and $N_{\overline{GC}\ RCT}$, similarly number of events reconstructed and trigger accepted but not generated in that interval. The combined reconstruction and trigger acceptance is then given by

$$\varepsilon_{\text{rec+trig}} = \frac{N_{RCT}}{N_{GC}} = \frac{N_{GC\ RCT} + N_{\overline{GC}\ RCT}}{N_{GC\ RCT} + N_{GC\ \overline{RCT}}}, \tag{3.2}$$

and its variance is given by

$$\sigma^2_{\varepsilon_{\text{rec+trig}}} = \frac{1}{(N_{GC\ RCT} + N_{GC\ \overline{RCT}})^4} \left[(N_{GC\ \overline{RCT}} - N_{\overline{GC}\ RCT})^2 \sigma^2_{N_{GC\ RCT}} \right.$$
$$+ (N_{GC\ RCT} + N_{\overline{GC}\ RCT})^2 \sigma^2_{N_{GC\ \overline{RCT}}}$$
$$\left. + (N_{GC\ RCT} + N_{GC\ \overline{RCT}})^2 \sigma^2_{N_{\overline{GC}\ RCT}} \right]. \tag{3.3}$$

Similar formulae are used for calculating other acceptances when smearing is involved, like ε_{rec}. To calculate acceptance corrections without smearing, like the trigger or cut acceptance corrections, we use the same procedures with numbers connected to smearing put to zero.

The projected reconstruction acceptance ε_{rec} as a function of x^{vis}, E_ν^{vis}, and z_l^{vis} is shown in Figure 3.8. It is flat in x^{vis} with values around 0.7; for $E_\nu^{\text{vis}} > 100$ GeV it decreases with increasing E_ν^{vis} typically from 0.8 to 0.5, and it linearly increases from 0.4 to above unity with increasing z_l^{vis} (the acceptance larger than unity reflects an asymmetric in-out smearing effect). The E_ν^{vis} and z_l^{vis} distributions reflect shower leakage into the spectrometer which is not taken into account in the event kinematics. The reconstruction acceptance as a function of E_ν^{vis} for different x^{vis} bins (slices) is consistent with the projected distribution in Figure 3.8. Similarly, as a function of x^{vis} for different E_ν^{vis} bins all distributions are typically flat within statistical fluctuations. The trigger acceptance $\varepsilon_{\text{trig}}$ is also shown in Figure 3.8. The projected distribution is essentially flat in x^{vis} around 0.74. For increasing E_ν^{vis} it decreases from 0.85 to 0.65, and for increasing z_l^{vis} it increases from 0.65 to 0.85. The latter two
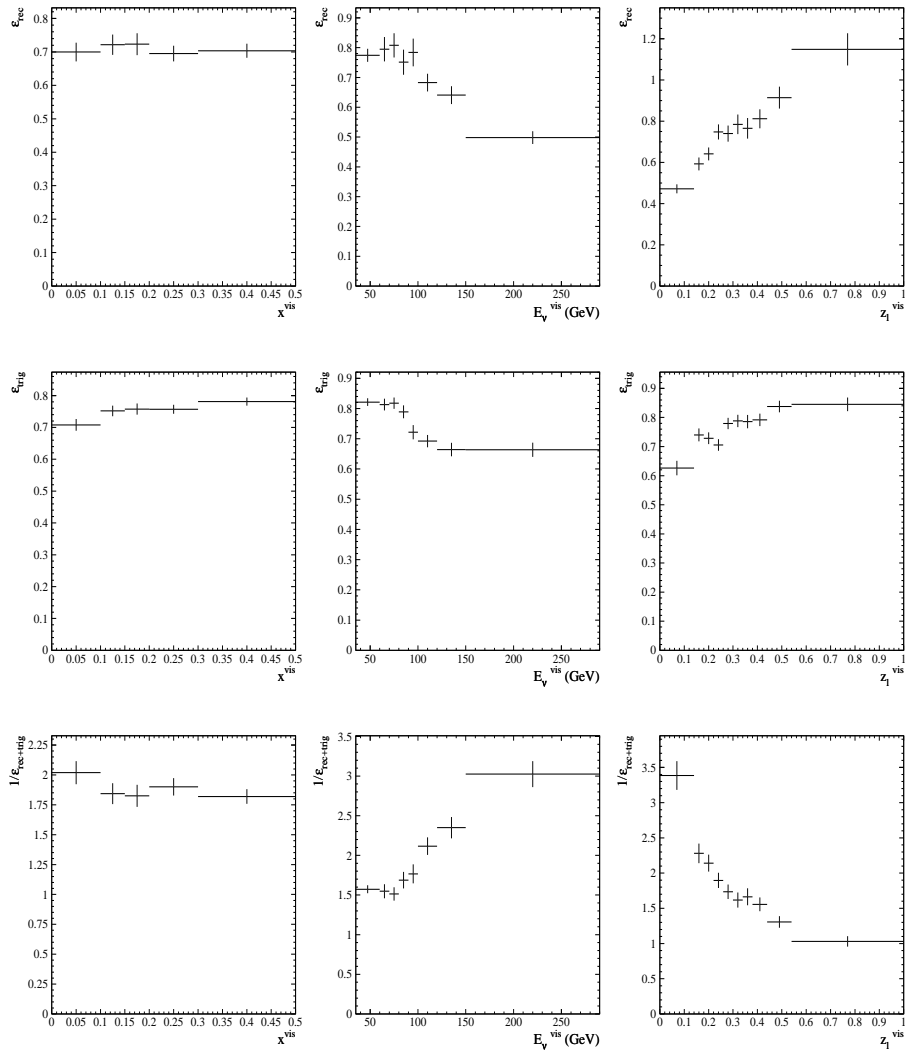
Figure 3.8: Reconstruction acceptance $\varepsilon_{\mathrm{rec}}$ (top), trigger acceptance $\varepsilon_{\mathrm{trig}}$ (middle), and acceptance correction $1/\varepsilon_{\mathrm{rec+trig}}$ (bottom) as a function of x^{vis}, E_ν^{vis} and z_l^{vis} as determined from a MC study. We note that $\varepsilon_{\mathrm{rec}}$ also includes smearing effects, so that locally it can become larger than unity. The errors are statistical only.

effects are due to the rejection of more and more events with increasing hadronic energy by the H-veto [119]. With increasing hadronic energy, for example, more slow neutrons emerge in the shower, resulting—after scattering—in increased activity in the H plane.

Having constructed acceptances for our standard histogram distributions (z_l^{vis}), $(x^{\mathrm{vis}}, E_\nu^{\mathrm{vis}})$, we can construct the correction distributions $1/\varepsilon_{\mathrm{rec+trig}}$. These corrections are to be multiplied with the corresponding experimental data. As shown in Figures 3.8, the correction is essentially flat in x^{vis} around 1.9. For increasing E_ν^{vis} it increases from around 1.5 to 3.0, and for increasing z_l^{vis} it decreases from 3.4 to 1.0. All distributions are smooth and the dependences on these variables can be qualitatively understood in terms of hadronic energy leakage to the spectrometer—not taken into account on event basis—and by the H plane veto effect. These effects are taken care of by our acceptance corrections, leading to a rise with increasing E_ν^{vis} or decreasing z_l^{vis}.

The reconstruction and trigger acceptance corrections, as calculated, are not expected to significantly depend on details of the underlying model because of cancellations in the acceptance ratios. The model actually influences only the sampling distributions within each bin.

3.9   Background evaluation

For our final analysis the physics model of MCDIMUON accounts only for the opposite sign dimuon sample $(\mu^-\mu^+)$ in deep inelastic CC-interactions with charmed hadron production and decay. However, the real data sample is expected to include events from muonic decay of non-charm hadrons produced either directly or during shower development. As discussed in Section 1.5 the contribution of other background sources is expected to be negligible because of the relatively small cross-sections in combination with our kinematical selections. Thus the (non-charm) background level depends on the probability for a $\pi^\pm$ or $K^\pm$ to decay before it is absorbed in the calorimeter or first part of the muon spectrometer.

An important feature of the background is that the resulting same- and opposite-sign dimuon distributions are closely related. Our strategy is to use only the $\mu^-\mu^-$ events to estimate the background in our $\mu^-\mu^+$ data and not the $\mu^+\mu^+$ events, because the latter have a significant $\overline{\nu}_\mu$-induced component. Due to charge conservation opposite sign dimuon events occur with larger probability than same sign events. Moreover, not only the number of events but also their kinematics is slightly different. An elaborate MC background study is

therefore necessary to obtain our "best" background subtracted and acceptance corrected standard histogram distributions.

For this purpose a MC sample of same and opposite sign dimuon events from $\pi^{\pm}$ or $K^{\pm}$ decay is produced using the following method. About 85k CC events, of which most are single muon μ^{-} events, are generated with JETTA and processed through the EFICASS detector simulation. For each MC event all $\pi^{\pm}$ or $K^{\pm}$ mesons either produced at the primary vertex, or in the shower, are allowed to decay and produce a second muon with a probability dependent on the energy, the branching ratio to $\mu + \nu_{\mu}$, lifetime, mass and travel distance of the meson.

To reduce computer time, the $\pi^{\pm}$ or $K^{\pm}$ meson decay is not performed during the detector simulation, but afterwards and only muons produced with high probability and with momentum above 6 GeV/c are selected for further processing. At the level of our statistical accuracy this is expected to be fully representative. The thus generated dimuon events are subjected to the same kinematical and fiducial cuts as used in our dimuon analysis. Then our standard histograms are filled, each event weighted with the muonic decay probability. In total a MC sample of about 5k $\mu^{-}\mu^{-}$ and 4k $\mu^{-}\mu^{+}{}_{BG}$ events is obtained in this way. For each bin in the histograms we first calculate the ratios of $\mu^{-}\mu^{+}{}_{BG}/\mu^{-}\mu^{-}$ where the first muon comes (by definition) from the primary charged current interaction and the second muon from $\pi^{\pm}$ or $K^{\pm}$ decay. We expect as scale factor an overall ratio of around 1.3 from the CHARM II thesis work by Vincent Lemaître [39, 40]. We obtain for this factor the value 1.45 ± 0.05. The 10% difference between the CHARM II and our values is due to slightly different assumptions concerning acceptances and different showering in glass and lead. The background fraction of events is found to be (22.0±2.1)%.

From the standard distributions of real data $\mu^{-}\mu^{-}$ events and using the ratios $\mu^{-}\mu^{+}{}_{BG}/\mu^{-}\mu^{-}$ of each interval obtained above, we derive the number of background events from π,K-decay in the opposite sign dimuon sample. The projected dependence of the ratios $\mu^{-}\mu^{+}{}_{BG}/\mu^{-}\mu^{-}$ as function of our standard variables is shown in Figures 3.9. This ratio is flat around 1.4 in x^{vis}, it decreases from 1.9 to 1.3 for increasing E_{ν}^{vis}, and increases for increasing z_{l}^{vis} from 1.25 to 3.3. The energy of the μ^{+} is mostly higher than the energy of the μ^{-} like for the correspondingly charged parents π, K. This effect is complementary but smaller for the visible hadronic energy, which results in the shapes of the z_{l}^{vis} and E_{ν}^{vis} distributions.

At this point we can construct our background by bin-by-bin multiplication of the MC $\mu^{-}\mu^{+}{}_{BG}/\mu^{-}\mu^{-}$ distribution with the real data $\mu^{-}\mu^{-}$ distribution.
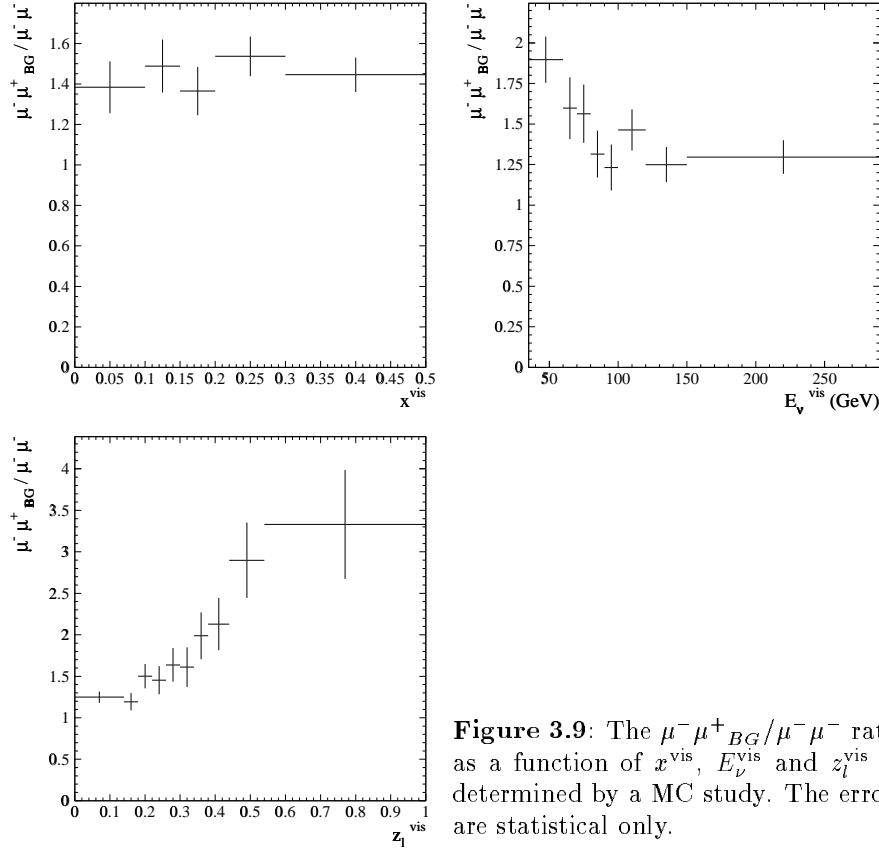
Figure 3.9: The $\mu^- \mu^+{}_{BG}/\mu^- \mu^-$ ratio as a function of x^{vis}, E_ν^{vis} and z_l^{vis} as determined by a MC study. The errors are statistical only.

To account for the effect of statistical fluctuations in the resulting background distributions, several alternatives are compared.

1) the histograms are left unchanged. The few bins with zero counts get assigned a statistical error ± 1, for other bins Gaussian errors are assumed.

2) partial rebinning: the histograms are smoothed in regions of lowest statistics, by averaging neighbouring bins. Using this method the one-dimensional histogram effectively reduces from 10 to 7 bins, and the two-dimensional histograms from 40 to 20 bins.

3) factorisation and partial rebinning: for the two dimensional $(x^{\mathrm{vis}}, E_\nu^{\mathrm{vis}})$ histogram the distributions in x^{vis} and E_ν^{vis} are assumed to be independent and thus factorisable. This factorisation is correct for the CC cross-section (Equation 1.20) to the extent that the logarithmic dependence of Q^2 on the nucleon scaling structure functions F_i can be neglected (scaling). Using the factorisation assumption the two-dimensional $(x^{\mathrm{vis}}, E_\nu^{\mathrm{vis}})$ histogram is recalculated using the two projected one-dimensional x^{vis} and E_ν^{vis} distributions. The z_l^{vis} histogram is partially rebinned, like in 2).

For each of the three alternatives the standard background distributions are made. After careful consideration we decided to use method 3) for our final fit analysis described in the next chapter and the two alternatives are used in our systematic error studies. We call this the "best" background estimate.

3.10 Discussion and summary

In the previous sections we described the analysis procedures to prepare our experimental data for the final part of the analysis. This final analysis and its result are presented in the next chapter. Before taking this last step it is worthwhile to look back and evaluate the procedures followed up to this point.

After the standard CHORUS calorimeter and muon spectrometer calibration the first step is to ensure that our dimuon events have well reconstructible muon tracks. This is handled by the SAMTRA and Super-SAMTRA reconstruction routines for accepted muons.

The next step, the vertex finding is done with a satisfactorily accurate method, the vertex location being determined within several centimeters (Figure 3.2). Given the muon momenta, the vertex position and the basic event information we derive for each event the values for many kinematical and other variables. Based on the average values per run of these variables, runs taken under unstable calorimeter conditions (mainly unidentified dead or hot channels) are removed. A rather large fraction (30%) of the recorded events is discarded

in this step. It may be possible that this fraction can be reduced somewhat by elaborate procedures and with carefully applied backward checks.

For accepted runs the individual events have been subjected to stringent tests and to first cuts. An important test is made by backtracking the two muons to the vertex and evaluating the distributions (Figure 3.3). Other selection criteria are applied to select the final sample.

For the final sample a comparison between the real data and a background estimate together with the MC programme JETTA is performed (Figures 3.4-3.7). It is concluded that they are in good overall agreement, within the statistical accuracy. The JETTA MC data are then used to calculate the reconstruction and trigger acceptances as well as the total acceptance correction (Figure 3.8). A major fraction of the reconstruction inefficiency is due to shower leakage into the spectrometer. The trigger inefficiency is significantly influenced by an undesirable H-veto effect.

Finally JETTA MC data are used to obtain our best estimate on the $\mu^-\mu^+$ background. Therefore the $\mu^-\mu^-$ data distributions are multiplied bin-by-bin by a distribution obtained by MC (Figure 3.9) to achieve the $\mu^-\mu^+{}_{BG}$ distributions.

In Figure 3.10 a comparison between real data and JETTA MC simulated opposite sign dimuon distributions for the standard histograms is given. The data points form the experimental distributions, where the errors are statistical only. The solid line represent the simulated distributions added to our best estimate for the background (dashed line), determined by multiplying the experimental $\mu^-\mu^-$ distributions with the corresponding $\mu^-\mu^+{}_{BG}/\mu^-\mu^-$ ratio distributions.
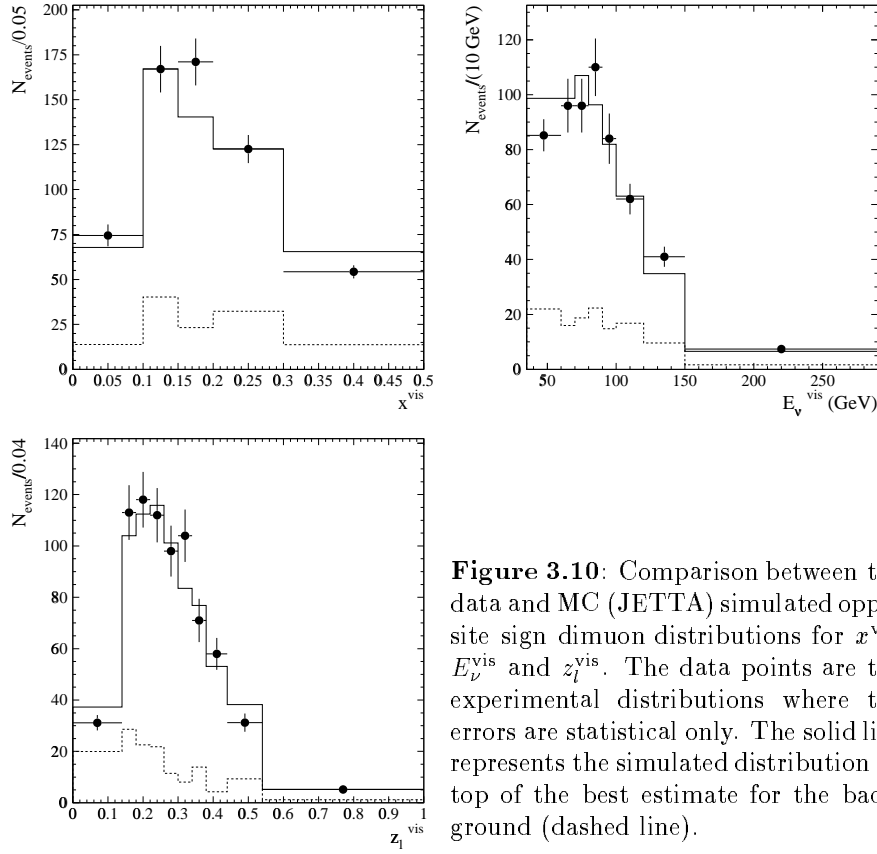
Figure 3.10: Comparison between the data and MC (JETTA) simulated opposite sign dimuon distributions for x^{vis}, E_ν^{vis} and z_l^{vis}. The data points are the experimental distributions where the errors are statistical only. The solid line represents the simulated distribution on top of the best estimate for the background (dashed line).

3. Data analysis

Chapter 4

Results

In this chapter the physics analysis in terms of the chosen dimuon model—with our standard histogram data as input—is described. After an introduction, the data fitting procedure is discussed. Then the resulting model parameters with their errors and quality of fit values are presented, and compared with earlier experiments. Finally an outlook is given on our expectation of the possible results using all available CHORUS dimuon calorimeter data.

4.1   Introduction

To extract the desired physics information from our experimental standard histogram data, we first have to subtract the background and to correct for various inefficiencies. The resulting data must be compared with simulated data from an adequate model with adjustable parameters. For this purpose we apply the "dimuon" model implemented in the Monte Carlo (MC) programme MCDI-MUON (Section 1.7.1). The model describes for an incoming muon neutrino the production, fragmentation and subsequent weak decay of a charm quark in terms of five free parameters. Two parameters, κ and α, concern the total content and the Bjorken-x distribution of strangeness in the nucleon. One parameter corresponds to the charm quark mass m_c. The formation of charmed hadrons is described by the Peterson *et al.* fragmentation function with one parameter ϵ_P. Finally the average muon branching ratio B_c takes care of the muonic decay of the produced charmed hadrons. The cross section is calculated according to the leading-order QCD helicity formalism for heavy quark production as discussed in Chapter 1.

For the values of the various parameters given in Table 1.4 and the results from the CHARM II analysis [39, 40], a MCDIMUON simulation for opposite sign dimuon events is made starting from GBEAM events. In this simulation cuts on the kinematical variables are issued, such that a reasonable fraction of events can be actually used in the fitting procedure. The events generated are reweighted with the dimuon cross-section in a fitting procedure. Thus the values of the fitted parameters are not the same as the ones used for the generation of the sample. This effect is investigated and found to be negligible. To determine the parameter values of the MCDIMUON model consistent with our data, standard histograms are made using the MC sample with statistics much higher than of the experimental data. These MC histograms are compared in terms of a χ^2 evaluation with the corresponding background subtracted experimental data, corrected for trigger and reconstruction inefficiencies. Only statistical errors are taken into account at this stage. By repeating the χ^2 evaluation for varying alternatives of the choice of parameter values, some insight is gained in the sensitivities. Our final result is based on a four parameter fit, and for this solution the systematic errors are estimated.

4.2   MCDIMUON data

MCDIMUON is based on a theoretical model with free parameters to extract information concerning charm production, fragmentation and decay. The antiquark distribution function, Equation 1.34, is taken directly from the CTEQ 3L [27] set, while the individual $\bar{u}$, $\bar{d}$, and $\bar{s}$ distribution functions are redefined using two additional parameters. The strange quark content (or magnitude) is connected to κ defined by Equation 1.35. The shapes of the strange and non-strange quark distributions are related through the shape parameter α. The strange sea is parameterised according to Equation 1.36, where its normalisation parameter A_s for given κ and α can be solved numerically (Equation 1.38). The mass of the charm quark, m_c, appears in the modified scaling variable χ of Equation 1.28 and thus in the cross section, given in Equation 1.30. The fragmentation parameter ϵ_P of the Peterson *et al.* distribution function (Equation 1.42), describes the charm quark hadronisation. The last parameter B_c, is the average muonic branching ratio of charmed hadrons (Equation 1.47). We assume here that B_c is not significantly dependent on the kinematical variables. This approximation is justified in view of our statistics. The neutrino cross section for the production of opposite-sign dimuons via charm production

at LO QCD is given by (Equation 1.48)

$$\frac{\mathrm{d}^3 \sigma^{\nu\,LO}}{\mathrm{d}x\mathrm{d}y\mathrm{d}z}(\nu\mathrm{N} \to \mu^-\mu^+\mathrm{X}) = \frac{\mathrm{d}^2 \sigma^{\nu\,LO}}{\mathrm{d}x\mathrm{d}y}(E_\nu, x, y, m_c, \kappa, \alpha)D_{H/c}^{\mathrm{Peterson}}(z, \epsilon_P)B_c,$$

$$(4.1)$$

as a function of E_ν, x, y, and z and dependent on the parameters m_c, κ, α, ϵ_P and B_c.

The total valence quark distribution function is a linear combination depending on Z and A of the u and d valence distribution functions of the proton assuming strong isospin symmetry. The x-distribution of the underlying u and d valence distributions is different when using a non-isoscalar target—as in our case—with $Z/A = 0.40$. Non-isoscalarity is assumed to have no effect for the sea quarks.

Each event is weighted with a factor depending on radiative effects at the primary vertex. This factor is determined for the inclusive charged current cross-section using the prescription of Bardin [31].

The cross section weighted (effective) number of MCDIMUON events and the number of real data events are normalised with respect to each other, on the basis of the number of "protons on target" from the SPS beam during data taking, and the number of muon-neutrinos per proton on target given by GBEAM.

The expected effective number of events in a two-dimensional interval (Δx^{vis}, $\Delta E_\nu^{\mathrm{vis}}$) follows from a convolution of the theoretical model and the neutrino beam spectrum:

$$N_{MC}\left(\Delta x^{\mathrm{vis}}, \Delta E_\nu^{\mathrm{vis}}\right) = N_{nucl}\int_{\Delta x^{\mathrm{vis}}} \mathrm{d}x^{\mathrm{vis}} \int_{\Delta E_\nu^{\mathrm{vis}}} \mathrm{d}E_\nu^{\mathrm{vis}} \int_\gamma \mathrm{d}\gamma$$

$$\int_{E_\nu} \mathrm{d}E_\nu \int_x \mathrm{d}x \int_y \mathrm{d}y \int_z \mathrm{d}z \frac{\mathrm{d}\Phi}{\mathrm{d}E_\nu}(E_\nu)$$

$$\frac{\mathrm{d}^3\sigma}{\mathrm{d}x\mathrm{d}y\mathrm{d}z}(E_\nu, x, y, z) \otimes P(\gamma, E_\nu, x, y, z, E_\nu^{\mathrm{vis}}, x^{\mathrm{vis}})$$

$$(4.2)$$

with

- N_{nucl}: the number of nucleons,

- $\mathrm{d}\Phi(E_\nu)/\mathrm{d}E_\nu$: the differential muon neutrino flux passing through the chosen fiducial volume of the calorimeter target as a function of the neutrino energy,

- $\mathrm{d}^3\sigma/(\mathrm{d}x\mathrm{d}y\mathrm{d}z)$: the dimuon cross section of nucleons (Equation 4.1),

- γ: a collection of instrumental and kinematic variables, like the directions of the muon tracks, the muon energies, the hadronic energy, the transverse position of the vertex, etc.

- $P(\gamma, E_\nu, x, y, z, E_\nu^{\text{vis}}, x^{\text{vis}})$: the probability that an event generated with the instrumental and kinematic variables (γ, E_ν, x, y, z) gives the visible variables $(E_\nu^{\text{vis}}, x^{\text{vis}})$. This probability also includes all cuts.

A similar model prediction for the number of events in a $(\Delta z_l^{\text{vis}})$ interval can be obtained by replacing $\int_{\Delta x^{\text{vis}}} \mathrm{d}x^{\text{vis}} \int_{\Delta E_\nu^{\text{vis}}} \mathrm{d}E_\nu^{\text{vis}}$ by $\int_{\Delta z_l^{\text{vis}}} \mathrm{d}z_l^{\text{vis}}$ and by replacing $P(\gamma, E_\nu, x, y, z, E_\nu^{\text{vis}}, x^{\text{vis}})$ by $P(\gamma, E_\nu, x, y, z, z_l^{\text{vis}})$ in Equation 4.2. All MCDIMUON events used in the fitting are undergoing the same cuts on the visible kinematic variables as the corresponding data sample.

4.3 Fitting procedure

During the MCDIMUON parameter adjustment the total valence quark, and the total anti-quark distribution functions (Equations 1.33 and 1.34) are kept fixed, while the distributions of the individual anti-quark flavours vary along with the two strangeness parameters κ and α. Also the values of m_c, ϵ_P, and B_c are adjusted. A best fit is obtained by minimising

$$\chi^2 = \sum_{\text{bins}} \frac{\left((N_d - N_b * f) * 1/\varepsilon_{\text{rec+trig}} - N_{MC}\right)^2}{\sigma_{d,b}^2 + \sigma_{MC}^2}, \tag{4.3}$$

where—after applying all cuts—N_d and N_b are the number of observed $\mu^-\mu^+$ and $\mu^-\mu^-$ events, f is the ratio $\mu^-\mu^+_{BG}/\mu^-\mu^-$, $1/\varepsilon_{\text{rec+trig}}$ is the reconstruction and trigger acceptance correction (Section 3.8) in each bin respectively. The quantity N_{MC} is the effective number of (weighted) dimuon events from charm production as generated by MCDIMUON

$$N_{MC} = \sum_{\text{events}} w_{MC}, \tag{4.4}$$

the sum running over the events in the bin, and where w_{MC} is the weight given according to the dimuon cross-section. The denominator contains the variances of the samples in each bin. In particular $\sigma_{MC}^2 = \sum_{\text{events}} w_{MC}^2$ concerns the statistical uncertainties on the MCDIMUON events and $\sigma_{d,b}$ on the observed number of events for $\mu^-\mu^+$ and $\mu^-\mu^-$ and on the ratio $\mu^-\mu^+_{BG}/\mu^-\mu^-$ and

$1/\varepsilon_{\text{rec+trig}}$. For given initial values of the parameters m_c, κ, α, ϵ_P and B_c a best fit is made by successively changing the parameters until the χ^2 reaches a minimum. During this iterative optimisation, for each step N_{MC} and σ_{MC} are modified by reweighting the MC events according to the parameter-dependent cross section. The Minuit function minimisation and error analysis package [120] is used to find the best-fit parameter values and the uncertainties including correlations. In total about 30k MC events are used to perform the fit. We note that for the χ^2 fitting procedure, instead of "correcting" the experimental data for reconstruction and trigger acceptance, we could equivalently have converted the MCDIMUON data to quasi-experimental data in which the acceptance is taken into account.

4.4 Five parameter fit

In Table 4.1 the results of a five parameter fit are given for our best background estimation method (Section 3.9). The contributions of the $(x^{\text{vis}}, E_\nu^{\text{vis}})$ and z_l^{vis} data points to the total χ^2 are 27.6 and 5.4, respectively. The total χ^2 is 32.9 and the number of degrees of freedom (ndf) is 45, corresponding to a χ^2 probability of 91%.

We have applied in fact the various background treatments of Section 3.9 for the $(x^{\text{vis}}, E_\nu^{\text{vis}})$ histogram in a series of studies, keeping the z_l^{vis} histogram unchanged. Assuming that the corresponding errors are uncorrelated, the effect of changing the background treatment is largest (1.2 σ) on α. On the value of

Table 4.1: Results of the five parameter dimuon cross section fit. Only statistical errors are considered. The correlation coefficients above the diagonal are omitted for brevity.

parameter	value	correlation coefficient					
		global	m_c	κ	α	B_c	ϵ_P
m_c (GeV/c^2)	$2.12 \, ^{+ \, 0.56}_{- \, 0.69}$	0.982	1				
κ	$0.99 \, ^{+ \, 0.59}_{- \, 0.50}$	0.978	-0.111	1			
α	$-6.0 \, ^{+ \, 3.7}_{- \, 4.3}$	0.968	-0.260	-0.708	1		
B_c (%)	$6.1 \, ^{+ \, 3.4}_{- \, 1.8}$	0.993	0.481	-0.879	0.637	1	
ϵ_P	$0.296 \, ^{+ \, 0.094}_{- \, 0.070}$	0.753	-0.496	-0.006	0.046	-0.160	1

ϵ_P the effect is negligible because this parameter is primarily dependent on the z_l^{vis} distribution. The effects on the other parameters are 0.04, 0.32 and 0.42 σ, for m_c, κ and B_c respectively. One can thus conclude that only the value of α depends significantly on details of the background estimation. Furthermore we notice that anyhow the sensitivity to α ($\approx -6 \pm 4$) is small. We must thus question at this point whether our present data set provides sufficient constraints to give information on the shape of the strangeness x-distribution. Moreover, large values of the correlation coefficients (Table 4.1) indicate that some of the parameters are too much correlated to be treated independently. Therefore we perform a series of 4-parameter fits as a function of α.

4.5 Four parameter fits

Nine fits for each background treatment are made with α in the range from -4 to 4. These values cover the one standard deviation region of the α parameter obtained by previous experiments [38–41]. They also include somewhat counter-intuitive negative values just for completeness.

In general, as shown in Figure 4.1 and Table 4.2, when α increases χ^2 increases. This is consistent with the five parameter fit, where the lowest χ^2 corresponds with an uncomfortably negative central value of α. The charm quark mass, m_c, and the fragmentation parameter, ϵ_P, are essentially stable.

Table 4.2: Results of the four parameter dimuon cross section fit for fixed values of α. The errors are statistical only. The numbers correspond to Figure 4.1.

| α	χ^2	m_c (GeV/c^2)	κ	B_c (%)	ϵ_P
-4	33.2	$2.12^{+0.57}_{-0.68}$	$0.79^{+0.42}_{-0.29}$	$7.1^{+2.7}_{-1.8}$	$0.292^{+0.091}_{-0.068}$
-3	33.6	$2.11^{+0.58}_{-0.69}$	$0.65^{+0.37}_{-0.25}$	$7.9^{+3.1}_{-2.1}$	$0.290^{+0.090}_{-0.068}$
-2	34.0	$2.10^{+0.59}_{-0.69}$	$0.51^{+0.29}_{-0.20}$	$9.0^{+3.5}_{-2.4}$	$0.288^{+0.090}_{-0.067}$
-1	34.6	$2.10^{+0.60}_{-0.70}$	$0.40^{+0.22}_{-0.15}$	$10.2^{+3.6}_{-2.5}$	$0.286^{+0.089}_{-0.067}$
0	35.2	$2.11^{+0.62}_{-0.71}$	$0.33^{+0.16}_{-0.11}$	$11.3^{+3.7}_{-2.6}$	$0.285^{+0.089}_{-0.067}$
1	36.0	$2.12^{+0.64}_{-0.72}$	$0.289^{+0.124}_{-0.095}$	$12.2^{+3.9}_{-2.6}$	$0.283^{+0.088}_{-0.066}$
2	36.9	$2.14^{+0.67}_{-0.74}$	$0.264^{+0.105}_{-0.085}$	$13.0^{+4.1}_{-2.7}$	$0.281^{+0.088}_{-0.066}$
3	37.8	$2.18^{+0.70}_{-0.77}$	$0.247^{+0.093}_{-0.079}$	$13.7^{+4.4}_{-2.8}$	$0.278^{+0.088}_{-0.066}$
4	38.8	$2.24^{+0.73}_{-0.80}$	$0.236^{+0.087}_{-0.077}$	$14.4^{+4.8}_{-3.0}$	$0.276^{+0.087}_{-0.065}$

Figure 4.1: The variation of χ^2, m_c, κ, B_c, and ϵ_P as a function of α. The errors are statistical only.

The strange quark magnitude following from κ is stable for $\alpha \geq 0$ while increasing for negative α, and the muon branching ratio B_c increases linearly with α. The values m_c, κ, ϵ_P and B_c are for fixed α all rather insensitive to

the background treatment, $< 0.25\ \sigma$, and smallest for values of $\alpha \approx 2$.

In summary, our studies in five parameter space indicate the following: 1) fix α at a "reasonable" value in the range where the other parameters are essentially stable, i.e. between -1 and 4, which also covers the range obtained by earlier experiments (see Table 4.7), and 2) apply the "best" background estimation, i.e. the one with factorisation treatment to suppress statistical fluctuations, which happens to give also the lowest χ^2 value.

4.6 Final fit
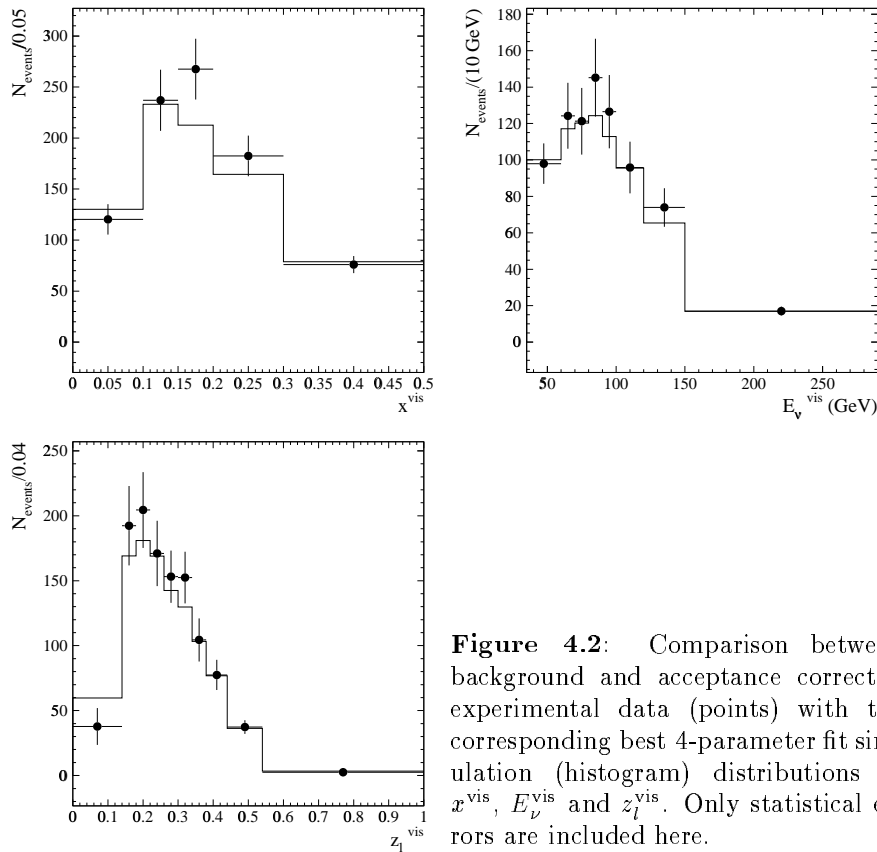
Figure 4.2: Comparison between background and acceptance corrected experimental data (points) with the corresponding best 4-parameter fit simulation (histogram) distributions of x^{vis}, E_ν^{vis} and z_l^{vis}. Only statistical errors are included here.

Table 4.3: The standard z_l^{vis} intervals (10 data points) with the corresponding numbers of events and correction factors as indicated for data, background and Monte Carlo. The deviation of each interval to the χ^2 of the final result is also listed, δ. The errors are statistical only.

z_l^{vis}	$N_{RD}^{\mu^-\mu^+}$	$N_{BG}^{\mu^-\mu^+}$	$N_{RD}^{\mu^-\mu^-}$	$\frac{\mu^-\mu^+_{BG}}{\mu^-\mu^-}$	$\frac{1}{\varepsilon_{rec+trig}}$	$\frac{N_{RD-BG}^{\mu^-\mu^+}}{\varepsilon_{rec+trig}}$	$N_{MC}^{\mu^-\mu^+}$	δ
0.00-0.14	109.0 ± 10.4	69.9 ± 10.1	56.00 ± 7.48	1.249 ± 0.067	3.386 ± 0.205	132 ± 50	208.9 ± 6.2	-1.53
0.14-0.18	113.0 ± 10.6	28.6 ± 6.4	24.00 ± 4.90	1.193 ± 0.105	2.280 ± 0.139	192 ± 31	169.2 ± 5.1	0.75
0.18-0.22	118.0 ± 10.9	22.5 ± 6.2	15.00 ± 3.87	1.501 ± 0.147	2.141 ± 0.120	204 ± 29	180.9 ± 5.2	0.79
0.22-0.26	112.0 ± 10.6	21.8 ± 6.2	15.00 ± 3.87	1.453 ± 0.169	1.896 ± 0.108	171 ± 25	169.0 ± 4.7	0.08
0.26-0.30	98.0 ± 9.9	9.8 ± 3.0	6.00 ± 1.73	1.625 ± 0.155	1.735 ± 0.102	153 ± 20	142.5 ± 4.3	0.52
0.30-0.34	104.0 ± 10.2	9.8 ± 3.0	6.00 ± 1.73	1.625 ± 0.155	1.617 ± 0.107	152 ± 20	129.8 ± 4.3	1.11
0.34-0.38	71.0 ± 8.4	8.2 ± 2.7	4.00 ± 1.26	2.058 ± 0.211	1.663 ± 0.120	104 ± 17	103.3 ± 3.5	0.06
0.38-0.44	87.0 ± 9.3	12.3 ± 4.1	6.00 ± 1.90	2.058 ± 0.211	1.556 ± 0.098	116 ± 17	115.3 ± 3.6	0.05
0.44-0.54	78.0 ± 8.8	6.6 ± 2.1	2.14 ± 0.62	3.080 ± 0.378	1.306 ± 0.082	93 ± 13	90.9 ± 3.0	0.17
0.54-1.00	59.0 ± 7.7	30.4 ± 9.5	9.86 ± 2.85	3.080 ± 0.378	1.030 ± 0.074	30 ± 13	39.7 ± 1.8	-0.79

Then, before performing the final 4-parameter fit we have to estimate the best value of the α-parameter. It is natural to do this on the basis of previous experimental results. Calculating the weighted average of the α values found in the CHARM II [39,40] and CCFR(LO) [41] analyses results in $\alpha = 2.22 \pm 0.58$, with a χ^2 of 0.91. The CDHS [38] value, $\alpha = 0$, is not included because the parameter was fixed (not determined by a fit). We prefer to fix the value of α on the weighted average, which is based on two considerably larger and more complete data sets than our own data, and subjected to essentially the same analysis. We perform a best fit for the values of m_c, κ, B_c and ϵ_P, using our best background estimate. The results are shown in Table 4.6. An overview of our standard histogram data as a function of z_l^{vis} and (x^{vis}, E_ν^{vis}) is given in Tables 4.3 and 4.4, including the δ_is, the contributions to the χ^2 of each interval. In Figure 4.2 the comparison between experimental and simulated projected distributions of x^{vis}, E_ν^{vis} and z_l^{vis} are shown. The contributions of the (x^{vis}, E_ν^{vis}) and z_l^{vis} data to the total χ^2 are 31.38 and 5.69, respectively. The total χ^2 is 37.07 and the number of degrees of freedom is 46 with a χ^2 probability of 82%. The value of $\chi^2/\mathrm{ndf} = 0.81$ suggests that the model provides an adequate description of the data, although we note that there is a strong correlation between B_c and m_c, and B_c and κ. The location of the found χ^2 minimum and its corresponding values of the free parameters is very stable against different starting values of the fit parameters.

Table 4.4: Same as Table 4.3 but for the $(x^{\text{vis}}, E_\nu^{\text{vis}})$ intervals (45 data points).

E_ν^{vis}	x^{vis}	$N_{RD}^{\mu^-\mu^+}$	$N_{BG}^{\mu^-\mu^+}$	$N_{RD}^{\mu^-\mu^-}$	$\frac{\mu^-\mu^+{}_{BG}}{\mu^-\mu^-}$	$\frac{1}{\varepsilon_{rec+trig}}$	$\frac{N_{RD-BG}^{\mu^-\mu^+}}{\varepsilon_{rec+trig}}$	$N_{MC}^{\mu^-\mu^+}$	δ
35- 60	0.00-0.10	13.0±3.6	7.3±2.4	4.03±1.22	1.80±0.22	1.41±0.26	8±6	14.5±1.1	-1.00
35- 60	0.10-0.15	37.0±6.1	10.6±3.2	5.44±1.52	1.94±0.23	1.45±0.14	38±11	41.4±1.6	-0.29
35- 60	0.15-0.20	48.0±6.9	6.1±2.1	3.42±1.08	1.78±0.21	1.37±0.13	57±11	43.5±1.5	1.22
35- 60	0.20-0.30	64.0±8.0	16.9±4.7	8.46±2.16	2.00±0.21	1.65±0.13	78±16	75.7±1.7	0.11
35- 60	0.30-0.50	51.0±7.1	14.4±4.0	7.65±1.99	1.89±0.19	1.74±0.12	64±15	75.2±1.3	-0.79
60- 70	0.00-0.10	13.0±3.6	2.1±0.9	1.39±0.55	1.52±0.23	1.71±0.32	19±7	12.9±1.2	0.78
60- 70	0.10-0.15	14.0±3.7	3.1±1.2	1.88±0.71	1.64±0.25	1.68±0.26	18±7	20.5±1.4	-0.29
60- 70	0.15-0.20	27.0±5.2	1.8±0.8	1.18±0.48	1.50±0.23	1.53±0.24	39±10	21.4±1.5	1.71
60- 70	0.20-0.30	21.0±4.6	4.9±1.9	2.92±1.05	1.69±0.24	1.54±0.19	25±8	32.0±1.4	-0.87
60- 70	0.30-0.50	21.0±4.6	4.2±1.6	2.64±0.96	1.59±0.22	1.42±0.17	24±7	30.4±1.0	-0.86
70- 80	0.00-0.10	12.0±3.5	2.5±1.0	1.67±0.62	1.49±0.22	1.41±0.22	13±5	19.0±1.6	-0.98
70- 80	0.10-0.15	18.0±4.2	3.6±1.4	2.25±0.80	1.60±0.24	1.68±0.27	24±8	21.2±1.6	0.35
70- 80	0.15-0.20	24.0±4.9	2.1±0.9	1.42±0.55	1.47±0.22	1.72±0.29	38±11	19.4±1.3	1.72
70- 80	0.20-0.30	24.0±4.9	5.8±2.1	3.50±1.18	1.65±0.22	1.53±0.18	28±9	30.5±1.5	-0.29
70- 80	0.30-0.50	18.0±4.2	4.9±1.8	3.17±1.08	1.55±0.21	1.37±0.15	18±7	30.0±1.1	-1.80
80- 90	0.00-0.10	23.0±4.8	3.0±1.1	2.36±0.80	1.25±0.18	1.17±0.20	23±7	25.0±2.0	-0.22
80- 90	0.10-0.15	20.0±4.5	4.3±1.5	3.19±1.02	1.35±0.19	1.77±0.29	28±9	21.3±1.7	0.68
80- 90	0.15-0.20	17.0±4.1	2.5±0.9	2.01±0.71	1.23±0.18	1.83±0.35	27±9	19.9±1.5	0.72
80- 90	0.20-0.30	25.0±5.0	6.9±2.2	4.96±1.48	1.39±0.18	1.86±0.25	34±11	30.3±1.6	0.29
80- 90	0.30-0.50	25.0±5.0	5.9±1.9	4.49±1.36	1.31±0.17	1.76±0.22	34±10	27.8±1.1	0.57
90-100	0.00-0.10	22.0±4.7	1.9±0.8	1.67±0.62	1.17±0.18	2.17±0.38	43±13	23.8±2.1	1.52
90-100	0.10-0.15	15.0±3.9	2.8±1.1	2.25±0.80	1.26±0.19	1.48±0.24	18±7	20.5±1.8	-0.37
90-100	0.15-0.20	10.0±3.2	1.6±0.7	1.42±0.55	1.16±0.17	1.65±0.28	14±6	16.6±1.5	-0.46
90-100	0.20-0.30	14.0±3.7	4.6±1.7	3.50±1.18	1.30±0.18	1.76±0.26	17±8	28.2±1.6	-1.50
90-100	0.30-0.50	23.0±4.8	3.9±1.4	3.17±1.08	1.22±0.16	1.81±0.25	35±10	23.8±1.1	1.05
100-120	0.00-0.10	22.0±4.7	4.5±1.5	3.19±1.01	1.39±0.18	2.36±0.31	41±13	46.2±3.3	-0.37
100-120	0.10-0.15	28.0±5.3	6.5±2.1	4.31±1.28	1.50±0.19	1.87±0.27	40±12	31.6±2.4	0.70
100-120	0.15-0.20	16.0±4.0	3.7±1.3	2.72±0.90	1.37±0.17	2.44±0.39	30±11	28.0±2.0	0.17
100-120	0.20-0.30	32.0±5.7	10.4±3.1	6.71±1.83	1.55±0.17	2.19±0.27	47±15	43.0±2.1	0.29
100-120	0.30-0.50	26.0±5.1	8.8±2.6	6.07±1.68	1.45±0.16	1.91±0.20	33±11	42.2±1.6	-0.82
120-150	0.00-0.10	27.0±5.2	3.8±1.3	3.19±1.01	1.19±0.16	1.94±0.25	45±12	50.5±3.8	-0.45
120-150	0.10-0.15	20.0±4.5	5.5±1.8	4.31±1.28	1.28±0.16	2.76±0.46	40±15	35.7±2.9	0.29
120-150	0.15-0.20	17.0±4.1	3.2±1.1	2.72±0.90	1.17±0.15	2.46±0.40	34±12	27.8±2.3	0.52
120-150	0.20-0.30	29.0±5.4	8.9±2.6	6.71±1.83	1.32±0.15	2.63±0.36	53±17	41.6±2.3	0.65
120-150	0.30-0.50	30.0±5.5	7.5±2.2	6.07±1.68	1.24±0.14	2.21±0.27	50±14	40.6±1.7	0.63
150-290	0.00-0.10	17.0±4.1	3.1±1.1	2.50±0.84	1.23±0.16	3.40±0.39	47±16	68.5±5.6	-1.28
150-290	0.10-0.15	15.0±3.9	4.5±1.5	3.38±1.06	1.33±0.16	2.85±0.41	30±13	40.8±3.8	-0.83
150-290	0.15-0.20	12.0±3.5	2.6±1.0	2.13±0.74	1.22±0.15	3.11±0.61	29±13	36.1±3.1	-0.53
150-290	0.20-0.30	36.0±6.0	7.2±2.2	5.25±1.54	1.37±0.15	2.92±0.38	84±22	47.2±3.0	1.68
150-290	0.30-0.50	23.0±4.8	6.1±1.9	4.75±1.42	1.29±0.13	2.84±0.36	48±16	44.7±2.1	0.20

Systematic errors and discussion

Before considering the precision of our final result, we note that there are two levels of systematic uncertainties. On the first level, the physics interpretation and general application of the obtained fit values in a "complete" (QCD-based) description is restricted by the intrinsic simplifications of our dimuon model. However by comparing our results with results from other experiments obtained with the same model in essentially the same way, we ignore these intrinsic model uncertainties at this point and aim at a direct check between outcomes of different experiments. For this reason we have as closely as possible followed the LO analysis of the CHARM II [39,40], CCFR [41], and CDHS [38] experiments. The significance of our work thus mainly concerns a comparison and consistency check with these latter experiments.

On the second level, within the context of the common dimuon model, to obtain estimates for the systematic uncertainties of the final parameter values we perform several studies. Statistical errors strongly dominate the overall precision. The depth of our systematic studies is balanced accordingly. The systematic uncertainties form two groups:

1) Fixed input parameters with known standard deviations.

The systematic error is determined by independent fits for values plus and minus one standard deviation away from the fixed position. For simplicity the total systematic error is then symmetrised by quadratic averaging $\sqrt{(\delta_{k-}^2 + \delta_{k+}^2)/2}$.

2) Fixed input parameter values based on assumptions.

The systematic error is determined by independent fits for values based on different assumptions. We calculate for each assumption an error component δ_i, and their root-mean-square is calculated for each fit parameter using the formula $\sqrt{(\sum_{i=1}^{n} \delta_i^2)/n}$, where i runs over the different assumptions.

Following the list in Table 4.5 the systematic uncertainties are obtained in the following way:

- The fixing of $\alpha = 2.22 \pm 0.58$ and $\beta = 1.7 \pm 1.5$ $(GeV/c)^{-2}$ (Equation 1.45), the shapes of the strangeness and the the p_t distribution, respectively. The central value of β is determined by averaging the values used by E531 [58], CDHS [38] and CCFR [41], and its error covers the entire range.

- We use the 1996 Particle Data Group (PDG) values [121] $|V_{cd}| = 0.221 \pm 0.002$ and $|V_{cs}| = 0.9743 \pm 0.0004$, where the errors are correlated due to the unitarity constraint on the Cabibbo-Kobayashi-Maskawa (CKM)

matrix [23, 24]. The values are not significantly changed between the values used and the latest PDG values [52]. By varying these CKM matrix elements in the dimuon cross-section of Equation 1.30 only the relative weight of scattering on d or s quarks changes, and as the relative error on $|V_{cd}|$ is about 20 times larger than the one on $|V_{cs}|$, only the uncertainty on $|V_{cd}|$ is considered.

- To calculate the uncertainty due to the D decay to $K + \mu + \nu$, $K^* + \mu + \nu$, and $\pi + \mu + \nu$, we assume, as mentioned in Section 1.7.1, that the relative branching ratios are 0.60 ± 0.03, 0.33 ± 0.03, and 0.07 ± 0.02 respectively. The uncertainty of the last decay can be neglected. The effect on the uncertainty on the relative branching ratios is about a factor of 2 larger for the decay to K^* than to K; only the uncertainty in the K^* decay is considered. The uncertainties due to the relative branching ratios of the Λ_c decay are expected to be negligible, because only 7% of the charm quarks fragments into a Λ_c, and only 4.5% of the Λ_c decay into a muon (see Table 1.4).

- To judge the uncertainty due to the quark distribution functions and the charm fragmentation function, we utilise the GRV 94 LO [28] quark distributions, and the Collins-Spiller fragmentation function [47] in two independent fits. It has to be noted that the uncertainty in the fragmentation parameter ϵ_P can not be determined in a straightforward way, as the fragmentation parameter of the Collins-Spiller fragmentation function is defined in a different way.

- The overall uncertainty of 5.2% in the neutrino flux normalisation is mostly due to the estimated error on the number of protons on target from the beam-current transformers. Our uncertainty estimate concerning the neutrino beam (total flux and energy distribution) is based on a conservative intuitive estimate, comparing results from different GBEAM versions.

- The uncertainty in the energy scale of the calorimeter is estimated by the following method. The calorimeter scintillation signal is parametrised according to $S = \alpha_c \times P(\text{GeV}/c) + \beta_c$, with two parameters α_c and β_c [88]. For electrons these parameters have the values $\alpha_c = 17.2 \pm 0.3$, $\beta_c = -0.14 \pm 0.96$, while for pions they are $\alpha_c = 15.3 \pm 0.2$, $\beta_c = -5.8 \pm 1.0$. In our analysis we use the values $\alpha_c = 16.6 \pm 1.0$ and $\beta_c = -5.1 \pm 5.0$, and the uncertainties in these parameters, assumed to be uncorrelated, are

106

quadratically added to estimate the calorimeter energy scale uncertainty. The value of $\beta_c = -5.1$ corresponds to an offset of -307 MeV hadronic energy. The uncertainty in the momentum scale of the spectrometer is assumed to be 2%.

- The uncertainty in the trigger efficiency is evaluated assuming a 10% error on the trigger inefficiency calculated for each interval of the distribution.

- The systematic error due to the uncertainty in the reconstruction efficiency correction is evaluated by splitting this efficiency into a smearing and a real reconstruction efficiency, resulting in $\varepsilon_{\text{rec+smear}} = 0.707\pm0.008$, $\varepsilon_{\text{smear}} = 1.195 \pm 0.008$ and $\varepsilon_{\text{rec}} = 0.592 \pm 0.007$, respectively, where the errors are statistical only. The uncertainty in the values of the fitted parameters due to ε_{rec} is evaluated by assuming a 10% error on the bin-by-bin reconstruction inefficiency.

- To estimate the uncertainty due to the shape of the background distribution, the partial rebinning method is applied (Section 3.9). Only the shape of the background distribution is estimated, because the total background is normalised using the number of real data $\mu^-\mu^-$ events. The systematic error due to the statistical uncertainty in the background normalisation is estimated from the $\mu^-\mu^-$ sample with 144 ± 12 events.

In Table 4.5 the systematic errors considered are given. Different components of the same error have been added in quadrature. The most significant error components for m_c arise from the uncertainties in the relative D-meson branching ratio to K and K*, and the quark distribution functions. For κ they reflect the uncertainty in the muon energy calibration of the spectrometer and the shape of the p_t distribution of charmed hadrons with respect to the W-boson direction. For B_c the systematic error mainly stems from the uncertainties in the neutrino flux distribution, the spectrometer calibration and the already mentioned relative D-meson branching ratios. Also for ϵ_P the uncertainties in the neutrino flux distribution and the relative D branching ratios predominate.

The influence of uncertainty in the relative D branching ratios can be understood in terms of a change in the energy distributions—in particular the average values—of the secondary muon, the hadron shower and the neutrino from charm decay. For example the fragmentation variable z_l^{vis} depends on the energy of the second muon and the hadronic energy, so its distribution is effected.

Table 4.5: Systematic errors.

Error source	Δm_c	$\Delta \kappa$	ΔB_c (%)	$\Delta \epsilon_P$
α (xs distribution)	0.02	0.011	0.4	0.001
β (p_t distribution)	0.16	0.029	0.4	0.029
$|V_{cd}|$ and $|V_{cs}|$	0.00	0.006	0.2	0.001
D decay K* versus K	0.41	0.009	1.1	0.052
Quark distribution function	0.21	0.003	1.1	0.010
Fragmentation	0.12	0.002	0.2	
Neutrino flux normalisation	0.00	0.000	0.7	0.000
Neutrino beam	0.07	0.005	1.7	0.040
Energy scale calorimeter	0.18	0.020	0.9	0.016
Momentum scale spectrometer	0.15	0.040	1.1	0.016
Trigger efficiency	0.11	0.007	0.8	0.005
Reconstruction efficiency	0.01	0.008	0.8	0.014
Background shape	0.01	0.010	0.2	0.013
Background normalisation	0.01	0.005	0.3	0.004
Total	0.57	0.058	3.1	0.079

D stands for D$^\pm$, D^0, $\overline{\mathrm{D}}^0$ and D$_\mathrm{s}^\pm$.

Table 4.6: The result of our final 4-parameter fit for a fixed value of $\alpha = 2.22$. The first error is statistical and the last systematical, the correlation coefficients are statistical only.

parameter	value	stat	syst	correlation coefficient				
				global	m_c	κ	B_c	ϵ_P
α	2.22	(fixed)						
m_c (GeV/c^2)	2.15	$^{+0.67}_{-0.75}$	± 0.57	0.947	1			
κ	0.260	$^{+0.101}_{-0.083}$	± 0.058	0.917	-0.058	1		
B_c (%)	13.1	$^{+4.1}_{-2.7}$	± 3.1	0.968	0.715	-0.664	1	
ϵ_P	0.280	$^{+0.088}_{-0.066}$	± 0.079	0.675	-0.261	-0.235	0.150	1

Nuclear effects on the deep inelastic nucleon cross section (see Section 1.2) are not taken into account in the fitting procedure. It is difficult to implement these effects consistently. We estimate the systematic uncertainty due to nuclear effects by using the following phenomenological method. The nuclear structure function ratio $F_2^{\mathrm{Pb}}/F_2^{\mathrm{D}}$ is obtained by multiplying the ratios $F_2^{\mathrm{Pb}}/F_2^{\mathrm{C}}$ and $F_2^{\mathrm{C}}/F_2^{\mathrm{D}}$ taken from NMC analyses [116, 117], and then using the parametrisation $F_2^{\mathrm{Pb}}/F_2^{\mathrm{D}} = x^{m_1}(1 + m_2)(1 - m_3 x)$ proposed by Smirnov [122]. The values found in a fit are $m_1 = 0.128 \pm 0.015$, $m_2 = 0.50 \pm 0.07$ and $m_3 = 0.76 \pm 0.08$ with a $\chi^2/\mathrm{ndf} = 4.3/12$. We attribute the deviation from unity entirely to intrinsic effects of the target nucleus, as opposed to propagator effects. Therefore the x-dependence should also be valid for neutrino scattering. Neglecting in this ratio any dependence on Q^2, it is simply assumed that all parton distribution functions have the same nuclear dependence. By applying the nuclear modification of the parton distributions, the deviations from the central values are $\Delta m_c = +0.06$ GeV$/c^2$, $\Delta \kappa = -0.074$, $\Delta B_c = +1.4\%$ and $\Delta \epsilon_P = +0.001$. By applying the modification to the dimuon cross-section the differences are the same. Only the effects on B_c and κ are significant with respect to the uncertainties. The systematic errors for our four parameters are shown in Table 4.6.

4.7 Comparison with other experiments

A comparison of our results with those from CDHS [38], CCFR [41] and CHARM II [39, 40], is shown in Table 4.7. All results are based on a similar leading-order QCD formalism. We observe that the parameter values determined in our analysis are compatible with those of the other experiments within the errors, except ϵ_P, or $\langle z \rangle$. Our value of ϵ_P is only compatible with the value found by CCFR. There are two main differences on data and analysis between the earlier experiments and ours:

1) the earlier data are based on neutrino as well as anti-neutrino interactions, while we only have neutrino induced events. For deep inelastic neutrino induced charged current charm production about 50% is due to interactions with strange quarks, while for anti-neutrino interactions strangeness accounts for about 90%. Thus the anti-neutrino data are more sensitive to the strangeness parameters κ and α;

2) the earlier experiments have their MC sample normalised to the real data sample in terms of the number of equivalently detected and generated inclusive charged current events. This minimises the uncertainty on B_c due to uncertain-

4. Results

Table 4.7: Comparison of neutrino dimuon results using leading-order QCD analyses from CDHS [38], CCFR(LO) [41], CHARM II [39,40], and our analysis. Statistical and systematic errors are added in quadrature, except for the error on ϵ_P from CCFR which is statistical only. For CHARM II, CCFR and our analysis the quantity $\langle z \rangle$ is calculated from the Peterson *et al.* fragmentation function [46] using the fitted value of ϵ_P. For CDHS, the range for ϵ_P is obtained from the determination of $\langle z \rangle$. Numbers in parentheses are derived from fitted parameters.

	CDHS	CCFR(LO)	CHARM II	Our analysis
		c quark production		
m_c (GeV/c^2)	1.50 (fixed)	1.31 ± 0.24	1.79 ± 0.38	2.15 ± 0.91
κ	0.48 ± 0.08^a	0.373 ± 0.048	0.388 ± 0.095	0.26 ± 0.11
α	0 (fixed)	2.50 ± 0.65	1.12 ± 1.29	2.22 (fixed)
		c quark fragmentation		
ϵ_P	([0.02,0.14])	0.20 ± 0.04	0.072 ± 0.017	0.28 ± 0.11
$\langle z \rangle$	0.68 ± 0.08	(0.56 ± 0.02)	(0.66 ± 0.02)	(0.53 ± 0.04)
		charmed hadron decay		
B_c (%)	8.4 ± 1.5^a	10.5 ± 0.9	9.05 ± 0.98	13.1 ± 4.7

^{a}Corrected for the PDG98 [52] values of V_{cd} and V_{cs}.

ties in the neutrino flux. In our experiment we normalise the MC to the real data sample by using the neutrino-nucleon dimuon cross-section, the GBEAM neutrino flux and the number of nucleons in the target. The earlier experiments are more sensitive to the charm production cross section with respect to the total CC cross section, while in our analysis we are more sensitive to the charm production cross-section itself. For comparable uncertainties in B_c, the combined relative error on our neutrino flux measurement and number of target nucleons must be the same as the relative error on the total CC cross-section including the CC detection efficiency for the earlier experiments. From Table 1.1 B_c should have a value between 4% and 17% and the obtained value of 13% is thus quite reasonable.

In Figure 4.3 the strange quark distribution $xs(x, Q^2)$ and the down quark sea distribution $xd_{\text{sea}}(x, Q^2)$, both at $Q^2 = 20 \text{ GeV}^2/c^2$, obtained in CHARM II [39,40] and in our analysis are compared to the CTEQ 3L [27] distributions. The results of the two analyses are consistent, but the strange quark distribution obtained in our analysis has a wider error band. This is primarily due to the 1.4 times larger error on κ, related to our smaller number of events.

110
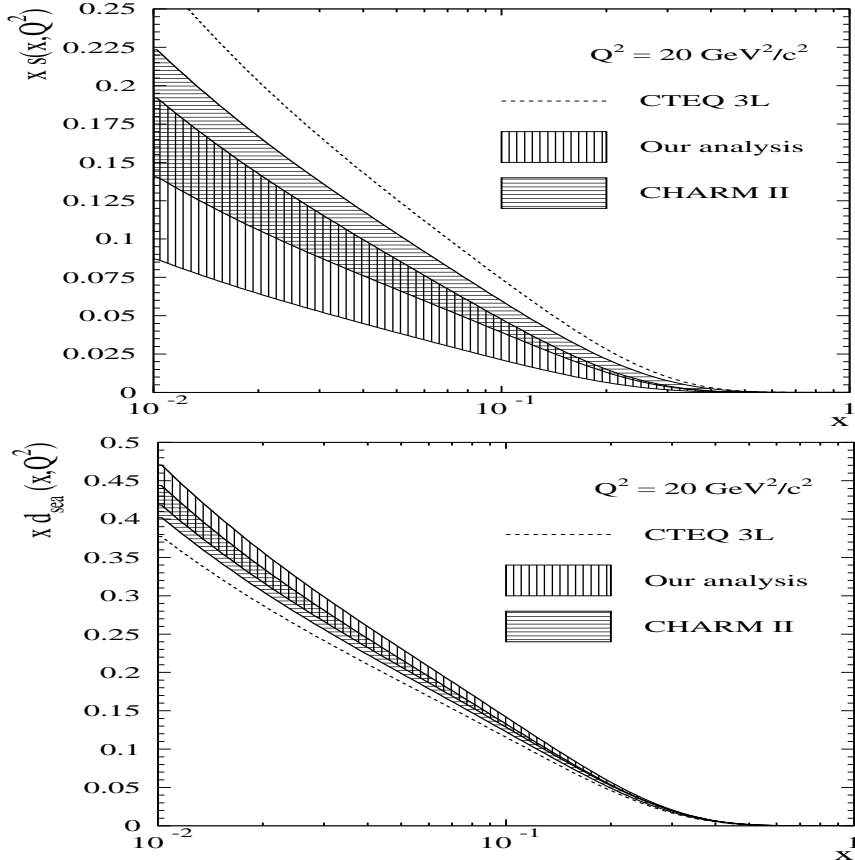
Figure 4.3: The strangeness distribution $xs(x, Q^2)$ (top) and the down quark sea distribution $xd_{\mathrm{sea}}(x, Q^2)$ (bottom) both at $Q^2 = 20$ GeV$^2/c^2$, from CHARM II data [39, 40], CTEQ 3L [27] and our analysis. The hatched areas indicate the $\pm 1\sigma$ statistical and systematical uncertainty added in quadrature. The κ and α contributions to these uncertainties are assumed to be uncorrelated.

For both experiments the analysis was performed with the total anti-quark distribution function $x\bar{q}(x, Q^2) = xs(x, Q^2) + 2xd_{\mathrm{sea}}(x, Q^2)$ taken from CTEQ 3L. The differences between the CTEQ 3L distributions on the one hand, and those from CHARM II and our analysis on the other can be attributed to the CTEQ 3L assumptions that the shape of the strange and non-strange sea are kept the same ($\alpha = 0$), and that $\kappa = 1/2$ at $Q^2 = 2.56$ GeV$^2/c^2$. This latter

111

value corresponds to $\kappa = 0.593$ at 20 GeV$^2/c^2$, where our and the CHARM II analysis are made.

Notwithstanding the fit stability and a good description of our data by the LO formalism, the QCD interpretation of m_c and κ requires caution. A recent—though incomplete—next-to-leading-order analysis [42] of dimuon data performed by the CCFR collaboration (see also Table 1.3) shows that these parameters may be sensitive to a gluon fusion contribution, particularly near the reaction threshold.

4.8   Outlook

In our analysis only the 1995 CHORUS calorimeter data are used. When all the data available from 1994 through 1998 would be analysed in the same way the data sample would be 5 times larger. If all data are considered we have about 5k $\mu^-\mu^+$ events, using the same cuts. In 1998 an additional running period without emulsions was granted to CHORUS. In this period a substantial increase of the data sample of CC neutrino-calorimeter interactions was acquired. In the same period also data with the anti-neutrino beam were taken, amounting to 3% of the total neutrino sample. The calorimeter triggers were improved. In particular, the minimum bias trigger only included a hit in one of the calorimeter scintillator planes, the trigger H-plane veto was removed, the fiducial volume of the charged current trigger was increased. By using these data the efficiency of the calorimeter two track triggers of the previous years can be estimated. Not only the total two-track trigger efficiency, but also the dependence on the fiducial volume, the dependence on the H-plane veto, as well as the dependence on the timing problems of the two-track trigger signal from the first two spectrometer magnets can be measured. By using an improved spectrometer track finding algorithm it is expected that the number of events increases with about 12%, and thus that the efficiency correction decreases accordingly. In the present work about 30% of the triggers is not included in the analysis, especially due to calorimeter instabilities. This loss of triggers can be reduced by half by more detailed study. Taking care of energy leakage into the spectrometer for individual events, and using calorimeter streamer tube information to "extrapolate" the muon tracks to find the vertex will improve the reconstruction efficiency and minimise smearing. By detailed studies of the sensitivity to various cuts, most probably less stringent selections can be made. Using all these improvements we expect that the number of events used for dimuon analysis can be enlarged by a factor two. The larger statistics of

the sample will allow to represent the data in more dimensions and in smaller intervals. Detailed studies may then allow the data to be better understood, and to reduce the systematic errors.

The efficiency of—and the uncertainties in—the event reconstruction also can be improved; examples are the calorimeter shower development and resolution, the muon energy deposition in the calorimeter and the vetoing of out-of-time muons.

It would be worthwhile to develop a Monte Carlo programme which can be used for detector smearing and acceptance evaluations as well as fitting. A fast detector simulation is needed for that.

An experimental study of the neutrino beam is at present being performed [63, 123]. This knowledge will reduce the uncertainty on the neutrino flux and its energy distribution. To minimise the error due to the neutrino flux normalisation it is recommended to normalise the dimuon Monte Carlo sample by using the number of generated and detected charged current events, instead of the method applied in our analysis. A further study of the background from π,K-decay using real $\mu^-\mu^-$ data, and an improved Monte Carlo generator of this background can improve our knowledge on the background and thus the systematic effect it has on the results. This becomes of increasing importance for a data set with higher statistics.

Improved knowledge of F_2 and xF_3 for our lead calorimeter target (this analysis is being performed in CHORUS [124]) can be used to determine the non-singlet and singlet quark distributions and the gluon distribution including nuclear effects. Using the obtained quark and gluon distributions one can determine [125] the quark flavour distributions. The systematic error due to nuclear effects (one of the largest systematic error estimates in our analysis) can be reduced.

In conclusion, in our analysis the statistical and systematic errors are at about the same level for all fitted parameters. The former can be reduced by using all available CHORUS data, and the latter by studying and improving the effects discussed above. In principle, the number of neutrino induced events can then be twice as large as in the analysis performed by the CCFR collaboration [41, 42], but the number of anti-neutrino events will be negligible compared to the CCFR sample. Nevertheless, a competitive charm production analysis using all the CHORUS data seems within reach. The value of B_c can be determined independently in the emulsion analysis from CHORUS. We expect that a full NLO analysis can be performed. All these improvements will enhance our knowledge of the strange quark sea, the charm quark mass, the charm quark fragmentation and the decay of charmed hadrons into a muon.

4. Results

References

[1] E. Eskut *et al.*, CHORUS *coll.*, "The CHORUS experiment to search for $\nu_\mu \to \nu_\tau$ oscillation", *Nucl. Instrum. Meth.* **A401** (1997) 7–44.

[2] W.K.H. Panofsky, "Low q^2 electrodynamics, elastic and inelastic electron (and muon) scattering", In *14th International Conference on High-Energy Physics*, 23–39, 1968, Vienna, Austria.

[3] M. Gell-Mann, "A Schematic Model of Baryons and Mesons", *Phys. Lett.* **8** (1964) 214–215.

[4] G. Zweig, "An SU$_3$ Model for Strong Interaction Symmetry and Its Breaking", CERN Preprint 8182/TH.401, CERN, January 1964.

[5] G. Zweig, "An SU$_3$ Model for Strong Interaction Symmetry and Its Breaking II", CERN Preprint 8419/TH.412, CERN, February 1964.

[6] R.P. Feynman, "Very high-energy collisions of hadrons", *Phys. Rev. Lett.* **23** (1969) 1415–1417.

[7] E.D. Bloom *et al.*, "High-energy inelastic e-p scattering at 6° and 10°", *Phys. Rev. Lett.* **23** (1969) 930–934.

[8] M. Breidenbach *et al.*, "Observed behavior of highly inelastic electron-proton scattering", *Phys. Rev. Lett.* **23** (1969) 935–939.

[9] J.J. Aubert *et al.*, "Experimental Observation of a Heavy Particle J", *Phys. Rev. Lett.* **33** (1974) 1404–1406.

[10] J.-E. Augustin *et al.*, "Discovery of a Narrow Resonance in e$^+$ e$^-$ Annihilation", *Phys. Rev. Lett.* **33** (1974) 1406–1408.

References

[11] S.W. Herb *et al.*, "Observation of a Dimuon Resonance at 9.5 GeV in 400-GeV Proton-Nucleus Collisions", *Phys. Rev. Lett.* **39** (1977) 252–255.

[12] W.R. Innes *et al.*, "Observation of Structure in the Υ(1S) Region", *Phys. Rev. Lett.* **39** (1977) 1240–1242.

[13] M.L. Perl *et al.*, "Evidence for Anomalous Lepton Production in e^+-e^- Annihilation", *Phys. Rev. Lett.* **35** (1975) 1489–1492.

[14] S.L. Glashow, "Partial-symmetries of weak interactions", *Nucl. Phys.* **22** (1961) 579–588.

[15] S. Weinberg, "A model of leptons", *Phys. Rev. Lett.* **19** (1967) 1264–1266.

[16] A. Salam, "Elementary Particle Theory: Relativistic groups and analycity", In *Proc. Eighth Nobel Symposium Aspenäsgården*, 367–377, 1968, Lerum, Sweden.

[17] V.N. Gribov and L.N. Lipatov, "Deep inelastic ep scattering in perturbation theory", *Sov. J. of Nucl. Phys.* **15** (1972) 438–450.

[18] V.N. Gribov and L.N. Lipatov, "e^+e^--Pair Annihilation and Deep Inelastic ep Scattering in Perturbation Theory", *Sov. J. of Nucl. Phys.* **15** (1972) 675–684.

[19] L.N. Lipatov, "The parton model and perturbation theory", *Sov. J. of Nucl. Phys.* **20** (1975) 94–102.

[20] Yu.L. Dokshitzer, "Calculation of structure functions of deep-inelastic scattering and e^+e^- annihilation by perturbation theory in quantum chromodynamics", *Soviet Physics JTEP* **46** (1977) 641–653.

[21] G. Altarelli and G. Parisi, "Asymptotic freedom in parton language", *Nucl. Phys.* **B126** (1977) 298–318.

[22] J.D. Bjorken, "Asymptotic Sum Rules at Infinite Momentum", *Phys. Rev.* **179** (1969) 1547–1553.

[23] M. Kobayashi and T. Maskawa, "CP-Violation in the Renormalizable Theory of Weak Interaction", *Prog. Theor. Phys.* **49** (1973) 652–657.

[24] N. Cabibbo, "Unitary symmetry and leptonic decays", *Phys. Rev. Lett.* **10** (1963) 531–533.

116

[25] M.A.G. Aivazis *et al.*, "Leptoproduction of heavy quarks. I. General formalism and kinematics of charged current and neutral current production processes", *Phys. Rev.* **D50** (1994) 3085–3101.

[26] M.A.G. Aivazis *et al.*, "Leptoproduction of heavy quarks. II. A unified QCD formulation of charged and neutral current processes from fixed-target to collider energies", *Phys. Rev.* **D50** (1994) 3102–3118.

[27] H.L. Lai *et al.*, CTEQ *coll.*, "Global QCD analysis and the CTEQ parton distributions", *Phys. Rev.* **D51** (1995) 4763–4782.

[28] M. Glück, E. Reya and A. Vogt, "Dynamical parton distributions of the proton and small-x physics", *Z. Phys.* **C67** (1995) 433–447.

[29] C.G. Callan and D.J. Gross, "High-energy electroproduction and the constitution of the electric current", *Phys. Rev. Lett.* **22** (1969) 156–159.

[30] R.M. Barnett, "Evidence for New Quarks and New Currents", *Phys. Rev. Lett.* **36** (1976) 1163–1166.

[31] D.Yu. Bardin and V.A. Dokuchaeva, "On the Radiative Corrections to the Neutrino Deep Inelastic Scattering", Preprint E2-86-260, JINR, 1986.

[32] D.F. Geesaman, K. Saito and A.W. Thomas, "The nuclear EMC effect", *Annu. Rev. Nucl. Part. Sci.* **45** (1995) 337–390.

[33] T.H. Bauer, R.D Spital, D.R. Yennie and F.M. Pipkin, "The hadronic properties of the photon in high-energy interactions", *Rev. Mod. Phys.* **50** (1978) 261–436.

[34] N.N. Nicolaev and V.I. Zakharov, "Parton model and deep inelastic scattering on nuclei", *Phys. Lett.* **B55** (1975) 397–399.

[35] A.H. Mueller and J. Qiu, "Gluon recombination and shadowing at small values of x", *Nucl. Phys.* **B268** (1986) 427–452.

[36] A. Bodek and J.L. Ritchie, "Fermi-motion effects in deep-inelastic lepton scattering from nuclear targets", *Phys. Rev.* **D23** (1981) 1070–1091.

[37] A. Bodek and J.L. Ritchie, "Further studies of Fermi-motion effects in lepton scattering from nuclear targets", *Phys. Rev.* **D24** (1981) 1400–1402.

References

[38] H. Abramowicz *et al.*, CDHS *coll.*, "Experimental Study of Opposite-Sign Dimuons Produced in Neutrino and Antineutrino Interactions", *Z. Phys.* **C15** (1982) 19–31.

[39] Vincent Lemaître, "Production inclusive de particules charmées par interaction neutrino-nucléon dans l'expérience CHARM II", Ph.D. Thesis, Université catholique de Louvain (UCL), Louvain-la-Neuve, Belgium, 1995.

[40] P. Vilain *et al.*, "Leading order QCD analysis of neutrino-induced dimuon events", CERN-Preprint CERN-EP/98-128, CERN, August 1998.

[41] S.A. Rabinowitz *et al.*, CCFR *coll.*, "Measurement of the Strange Sea Distribution Using Neutrino Charm Production", *Phys. Rev. Lett.* **70** (1993) 134–137.

[42] A.O. Bazarko *et al.*, CCFR *coll.*, "Determination of the strange quark content of the nucleon from a next-to-leading-order QCD analysis of neutrino charm production", *Z. Phys.* **C65** (1995) 189–198.

[43] H. Plothow-Besch, "PDFLIB: Nucleon, Pion and Photon Parton Density Functions and α_s Calculations", User's Manual - Version 7.09, Computer Program Library W5051 PDFLIB, CERN, July 1997.

[44] M. Glück, S. Kretzer and E. Reya, "Detailed next-to-leading order analysis of deep inelastic neutrino induced charm production off strange sea partons", *Phys. Lett.* **B398** (1997) 381–386.

[45] B. Andersson, G. Gustafson and B. Söderberg, "A General Model for Jet Fragmentation", *Z. Phys.* **C20** (1983) 317–329.

[46] C. Peterson, D. Schlatter, I. Schmitt and P.M. Zerwas, "Scaling violations in inclusive e^+e^- annihilation spectra", *Phys. Rev.* **D27** (1983) 101–111.

[47] P.D.B. Collins and T.P. Spiller, "The fragmentation of heavy quarks", *J. Phys.* **G11** (1985) 1289–1298.

[48] D. Bortoletto *et al.*, CLEO *coll.*, "Charm production in nonresonant e^+e^- annihilation at $\sqrt{s} = 10.55$ GeV", *Phys. Rev.* **D37** (1988) 1719–1743.

[49] H. Albrecht *et al.*, ARGUS *coll.*, "Production and decay of the charged D* meson in e^+e^- annihilation at 10 GeV centre-of-mass energy", *Phys. Lett.* **B150** (1985) 235–241.

118

[50] N. Ushida *et al.*, E531 *coll.*, "Cross sections for neutrino production of charmed particles", *Phys. Lett.* **B206** (1988) 375–379.

[51] T. Bolton, "Determining the CKM Parameter V_{cd} from νN Charm Production", e-Print hep-ex/9708014, LANL, 1997, Updated Nevis Preprint R1501.

[52] C. Caso *et al.*, Particle Data Group, "Review of Particle Physics", *Eur. Phys. J. C* **3** (1998) 1–794.

[53] M. Jonker *et al.*, CHARM *coll.*, "Experimental study of opposite-sign and same-sign dimuon events produced in wide-band neutrino and antineutrino beams", *Phys. Lett.* **B107** (1981) 241–248.

[54] B. Strongin *et al.*, FMMF *coll.*, "Study of opposite-sign dimuon production in high-energy neutrino-nucleon interactions", *Phys. Rev.* **D43** (1991) 2778–2786.

[55] V. Jain *et al.*, E632 *coll.*, "Dimuon production by neutrinos in the Fermilab 15-ft bubble chamber at the Tevatron", *Phys. Rev.* **D41** (1990) 2057–2073.

[56] K. Lang *et al.*, CCFR *coll.*, "Neutrino Production of Dimuons", *Z. Phys.* **C33** (1987) 483–503.

[57] N. Ushida *et al.*, E531 *coll.*, "Experimental details on lifetime measurements of neutrino-produced charmed particles in a tagged emulsion spectrometer", *Nucl. Instrum. Meth.* **224** (1984) 50–64.

[58] N. Ushida *et al.*, E531 *coll.*, "Production characteristics of charmed particles in neutrino interactions", *Phys. Lett.* **B206** (1988) 380–384.

[59] M.H. Shaevitz, "Charm and dilepton production by neutrinos and antineutrinos", *Nucl. Phys.* **B19** (1991) 270–278.

[60] U.K. Yang *et al.*, "Measurements of the longitudinal structure function and $|V_{cd}|$ in the CCFR experiment", e-Print hep-ex/9806023, LANL, 1998, UR-1534, ER-40685-918.

[61] F. James, "Monte Carlo theory and practice", *Rep. Prog. Phys.* **43** (1980) 1145–1189.

[62] L. Montanet *et al.*, Particle Data Group, "Review of Particle Properties", *Phys. Rev.* **D50** (1994) 1173–1826.

References

[63] R. Oldeman, "Measurement of the beam flux from charged-current neutrino interactions in the Chorus calorimeter", CHORUS Internal Report 98001, CERN, March 1998.

[64] T. Sjöstrand, "High-energy-physics event generation with PYTHIA 5.7 and JETSET 7.4", *Comput. Phys. Commun.* **82** (1994) 74–89.

[65] T. Sjöstrand, "Pythia 5.7 and jetset 7.4, Physics and Manual", CERN, CERN Program Library Long Writeup W5035/W5044.

[66] G. Ingelman, "LEPTO version 6.1 — The LUND Monte Carlo for Deep Inelastic Lepton-Nucleon Scattering", Preprint TSL/ISV-92-0065, Uppsala University, May 1992.

[67] Z. Was, "The τ decay library tauola, version 2.4", *Comput. Phys. Commun.* **76** (1993) 361–380.

[68] Z. Was, "The τ decay decay library tauola, update with exact $O(\alpha)$ QED corrections in $\tau \to \mu\nu\bar{\nu}$ decay modes", *Comput. Phys. Commun.* **70** (1992) 69–76.

[69] Z. Was, "Radiative corrections", CERN Preprint CERN-TH 7151/91:32, CERN, January 1991.

[70] P. Zucchelli, "Tecniche calorimetriche per la selezione cinematica degli eventi nell'esperimento CHORUS", Ph.D. Thesis, Università degli Studi di Ferrara, Ferrara, Italy, 1992/1994.

[71] E. Eichten, I. Hinchliffe, K. Lane and C. Quigg, "Supercollider physics", *Rev. Mod. Phys.* **56** (1984) 579–707.

[72] E. Eichten, I. Hinchliffe, K. Lane and C. Quigg, "Erratum: Supercollider physics [*Rev. Mod. Phys.* **56** (1984) 579–707] ", *Rev. Mod. Phys.* **58** (1986) 1065–1073.

[73] B. Andersson, G. Gustafson, G. Ingelman and T. Sjöstrand, "Parton fragmentation and string dynamics", *Phys. Rev.* **97** (1983) 31–145.

[74] E.H.M. Heijne, "Muon flux measurement with silicon detectors in the CERN neutrino beams", Yellow Report 83-06, CERN, July 1983.

[75] G. Acquistapace *et al.*, "The West Area Neutrino Facility for CHORUS and NOMAD experiments (94-97 operation)", CERN Preprint CERN-ECP/95-14, CERN, July 1995.

120

[76] S. van der Meer, "A directive device for charged particles and its use in an enhanced neutrino beam", Yellow Report 61-7, CERN, February 1961.

[77] B. Van de Vyver and P. Zucchelli, "Prompt ν_τ background in Wide Band ν_μ Beams", CERN Preprint CERN-PPE/96-113, CERN, August 1996.

[78] M.C. Gonzalez-Garcia and J.J. Gomez-Cadenas, "Prompt ν_τ Fluxes in Present and Future Tau Neutrino Experiments", CERN Preprint CERN-PPE/96-114, CERN, 1996.

[79] S. Sorrentino, "GBEAM, the neutrino beam simulation", CHORUS Internal Report 98005, CERN, May 1998.

[80] F. Bergsma et al., "The hexagonal toroidal air-core magnet of the CHORUS detector", Nucl. Instrum. Meth. **A357** (1995) 243–248.

[81] S. Aoki et al., "Scintillating fiber trackers with opto electronic readout for the CHORUS neutrino experiment", Nucl. Instrum. Meth. **A344** (1994) 143–148.

[82] P. Annis et al., "Performance and calibration of the CHORUS scintillating fiber tracker and opto-electronics readout system", Nucl. Instrum. Meth. **A367** (1995) 367–371.

[83] P. Annis et al., "The CHORUS scintillating fiber tracker and opto-electronic readout system", Nucl. Instrum. Meth. **A412** (1998) 19–37.

[84] R. Wigmans, "On the energy resolution of uranium and other hadron calorimeters", Nucl. Instrum. Meth. **A259** (1987) 389–429.

[85] D. Acosta et al., "Electron, pion and multiparticle detector with a lead/scintillating-fiber calorimeter", Nucl. Instrum. Meth. **A308** (1991) 481–508.

[86] E. Bernardi et al., "Performance of a compensating lead-scintillator hadronic calorimeter", Nucl. Instrum. Meth. **A262** (1987) 229–242.

[87] D. Buontempo et al., "Construction and test of calorimeter modules for the CHORUS experiment", Nucl. Instrum. Meth. **A349** (1994) 70–80.

[88] E. Di Capua et al., "Response to electrons and pions of the calorimeter for the CHORUS experiment", Nucl. Instrum. Meth. **A378** (1996) 221–232.

References

[89] L. Gatignon, "The prolongated X9 test beam for CHORUS/WA95", CERN Preprint CERN SL/Note 95-72 (EA), CERN, 1995.

[90] G. Heyboer, "CAMMOR: Muon Momentum Calculation from Range in the Spectrometer", CHORUS Internal Report 96-06, CERN, August 1996.

[91] L.S. Brown and D.L. Nordstrom, "Passage of particles through matter", *Phys. Rev.* **D50** (1994) 1251–1258.

[92] H. Abramowicz *et al.*, CDHS *coll.*, "The response and resolution of an iron-scintillator calorimeter for hadronic and electromagnetic showers between 10 GeV and 140 GeV", *Nucl. Instrum. Meth.* **180** (1981) 429–439.

[93] A. Blondel *et al.*, CDHS *coll.*, "Electroweak parameters from a high statistics neutrino nucleon scattering experiment", *Z. Phys.* **C45** (1990) 361–379.

[94] J.P. DeWulf *et al.*, CHARM II *coll.*, "Test results of the streamer-tube system of the CHARM II neutrino detector", *Nucl. Instrum. Meth.* **A252** (1986) 443–449.

[95] J.P. DeWulf *et al.*, CHARM II *coll.*, "Test results and conditioning procedure of a limited streamer-tube calorimeter", *Nucl. Instrum. Meth.* **A263** (1988) 109–113.

[96] D. Geiregat *et al.*, CHARM II *coll.*, "Calibration and performance of the CHARM-II detector", *Nucl. Instrum. Meth.* **A325** (1993) 92–108.

[97] G. Marel *et al.*, "Large planar drift chambers", *Nucl. Instrum. Meth.* **141** (1977) 43–56.

[98] M. Holder *et al.*, CDHS *coll.*, "A detector for high-energy neutrino interactions", *Nucl. Instrum. Meth.* **148** (1978) 235–249.

[99] T. Patzak, "Muon detection in the CHORUS neutrino oscillation experiment", Ph.D. Thesis, Humboldt University of Berlin, Berlin, Germany, 1995.

[100] G. Zacek and H. Overas, "SAMTRA: Muon Track Finding and Fitting in the Spectrometer", 1989, CHARM2 offline manual.

[101] M.G. van Beuzekom *et al.*, "The trigger system of the CHORUS experiment", *Nucl. Instrum. Meth.* **A427** (1999) 587–606.

[102] G. Carnevale, J. Panman and F. Riccardi, "REMOS: A Portable Object Oriented Environment for Multiprocessor Real Time Applications", In *Proc. of Computing in High-energy Physics: CHEP '94*, 311–314, 1994, San Francisco, USA.

[103] G. Carnevale, J. Panman and F. Riccardi, "Chorus DAQ Tools Manual", CHORUS Manual.

[104] R. Gurin, "Interf.Lowlevel, Interf.README and Subscription", CHORUS Manuals.

[105] D. Bonekämper, "Ein Slow-Control-System für das CHORUS-Experiment", Dipl. Thesis, Westfälische Wilhelms-Universität, Münster, Germany, August 1993.

[106] G. Carnevale, B. Friend, J. Panman and F. Riccardi, "The CHORUS Data Acquisition System", In *Proc. of Computing in High-energy Physics: CHEP '94*, 101–103, 1994, San Francisco, USA.

[107] R. Meijer Drees, "CHORUS Histogram Package Users' Guide", CHORUS Manual.

[108] J. Brunner, "CHORAL Manual", CHORUS Manual.

[109] CERN, "HBOOK – Statistical Analysis and Histogramming", CERN Program Library Long Writeup Y250.

[110] C.A.F.J. van der Poel, "debughist, HistDump and Hbook2Chorus Users' Guide info and index file description", CHORUS Manual.

[111] J. Ousterhout, "Tcl and the Tk Toolkit", Addison-Wesley, 1994, ISBN 0-201-63337-X.

[112] CERN, "HIGZ – High level Interface to Graphics and Zebra, HPLOT – User's Guide", CERN Program Library Long Writeup Q120 and Y251.

[113] D.G. Cassel and H. Kowalski, "Pattern recognition in layered track chambers using a tree algorithm", *Nucl. Instrum. Meth.* **185** (1981) 235–251.

[114] H. Eichinger and M. Regler, "Review of track-fitting methods in counter experiments", Yellow Report 81-06, CERN, June 1981.

References

[115] R. Oldeman, "Study of charged current deep inelastic events in the Chorus calorimeter", CHORUS Internal Report 97020, CERN, September 1997.

[116] M. Arneodo *et al.*, NMC *coll.*, "The A dependence of the nuclear structure function ratios", *Nucl. Phys.* **B481** (1996) 3–22.

[117] M. Arneodo *et al.*, NMC *coll.*, "The structure function ratios $F_2^{\text{Li}}/F_2^{\text{D}}$ and $F_2^{\text{C}}/F_2^{\text{D}}$ at small x", *Nucl. Phys.* **B441** (1995) 12–30.

[118] CERN, "GEANT – Detector Description and Simulation Tool", CERN Program Library Long Writeup W5013.

[119] R. Oldeman, Veto-ing of CACC events due to Backscattering on the H plane, December 1997, Talk given at CHORUS collaboration meeting.

[120] CERN, "MINUIT – Function Minimization and Error Analysis", CERN Program Library Long Writeup D506.

[121] R.M. Barnett *et al.*, Particle Data Group, "Review of Particle Physics", *Phys. Rev.* **D54** (1996) 1–721.

[122] G.I. Smirnov, "On the universality of the x and A dependence of the EMC effect and its relation to parton distributions in nuclei", *Phys. Lett.* **B364** (1995) 87–92.

[123] M. Doucet and R. Oldeman, "Determination of the Relative WANF Beam Spectrum using a y-intercept technique", CHORUS Internal Report 98015, CERN, January 1999.

[124] R. Oldeman, Ph.D. Thesis in preparation.

[125] A.J. Buras and K.J.F. Gaemers, "Simple parametrizations of parton distributions with Q^2 dependence given by asymptotic freedom", *Nucl. Phys.* **B132** (1978) 249–267.

Summary

This thesis deals with charm production induced by neutrino deep inelastic scattering in the CHORUS calorimeter. The neutrinos, with an average energy of 26.6 GeV, are generated in the wide band neutrino beamline of the CERN super proton synchrotron. The observed events have a hadronic shower and two opposite sign muons in the final state. The main aim of our study is to determine the strange quark content of the nucleon, expressed through the parameter κ, and the shape of the strangeness distribution with respect to the one of the non-strange sea, given by α. Additional information is obtained on 1) the mass of the charm quark m_c, 2) the fragmentation of the charm quark to charmed hadrons, using the Peterson *et al.* fragmentation function with the free parameter ϵ_P, and 3) the average muonic decay branching ratio B_c of the produced charmed hadrons.

The part of the CHORUS detector central in our study consists of a set of trigger hodoscope planes, a calorimeter and a muon spectrometer. The calorimeter is used to measure the energy of the hadronic shower. The muon spectrometer—located in the beam direction downstream of the calorimeter—allows to identify muons and determines their trajectory, momentum and charge. The trigger selects neutrino events induced in the calorimeter with a hadronic shower and two tracks in the final state.

For each event selected by the trigger the muon track parameters and momenta as well as the energy of the hadronic shower are determined. With this information the vertex location and kinematical variables are calculated. Unreliable runs are removed with a global checking procedure. By imposing kinematical criteria events for the final analysis are selected while rejecting part of the background.

Two Monte Carlo models are applied in the analysis to simulate the data. The first one, JETTA, is the basis to correct the data for reconstruction and trigger acceptances. MCDIMUON, the other model, is used to obtain the values

Summary

of the parameters which describe charm production via neutrino deep inelastic scattering. Charged current single muon JETTA events and same sign muon events are used for the background estimation. Data and JETTA Monte Carlo distributions are compared, and found to be statistically compatible.

By using the above obtained data, acceptances and background estimation, the values of the parameters of the MCDIMUON model are obtained by performing a χ^2 fit. By fixing the shape of the strange sea with respect to the non-strange sea to $\alpha = 2.22 \pm 0.58$—obtained by calculating the weighted average found in the CHARM II [39, 40] and CCFR(LO) [41] analyses—we obtain the following result $m_c = (2.15 \pm 0.71 \pm 0.57)\,\mathrm{GeV}/c^2$, $\kappa = 0.260 \pm 0.092 \pm 0.058$, $B_c = (13.1 \pm 3.5 \pm 3.1)\%$, $\epsilon_P = 0.280 \pm 0.078 \pm 0.079$, where the first error is statistical and the last systematical. The parameter values determined in our analysis are compatible with those from CDHS [38], CCFR [41] and CHARM II [39,40] except ϵ_P. Our value of ϵ_P is only consistent with the value found by CCFR. The statistical errors of our results can be reduced by using all available CHORUS data. In that case we expect about a factor of ten more events. Then also the systematical errors would have to be reduced.

Samenvatting

Dit proefschrift behandelt charm productie geïnduceerd door neutrino diep-inelastische verstrooiing in de CHORUS calorimeter. De neutrino's, met een gemiddelde energie van 26.6 GeV, zijn opgewekt in de wide band neutrino bundellijn van het CERN super proton synchrotron. De waargenomen gebeurtenissen hebben in de eindtoestand een shower van hadronische deeltjes en twee muonen met tegengestelde lading. Het doel van ons onderzoek is het vaststellen van de hoeveelheid strangeness in het nucleon, uitgedrukt in een parameter κ, en de vorm van de strangeness verdeling ten opzichte van die voor de niet-strange quark zee, uitgedrukt in α. Informatie wordt ook verkregen over 1) de massa van het charm quark m_c, 2) de fragmentatie van het charm quark in gecharmeerde hadronen, die wordt geparametriseerd door de Peterson et al. fragmentatiefunctie met de vrije parameter ϵ_P en 3) de gemiddelde vertakkingsverhouding B_c voor verval van de geproduceerde gecharmeerde hadronen naar muonen.

Het deel van de CHORUS detector centraal in onze studie bestaat uit een aantal triggerhodoscoop-vlakken, een calorimeter en een muonspectrometer. De calorimeter wordt gebruikt om de energie van de hadronische shower te meten. De muonspectrometer, die in de bundelrichting stroomafwaarts van de calorimeter staat, maakt het mogelijk muonen te identificeren en hun traject, impuls en lading te bepalen. De trigger wordt gebruikt om neutrino-gebeurtenissen, die plaatsvinden in de calorimeter met een hadronische shower en twee sporen in de eindtoestand, te selecteren.

Van elke gebeurtenis, die geselecteerd is door de trigger, worden de muon-impulsen, de parameters van de muonsporen en de hadronische shower-energie bepaald. Met deze informatie wordt de vertexpositie en de kinematische variabelen berekend. Runs die onbetrouwbaar zijn worden verwijderd met een globale controle procedure. Door het toepassen van kinematische criteria worden gebeurtenissen voor de uiteindelijke analyse geselecteerd en tevens wordt

een deel van de achtergrond verwijdert.

Twee Monte Carlo modellen worden gebruikt in de analyse om meetgegevens te simuleren. Het eerste model, JETTA, vormt de basis voor correctie van de meetgegevens voor reconstructie en trigger acceptanties (efficienties). Het andere model, MCDIMUON, wordt gebruikt om de waarden van de parameters in de beschrijving van charm productie door neutrino diep-inelastische verstrooiing, te bepalen. JETTA gebeurtenissen met ten minste een muon gevormd door een geladen stroom wisselwerking, en gebeurtenissen met twee muonen die dezelfde lading hebben, worden gebruikt om de achtergrond af te schatten. Meetgegevens en JETTA Monte Carlo verdelingen zijn vergeleken; deze blijken statistisch in overeenstemming te zijn.

De hierboven beschreven meetgegevens, acceptanties en de achtergrond afschatting worden gebruikt om de waarden van de parameters van het MCDIMUON model te bepalen door een χ^2 fit. Door de verdeling van de strange zee ten opzichte van die van de niet-strange quark zee te fixeren op $\alpha = 2.22 \pm 0.58$, deze waarde is verkregen door het gewogen gemiddelde te berekenen van de waarden gevonden door de CHARM II [39, 40] en de CCFR(LO) [41] analyses, krijgen we als resultaat $m_c = (2.15 \pm 0.71 \pm 0.57)\,\mathrm{GeV}/c^2$, $\kappa = 0.260 \pm 0.092 \pm 0.058$, $B_c = (13.1 \pm 3.5 \pm 3.1)\%$, $\epsilon_P = 0.280 \pm 0.078 \pm 0.079$, waarin de eerste fout statistisch en de laatste systematisch van aard is. De waarden van de parameters die bepaald zijn in onze analyse, uitgezonderd ϵ_P, zijn binnen de statistische onzekerheid in overeenstemming met de resultaten van CDHS [38], CCFR [41] en CHARM II [39, 40]. Onze waarde van ϵ_P is alleen in overeenkomst met de waarde gevonden door CCFR. De statistische onzekerheid van onze resultaten kan verminderd worden door alle beschikbare CHORUS meetgegevens te gebruiken. Dan verwachten we ongeveer tien keer zoveel gebeurtenissen. In dit geval zal ook de systematische fout vermindert moeten worden.

Abbreviations

ADC	Analog to Digital Converter
BCT	Beam-Current Transformer
CC	Charged Current
CCD	Charged Coupled Device
CERN	European Laboratory for Particle Physics
CHORUS	CERN Hybrid Oscillation Research apparatUS
CKM	Cabibbo-Kobayashi-Maskawa
CPU	Computer Processing Unit
CS	Changeable Sheet
DAQ	Data Acquisition
DATSPC	Digital Analog Time information in the Spectrometer
DGLAP	Dokshitzer Gribov-Lipatov Altarelli-Parisi
DT	"Diamond-shaped" magnet Tracker
EFICASS	Emulsion FIbre Calorimeter Spectrometer Simulation
EM	Electromagnetic
FS	Fast Slow beam extraction of the SPS
FWHM	Full Width Half Maximum
GUI	Graphical User Interface
HAD	Hadronic
HV	CHORUS online monitoring Histogram Viewer
HWHM	Half Width Half Maximum
LO	Leading-Order
MC	Monte Carlo
NC	Neutral Current
NFM	Neutrino Flux Monitoring system

Abbreviations

NLO	Next-to-Leading-Order
PDG	Particle Data Group
PM	Photomultiplier
QCD	Quantum Chromodynamics
QPM	Quark Parton Model
REMOS	Remote Operating System
RMS	Root Mean Square
ROC	Readout Cell
SLAC	Stanford Linear Accelerator
SM	Standard Model
SPS	Super Proton Synchrotron
SS	Special Sheet
TDC	Time to Digital Converter
TST	Tracker Streamer Tubes
TT	Target Tracker
VIC	VME Inter Crate
VME	VersaModule Eurocard
WANF	West Area Neutrino Facility
WBB	Wide Band (Neutrino) Beam
ndf	number of degrees of freedom

Acknowledgements

A lot of people supported me in the process leading up to this thesis. I would like to thank them all, but can only address some of them here.

I am grateful to my promotor Piet Duinker for his guidance during the last year. We had many discussions about the work and the manuscript. I look back on these discussions with pleasure; they have paved the way for the thesis in its present form.

I would like to thank my supervisor René van Dantzig. Since he became our team leader he has supported me concerning the physics as well as on practical matters. His confidence in my work and his detailed suggestions during the development of the thesis have helped to shape it.

Joop Konijn, our previous team leader, took the initiative for the NIKHEF participation in CHORUS. He provided the opportunities to start my research work. I am grateful for his support and for many pleasant occasions of working and meeting together.

It is a pleasure for me to thank Jaap Panman for his guidance when I was based at CERN. He broadened my view on physics and involved me in the CHORUS data acquisition project. I also express my gratitude to Maarten de Jong for valuable suggestions on my analysis method, and for providing the method and the source code to estimate the background of my data.

I am indebted to Michiel Botje, Sijbrand de Jong, and Jona Oberski for their careful reading of the manuscript and their suggestions for improvement.

I am deeply obliged to Vincent Lemaître for the advice he gave on the analysis of neutrino induced opposite sign dimuon events, for the discussions about the analyse method and for providing the source code of MCDIMUON and the fitting programme. Joelle Herin gave valuable suggestions concerning the analysis. I am grateful to Kengo Nakamura who has built the code for simulating the calorimeter triggers.

Acknowledgements

132

Curriculum vitae

The author of this thesis was born on the 9th of October 1968 in Maastricht, The Netherlands. At the Stella Maris secondary school in Meerssen he obtained the Atheneum B certificate. After the compulsory military service, he started his physics studies in 1988 at Utrecht University, where he obtained the propaedeutic certificates in physics and astronomy after one year. At the end of his undergraduate studies, he investigated heavy-ion collisions in the Subatomic Physics department. This work resulted in a thesis entitled "Simulations of the reaction ^{40}Ca + ^{48}Ti at 25.0 and 33.9 MeV per nucleon" under supervision of drs. G.J. van Nieuwenhuizen, drs. T.M.V. Bootsma, and prof. dr. R. Kamermans. He obtained his "pre-doctoral" degree (resembling M.Sc. degree) in experimental physics in January 1993.

He started his Ph.D. research in February 1993 at the 'Nationaal Instituut voor Kernfysica en Hoge Energie Fysica (NIKHEF)' in Amsterdam. During the first two years, he was based at the European Laboratory for Particle Physics (CERN) in Geneva, Switzerland. He participated in the CHORUS experiment, and together with his colleagues he developed the general on-line monitoring system as well as the trigger implementation. After returning to NIKHEF, he investigated neutrino-induced deep-inelastic charm production in the CHORUS calorimeter. Part of his research is described in this thesis, which was supervised by dr. R. van Dantzig and prof. dr. P. Duinker.